

MASTER OF SCIENCE THESIS

# Multiscale Modeling of Fracture in Composites

A Progressive Failure Model for Cryogenic Applications

W. Westbroek

Faculty of Aerospace Engineering · Delft University of Technology





# **Multiscale Modeling of Fracture in Composites**

**A Progressive Failure Model for Cryogenic Applications**

MASTER OF SCIENCE THESIS

For obtaining the degree of Master of Science in Aerospace Engineering  
at Delft University of Technology

W. Westbroek

July 27, 2017

The work in this thesis was supported by AIRBUS Defence & Space. Their cooperation is gratefully acknowledged.



Copyright © W. Westbroek  
All rights reserved.



DELFT UNIVERSITY OF TECHNOLOGY  
FACULTY OF AEROSPACE ENGINEERING  
DEPARTMENT OF AEROSPACE STRUCTURES AND MATERIALS

**GRADUATION COMMITTEE**

Dated: July 27, 2017

Committee chairman:

\_\_\_\_\_

Dr. S. R. Turteltaub

Committee members:

\_\_\_\_\_

Dr. J. Fatemi

\_\_\_\_\_

Dr. A. M. Aragón



---

# Abstract

Airbus Defence and Space is seeking to replace aluminum with Carbon Fiber Reinforced Plastic (CFRP) for the second stage Engine Thrust Frame (ETF) of the Ariane 6 rocket, currently under development. The envisioned CFRP structure forms the interface between the cryogenic fuel tank and the rocket engine. The absence of a reliable predictive failure method for composites under cryogenic conditions has inhibited development of such a structure in the past. This project was developed and carried out in an effort to provide new insights into the field of composite fracture mechanics under cryogenic conditions, with a goal of developing a progressive failure model for cryogenic applications of composites.

A multiscale framework was developed to accommodate the micro-mechanics of (cryogenic) fracture in composites. The multiscale framework uses information on the microscopic scale, obtained by numerical fracture simulations on a Representative Volume Element (RVE) containing single or multiple fibers, to find effective macroscopic behavior by computational homogenization. The fracture is modeled using Cohesive Element Modeling (CEM) with embedded zero-thickness cohesive elements.

The RVEs were created using a newly developed python framework with a `gmsh` produced mesh. The framework is able to produce RVEs with a random fiber structure and a low-aspect-ratio triangular element mesh. The cohesive elements are added to the mesh by a python function. Periodic boundary conditions are applied to the edges of the RVE by coupling equations on selected nodes. The python framework automatically writes the microscale model to an ABAQUS<sup>®</sup> input file, which is executed on the Delft University of Technology computational cluster.

The multiscale fracture framework was verified at room temperature by establishing a RVE. The RVE was found through a size convergence scheme. In this scheme, a mesh convergence study was performed for three load cases applied to five increasing Microstructural Volume Element (MVE) sizes. For each MVE size, five random realizations were created to find an average fracture response and to determine a measure of the spread. The results of converged meshes were used to compare the effective fracture response for each of the MVE sizes and to establish the RVE for each load case individually. A RVE of  $75 \times 75 \mu\text{m}$  was discovered as representative for all three load cases. This RVE size was found for a fiber volume fraction of 50% with a weak fiber-matrix interface.

After a working room-temperature multiscale fracture framework was established, the cryogenic conditions were added to the model. The cryogenic conditions were simulated using a temperature step, in which the temperature was reduced from 298 K to 77 K. During the temperature step the RVE was allowed to contract freely. The difference in Coefficient of Thermal Expansion (CTE) between the carbon fibers (HexTow<sup>®</sup> IM7) and epoxy (CYCOM<sup>®</sup> 5230-1) matrix resulted in thermal stresses up to 50 MPa.

The presence of the thermal stresses was observed to have a limited influence on the effective macroscopic fracture behavior. The mode I fracture strength increased at the cryogenic operating temperature. The restricted matrix contraction resulted in high pre-compression of the weak fiber-matrix interface, which added resistance to mode I opening. Conversely, the mode II fracture strength was affected adversely by the cryogenic conditions, but the reduction in strength was small compared to the standard deviation.

---

# Table of Contents

<b>Nomenclature</b>	<b>xix</b>
List of Acronyms . . . . .	xix
List of Symbols . . . . .	xx
<b>Acknowledgments</b>	<b>xxiii</b>
<b>1 Introduction</b>	<b>1</b>
<b>2 Literature Review</b>	<b>5</b>
2.1 Fracture Mechanics: A Review . . . . .	5
2.1.1 Linear Elastic Fracture Mechanics . . . . .	5
2.1.2 Elastic Plastic Fracture Mechanics . . . . .	9
2.1.3 Failure in Fiber Reinforced Plastics . . . . .	11
2.2 Cohesive Element Modeling . . . . .	13
2.2.1 Cohesive Zone Models . . . . .	13
2.2.2 Cohesive Element Formulation . . . . .	17
2.2.3 Intrinsic and Extrinsic Methods . . . . .	21
2.2.4 Mesh dependency . . . . .	22
2.3 Multiscale Approach to Fracture . . . . .	23
2.3.1 Multiscale Concepts . . . . .	23
2.3.2 Computational Homogenization of Fracture Processes . . . . .	24
2.3.3 Representative Volume Element . . . . .	27
2.3.4 Periodicity . . . . .	28
2.4 Conclusion . . . . .	30

<b>3</b>	<b>Methodology</b>	<b>31</b>
3.1	Multiscale Implementation . . . . .	31
3.2	Modeling: The Microstructural Volume Element . . . . .	34
3.3	Homogenization . . . . .	35
3.3.1	Bulk Homogenization . . . . .	36
3.3.2	Effective Fracture Properties . . . . .	37
3.3.3	Mode mixity . . . . .	42
<b>4</b>	<b>Numerical Experimental Setup</b>	<b>45</b>
4.1	Preprocessing: Model generation . . . . .	45
4.1.1	Input variables . . . . .	46
4.1.2	Geometry . . . . .	47
4.1.3	Mesh . . . . .	49
4.1.4	Thermal/Mechanical Boundary Conditions . . . . .	52
4.1.5	Abaqus input file . . . . .	55
4.2	Solver: Settings and convergence . . . . .	61
4.3	Postprocessing . . . . .	62
4.3.1	Data extraction and processing . . . . .	63
4.3.2	Multiscale coupling: Hill-Mandel . . . . .	68
<b>5</b>	<b>Multiscale Traction-Separation Laws at Room Temperature</b>	<b>71</b>
5.1	Mesh Convergence . . . . .	74
5.1.1	Uniaxial Extension . . . . .	76
5.1.2	Biaxial Extension-Compression . . . . .	81
5.1.3	Mixed Mode . . . . .	86
5.2	Micro-structural Volume Element size: RVE . . . . .	89
5.2.1	Uniaxial Extension . . . . .	90
5.2.2	Biaxial Extension-Compression . . . . .	91
5.2.3	Mixed Mode . . . . .	93
<b>6</b>	<b>Simulations at Cryogenic Temperature</b>	<b>97</b>
6.1	Thermal Analysis Results . . . . .	98
6.1.1	Effective Coefficient of Thermal Expansion . . . . .	98
6.1.2	Thermal Stress . . . . .	101
6.2	Fracture . . . . .	104
6.2.1	Uniaxial extension . . . . .	104
6.2.2	Biaxial extension-compression . . . . .	106
6.2.3	Mixed Mode . . . . .	107
6.3	Mode mixity . . . . .	109
6.4	Initiation criterion . . . . .	111
6.5	Conclusion . . . . .	112

---

<b>7</b>	<b>Conclusions and Recommendations</b>	<b>113</b>
7.1	Conclusions . . . . .	113
7.2	Recommendations . . . . .	115
	<b>Bibliography</b>	<b>117</b>
<b>A</b>	<b>Power Plots</b>	<b>123</b>



---

# List of Figures

1.1	The multiscale concept . . . . .	2
2.1	Potential Energy and force as a function of atomic separation. At the equilibrium separation ( $x_0$ ), the potential energy is minimized and the attractive and repelling forces are balanced. . . . .	6
2.2	The three modes of loading that can be applied to a crack . . . . .	8
2.3	Arbitrary contour around the tip of a crack . . . . .	10
2.4	Examples of damage and fracture mechanisms in fiber-composites . . . . .	11
2.5	Representation of the ductile failure process by the CZM . . . . .	14
2.6	One-Dimensional Effective Displacement TSLs . . . . .	16
2.7	A two-dimensional solid containing a cohesive crack . . . . .	18
2.8	Discretization of the solid into continuum elements and zero-thickness interface elements . . . . .	19
2.9	Shortest Euclidean distance and shortest path over the mesh between two random points . . . . .	22
2.10	The multiscale cohesive scheme: The left half shows the macroscopic modeling, whereas the right half depicts microscopic modeling details in the RVE . . . . .	24
2.11	Schematic representation of the macroscale model. The internal boundary $\Gamma_d^M$ represents the cohesive crack [75] . . . . .	25
2.12	Schematic representation of the homogenization of bulk material properties . . . . .	25
2.13	Schematic representation of homogenization of cohesive fracture . . . . .	26
2.14	RVE size determination procedure . . . . .	28
2.15	Periodic Boundary Conditions . . . . .	29
2.16	Avoiding wall effects by material periodicity . . . . .	30
3.1	Phantom nodes and phantom domains for a cracked element . . . . .	31
3.2	A bilinear traction-separation relation that describes the fracture behavior . . . . .	32
3.3	Stiffness degradation ( $t_{ult} = 100 \text{ N/mm}^2$ , $d_f = 0.001 \text{ mm}$ ) . . . . .	33

3.4	SEM micrograph of Fiber Reinforced Epoxy . . . . .	34
3.5	Microstructural Volume Element . . . . .	35
3.6	Hill-Mandel requirement for an equivalent crack. The figure also illustrates the complication caused by the arbitrary orientation of the cohesive elements. . . . .	38
3.7	Macroscopic crack length . . . . .	39
3.8	Mode mixity parameter $\beta$ . . . . .	42
4.1	Schematic representation of the preprocessing computational framework . . . . .	45
4.2	Method for picking fiber origins . . . . .	48
4.3	Microstructure comparison: SEM and MVE . . . . .	49
4.4	Two MVE meshes created using gmsk ( $V_f = 0.5$ , $w = h = 5e-2$ mm, $a = b = 5e-3$ mm ) . . . . .	51
4.5	Definition of boundary conditions to the MVE . . . . .	53
4.6	Method for defining the node pairs used for the periodic boundary conditions in a mesh with embedded cohesive elements . . . . .	53
4.7	Initial temperature distribution (above) and temperature distribution after cooling down (below) . . . . .	54
4.8	Boundary conditions applied in either load step . . . . .	55
4.9	Element Definition: Counter-Clockwise node numbering . . . . .	56
4.10	Definition of the thermal expansion coefficient . . . . .	59
4.11	Energy evolution in a typical simulation . . . . .	62
4.12	Schematic representation of the postprocessing framework . . . . .	63
4.13	Deformation and maximum in-plane principal stress at the final state of the simulation . . . . .	65
4.14	Cohesive element: Initial and deformed/opened state . . . . .	66
4.15	Power evolution for a typical uniaxial extension simulation ( $75 \times 75 \mu\text{m}$ MVE) . . . . .	68
4.16	ETLS for Mode I obtained for $\alpha = 0.4$ . . . . .	70
5.1	Unit cell ( $12.5 \times 12.5 \mu\text{m}$ ) . . . . .	72
5.2	MVE sizes tested in the convergence study . . . . .	72
5.3	Cohesive material properties used in the convergence study . . . . .	73
5.4	Deformations applied for the convergence study . . . . .	74
5.5	$12.5 \times 12.5 \mu\text{m}$ (Unit cell) . . . . .	75
5.6	$50 \times 50 \mu\text{m}$ . . . . .	75
5.7	$75 \times 75 \mu\text{m}$ . . . . .	75
5.8	Uniaxial Extension . . . . .	76
5.9	Mesh Convergence: Deformation (Uniaxial Extension, Unit Cell: $12.5 \times 12.5 \mu\text{m}$ ) . . . . .	77
5.10	Mesh Convergence: ETSL (Uniaxial Extension, Unit Cell: $12.5 \times 12.5 \mu\text{m}$ ) . . . . .	78
5.11	Mesh Convergence: Crack Configuration (Uniaxial Extension, Unit Cell: $12.5 \times 12.5 \mu\text{m}$ ) . . . . .	78
5.12	The effect of viscous stresses on the ETSL . . . . .	79
5.13	Mesh Convergence: Uniaxial Extension, $37.5 \times 37.5 \mu\text{m}$ . . . . .	79

5.14	Mesh Convergence: Uniaxial Extension, $50 \times 50 \mu\text{m}$ . . . . .	80
5.15	Mesh Convergence: Uniaxial Extension, $62.5 \times 62.5 \mu\text{m}$ . . . . .	80
5.16	Mesh Convergence: Uniaxial Extension, $75 \times 75 \mu\text{m}$ . . . . .	81
5.17	Biaxial Extension-Compression . . . . .	81
5.18	Mesh Convergence: Deformation (Biaxial Extension-Compression, Unit Cell: $12.5 \times 12.5 \mu\text{m}$ ) . . . . .	82
5.19	Mesh Convergence: ETSL (Biaxial Extension-Compression, Unit Cell: $12.5 \times 12.5 \mu\text{m}$ ) . . . . .	83
5.20	Mesh Convergence: Crack Configuration (Biaxial Extension-Compression, Unit cell: $12.5 \times 12.5 \mu\text{m}$ ) . . . . .	83
5.21	Mesh Convergence: Biaxial Extension-Compression, $37.5 \times 37.5 \mu\text{m}$ . . . . .	84
5.22	Mesh Convergence: Biaxial Extension-Compression, $50 \times 50 \mu\text{m}$ . . . . .	84
5.23	Mesh Convergence: Biaxial Extension-Compression, $62.5 \times 62.5 \mu\text{m}$ . . . . .	85
5.24	Mesh Convergence: Biaxial Extension-Compression, $75 \times 75 \mu\text{m}$ . . . . .	85
5.25	Mesh Convergence: Deformation (Mixed, Unit Cell: $12.5 \times 12.5 \mu\text{m}$ ) . . . . .	86
5.26	Mesh Convergence: ETSL (Mixed, Unit Cell: $12.5 \times 12.5 \mu\text{m}$ ) . . . . .	87
5.27	Mesh Convergence: Crack Configuration (Mixed, Unit cell: $12.5 \times 12.5 \mu\text{m}$ ) . . . . .	87
5.28	Mesh Convergence: Mixed, $37.5 \times 37.5 \mu\text{m}$ . . . . .	88
5.29	Mesh Convergence: Mixed, $50 \times 50 \mu\text{m}$ . . . . .	88
5.30	Mesh Convergence: Mixed, $62.5 \times 62.5 \mu\text{m}$ . . . . .	89
5.31	Mesh Convergence: Mixed, $75 \times 75 \mu\text{m}$ . . . . .	89
5.32	RVE convergence: ETSL Mode I, Uniaxial Extension . . . . .	90
5.33	RVE Convergence: Crack Material Content, Uniaxial Extension . . . . .	91
5.34	RVE Convergence: ETSL Mode II, Biaxial Extension-Compression . . . . .	92
5.35	RVE Convergence: Crack Material Content, Biaxial Extension-Compression . . . . .	92
5.36	RVE Convergence: ETSL Mode I, Mixed . . . . .	93
5.37	RVE Convergence: ETSL Mode II, Mixed . . . . .	94
5.38	RVE Convergence: ETSL absolute, Mixed . . . . .	94
5.39	RVE Convergence: Crack Material Content, Mixed . . . . .	95
6.1	Thermal Strain Evolution . . . . .	99
6.2	Effective CTE of the Composite . . . . .	100
6.3	Thermal Stress at $T = 77 \text{ K}$ . . . . .	102
6.4	Thermal tensile stress in the matrix developing radially around fibers . . . . .	103
6.5	Five Realizations of the $75 \times 75 \mu\text{m}$ RVE ( $V_f = 50\%$ ) . . . . .	104
6.6	Uniaxial Extension (Mode I) . . . . .	105
6.7	Crack Material Content: Uniaxial Extension . . . . .	105
6.8	Biaxial Extension-Compression (Mode II) . . . . .	106
6.9	Crack Material Content: Biaxial Extension-Compression . . . . .	107
6.10	Mixed (Mode I) . . . . .	107

---

6.11 Mixed (Mode II) . . . . .	108
6.12 Crack Material Content: Mixed . . . . .	108
6.13 Ultimate traction as a function of mode mixity . . . . .	109
6.14 Fracture Energy as a Function of Mode Mixity . . . . .	110
6.15 Typical Mode I and II Crack Morphologies . . . . .	110
A.1 Power Plot: Uniaxial Extension, $75 \times 75 \mu\text{m}$ MVE, $T = 77 \text{ K}$ . . . . .	124
A.2 Power Plot: Uniaxial Extension, $75 \times 75 \mu\text{m}$ MVE, $T = 298 \text{ K}$ . . . . .	125
A.3 Power Plot: Biaxial Extension-Compression, $75 \times 75 \mu\text{m}$ MVE, $T = 77 \text{ K}$ . . . . .	126
A.4 Power Plot: Biaxial Extension-Compression, $75 \times 75 \mu\text{m}$ MVE, $T = 298 \text{ K}$ . . . . .	127
A.5 Power Plot: Mixed Mode, $75 \times 75 \mu\text{m}$ MVE, $T = 77 \text{ K}$ . . . . .	128
A.6 Power Plot: Mixed Mode, $75 \times 75 \mu\text{m}$ MVE, $T = 298 \text{ K}$ . . . . .	129

---

## List of Tables

4.1	Input parameters: Geometry . . . . .	46
4.2	Input parameters: Loading . . . . .	46
4.3	Input parameters: Material Properties . . . . .	47
4.4	Input parameters: Solver Settings [1] . . . . .	61
5.1	Real fiber volume fraction for the considered MVE sizes (Fiber radius: $r = 5 \mu\text{m}$ )	73
6.1	RVE geometry . . . . .	97
6.2	Bulk Material Properties [12, 16, 34] . . . . .	98
6.3	Cohesive Material Properties . . . . .	98
6.4	Comparison between RoM and Simulation Results . . . . .	111
6.5	Principal strain direction for all three load cases . . . . .	111
6.6	Crack orientation observed in the simulation (RT) compared to the principal strain direction . . . . .	112



---

# Nomenclature

## List of Acronyms

<b>API</b>	Application Programming Interface
<b>ASI</b>	Abaqus Scripting Interface
<b>BVP</b>	Boundary Value Problem
<b>CEM</b>	Cohesive Element Modeling
<b>CFRP</b>	Carbon Fiber Reinforced Plastic
<b>CTE</b>	Coefficient of Thermal Expansion
<b>CTOD</b>	Crack Tip Opening Displacement
<b>CZM</b>	Cohesive Zone Model
<b>DNS</b>	Direct Numerical Simulation
<b>DOF</b>	Degree of Freedom
<b>EPFM</b>	Elastic-Plastic Fracture Mechanics
<b>ETF</b>	Engine Thrust Frame
<b>ETSL</b>	Effective Traction Separation Law
<b>FE</b>	Finite Element
<b>FEA</b>	Finite Element Analysis
<b>FEM</b>	Finite Element Method
<b>FRP</b>	Fiber Reinforced Plastic
<b>GFRP</b>	Glass Fiber Reinforced Plastic
<b>GUI</b>	Graphical User Interface

<b>LEFM</b>	Linear Elastic Fracture Mechanics
<b>LOX</b>	Liquid Oxygen
<b>LH2</b>	Liquid Hydrogen
<b>MVE</b>	Microstructural Volume Element
<b>PBC</b>	Periodic Boundary Conditions
<b>PPR</b>	Park-Paulino-Roesler
<b>RoM</b>	Rule of Mixtures
<b>RVE</b>	Representative Volume Element
<b>RT</b>	Room Temperature
<b>SEM</b>	Scanning Electron Microscope
<b>SIF</b>	Stress Intensity Factor
<b>SSTO</b>	Single Stage To Orbit
<b>SVD</b>	Singular Value Decomposition
<b>TSL</b>	Traction-Separation Law
<b>TU Delft</b>	Delft University of Technology
<b>UD</b>	Unidirectional
<b>XFEM</b>	eXtended Finite Element Method

## List of Symbols

$\alpha$	Coefficient of Thermal Expansion
$\bar{\epsilon}$	Applied Strain
$\beta$	Mode mixity parameter
$\delta$	Separation
$\delta_0$	Separation at damage initiation
$\delta_f$	Separation at failure
$\Gamma^f$	Equivalent macroscopic crack length
$\kappa$	Thermal Conductivity
$\mu$	Shear Modulus
$\nu$	Poisson's ratio
$\omega$	Stiffness Degradation Parameter
$\rho$	Density

$\mathbf{t}_T^f$	Crack averaged traction macroscopic traction vector
$[[\mathbf{u}]]^f$	Macroscopic crack opening
$C_p$	Specific Heat
$E$	Young's Modulus
$G$	Fracture Energy
$K$	Initial Elastic Stiffness
$N_f$	Number of fibers
$V_f$	Fiber volume fraction
$t$	Traction



---

# Acknowledgments

Firstly, I would like to express my gratitude to my thesis supervisor Dr. Sergio Turteltaub. His broad knowledge of fracture and solid mechanics was of great help when discussing approaches or new ideas. Dr. Turteltaub always took the time for me and my project and has been of tremendous support.

I would like to thank my supervisor at Airbus Defence and Space, Dr. Javad Fatemi. Without the effort of Dr. Fatemi the cooperation between Delft University of Technology and Airbus Defence and Space would not have been possible. Dr. Fatemi has provided me all the resources I needed to make this thesis into a successful project.

I would also like to acknowledge Christian Hirsch. We were in the same boat, both doing our MSc. theses on multiscale modeling. I very much enjoyed the lengthy discussions about the multiscale method and the time spent going over our individual struggles.

Lastly, I would like to thank my beautiful girlfriend Nicole Valderrábano. Next to proofreading my work and proposing corrections, you have been my greatest supporter. You were with me every step of the way.

Delft, University of Technology  
July 27, 2017

W. Westbroek



---

# Chapter 1

---

## Introduction

In recent years, the demand for an affordable launch vehicle service to deliver payloads to Earth orbits has dramatically increased due to growth in the satellite and space industries. To meet consumer demands, the next generation of launch vehicles need to cost less to produce and launch. One option to reduce cost, is to reduce the weight of the launch vehicle structure, thus cutting down on material and fuel costs. Alternatively, a reduction in structural weight allows for an increase in payload capacity weight, keeping the total launch cost the same as it would be with the original structure/weight. The opportunity to reduce launch cost makes exploration into structural weight savings a worthwhile venture.

Due to high specific strength and stiffness attributes, composites in the Carbon Fiber Reinforced Plastic (CFRP)-family can play an important role in saving weight and offer candidate materials for highly loaded structures such as cryogenic fuel tanks and thrust frames. However attractive, the application of CFRP for spacecraft or launcher structures has not been without set-backs - most notably the premature failure of a large-scale LH2 tank during testing of NASA's Single Stage To Orbit (SSTO) concept (X-33, technological demonstrator), which left the program without further options for development and funding, ultimately resulting in cancellation. For this particular program, the failure was attributed to microcracking as a result of thermal stresses for which a reliable failure prediction method had not yet been developed [46].

A composite consists of two or more materials which, in combination, exploit the strong-points of each constituent. For Carbon/Epoxy composites the carbon fibers provide formidable strength and stiffness, while the epoxy provides toughness, support and protection against the environment. Fracture in composites is the result of several different failure mechanisms within the constituents and at the interfaces. Global failure of the composite structure occurs when the damage within the plies (microcracking, fiber/matrix-interface failure, etc.) and inter-ply failure (delamination) has accumulated to the point that the residual strength is no longer sufficient to carry the load; Therefore, the notion that you cannot accurately predict failure in composites without making a distinction between the diverse constituents, is fundamental and valid.

Given the necessary computational power one could model the entire composite structure in detail, with the fibers and matrix separately included, and use Cohesive Element Modeling (CEM) or the eXtended Finite Element Method (XFEM) to model fracture. Unfortunately, one would need to repeat this process to investigate a sufficient amount of fiber distributions, out of an infinite number of possibilities, to determine average strength. At this time, it is difficult to imagine analyzing anything larger than small tensile specimen with this approach. The multiscale concept, shown schematically in Figure 1.1, couples multiscale (microscopic and macroscopic) perspectives by homogenizing and collapsing the results of the microscale analyses to an effective behavior that can be used macroscopically.

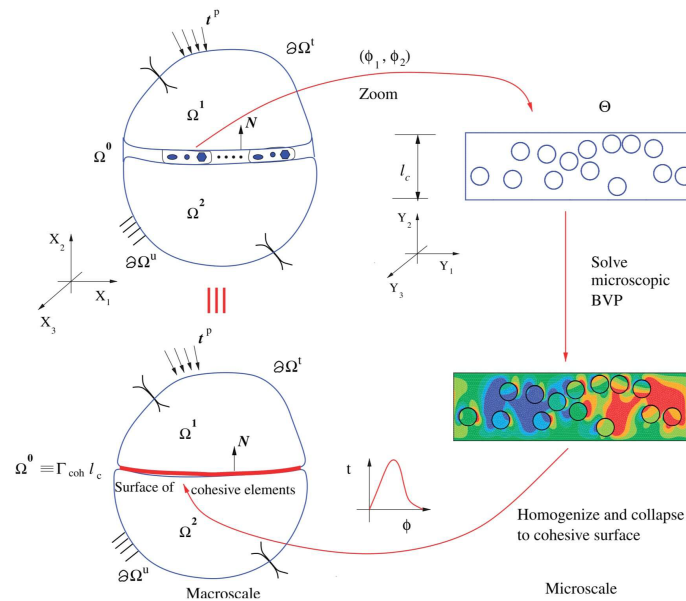


**Figure 1.1:** The multiscale concept [43]

The concept of multiscale modeling is powerful since it provides a way to develop a failure prediction method rooted in micromechanics and the physics of fracture. This thesis project will apply multiscale modeling to develop a failure method for cryogenic applications of CFRP. The objective is formulated as follows:

*The research objective of the MSc. Thesis is to develop a damage onset and growth model for transverse fracture inside Unidirectional (UD) CFRP plies under combined thermal and mechanical loading and under cryogenic conditions, by using advanced numerical methods on the microscopic scale coupled with the macroscale by computational homogenization, a technique known as multiscale modeling.*

The thesis objective requires a multiscale framework for transverse fracture to be developed and verified. The multiscale framework will use the Cohesive Zone Model (CZM) with embedded zero-thickness cohesive elements on the microscopic scale, similar to what was done by [73], to find the effective constitutive fracture behavior to be used at the macroscopic scale. The macroscale analysis itself is left out of the scope of the thesis project. The microscopic analysis is performed on a Representative Volume Element (RVE), which is a Microstructural Volume Element (MVE) that is large enough to be constitutively valid. Establishing the RVE

is critical to the validity of the multiscale method. The thesis work can be divided into three sub-objectives:

- Develop a method to automatically create MVEs capturing the composite microstructure in the transverse plane.
- Obtain a RVE by a size convergence study and find effective fracture behavior at room temperature.
- Find the effective fracture behavior at cryogenic temperature and isolate the effect of the thermal load.

The structure of the report is as follows; Chapter 2 presents a comprehensive overview of the theory relevant to the project and summarizes the literature study [78] performed in support of the thesis project. The theory of the multiscale fracture framework and the homogenization to effective thermal and cohesive constitutive behavior is discussed in Chapter 3. The computational implementation of the theory is included in Chapter 4. The multiscale framework will be applied to obtain room temperature effective fracture behavior in the form of an Effective Traction Separation Law (ETSL) for three different load cases. The effective fracture behavior will be used to establish the RVE size in Chapter 5. The room temperature results are used as a baseline to study the effect of the cryogenic thermal load. The results of the cryogenic simulations and the effective macroscale model are given in Chapter 6. Lastly, the conclusions and recommendations are included in Chapter 7.



---

## Chapter 2

---

# Literature Review

Chapter 2 contains an overview of the literature study completed prior to beginning the thesis. In this chapter, the foundation for fracture mechanics is laid out in Section 2.1, followed by an explanation of Cohesive Element Modeling (CEM) in Section 2.2.2. Chapter 2 concludes with discussing a multiscale approach to fracture.

### 2.1 Fracture Mechanics: A Review

This section explores the history and theory behind fracture mechanics leading up to modern day. Section 2.1.1 discusses the classical approach to fracture, known as Linear Elastic Fracture Mechanics (LEFM), and explains the various fracture modes. In Section 2.1.2 Elastic-Plastic Fracture Mechanics (EPFM) is explained as an extension to LEFM. Failure in reinforced plastics is included in Section 2.1.3.

#### 2.1.1 Linear Elastic Fracture Mechanics

The work done in fracture mechanics prior to the 1960's focused on materials that obey Hooke's law, with corrections for small-scale plasticity from 1948 onward. This type of fracture analysis is only applicable to structures whose global behavior is linear elastic. In more recent history, theories have been developed for various types of non-linear material behavior, such as (visco)plasticity, as well as dynamic effects. These developments can be seen as extensions to LEFM, which will be discussed later in this section.

Fracture occurs when the stresses and work applied to a material are sufficient to break the bonds between the atoms within the material [5]. The bond strength is generated by the forces between the atoms. In Figure 2.1 the potential energy and force is represented as a function of atomic distance. The equilibrium distance ( $x_0$ ) occurs when the potential energy is at a minimum. In order to increase the spacing between atoms, a tensile force must be applied.

The bond energy is obtained by integrating the force over the atomic distance. The limit of this integral is, in theory, the equilibrium distance to infinity [5]:

$$E_b = \int_{x_0}^{\infty} P dx \quad (2.1)$$

The force is typically approximated as a half period of a sine function, with period  $2\lambda$ . By assuming  $\lambda = x_0$ , the cohesive stress  $\sigma_c$  can be approximated by equation Eq. (2.2) [5].

$$\sigma_c \approx \frac{E}{\pi} \quad (2.2)$$

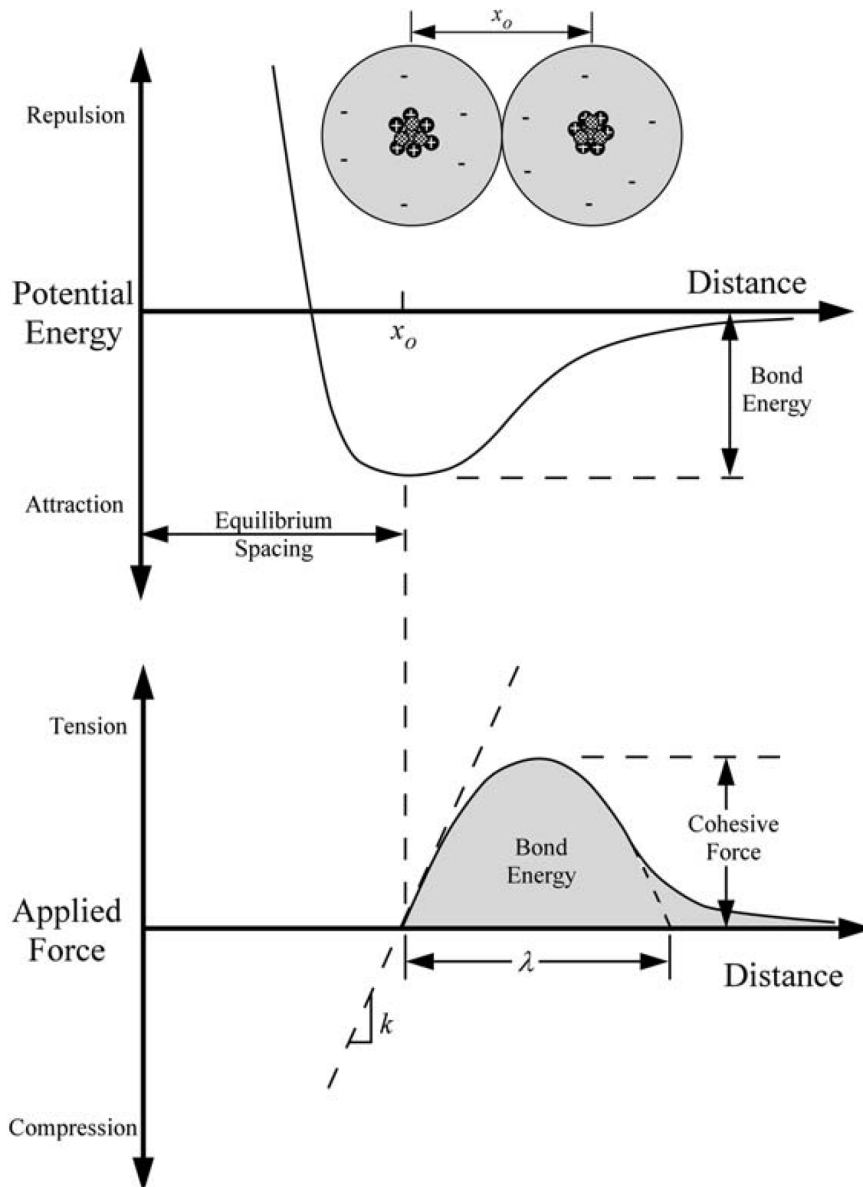


**Figure 2.1:** Potential Energy and force as a function of atomic separation. At the equilibrium separation ( $x_0$ ), the potential energy is minimized and the attractive and repelling forces are balanced. [5]

Experimentally determined fracture strengths diverge from the theoretical strength values,  $E/\pi$ , typically by three or four orders of magnitude. The notion that flaws in a material determine the fracture strength was introduced as early as the late 15<sup>th</sup> century. Leonardo da Vinci measured the strength of iron wires and found that it varied inversely with wire length. His finding implied that flaws in a material controlled the strength since a longer wire had a higher probability of containing a region with a flaw.

Inglis [38] was the first to analyze stress concentrations caused by elliptical holes in plates. For an infinite plate under far field uniaxial stress  $\sigma$  with an elliptical hole with semi-axes  $a$  and  $b$ , with axis  $a$  perpendicular to the far field stress direction, the stress at the tip of axis  $a$  is given by Eq. (2.3).

$$\sigma_{\max} = \sigma \left( 1 + \frac{2a}{b} \right) \quad (2.3)$$

Inglis [38] preferred to express this relation in terms of radius of curvature  $\rho = b^2/a$ .

$$\sigma_{\max} = \sigma \left( 1 + 2\sqrt{\frac{a}{\rho}} \right) \quad (2.4)$$

The ratio  $\sigma_{\max}/\sigma$  is known as the stress concentration factor ( $K_t$ ). For a circular hole the stress concentration is  $K_t = 3$ . Although the continuum assumptions made for this relation cannot be used to compute the fracture stress at the atomic scale, it supports the idea that flaws have an effect on the fracture stress [5].

For a sharp crack  $\rho \rightarrow 0$  the stress at the tip of the flaw/crack will go to infinity; therefore, theoretically, a material containing a sharp crack will fracture under an infinitesimally small stress. This paradox motivated Griffith [30] to develop a fracture theory based on energy instead of local stress [5].

The First Law of Thermodynamics encompasses several principles, perhaps most importantly the conservation of energy and the concept of internal energy. The First Law also states that when a system goes from a non-equilibrium state to equilibrium, there must be a net decrease in energy. In other words, energy is minimized for an equilibrium. Griffith [30] applied this idea to the analysis of a crack of length  $2a$  in the 1920's.

According to Griffith [30], when a crack is extended by an incremental energy  $dA$ , the total energy  $E$  equilibrium condition can be expressed as:

$$\frac{dE}{dA} = \frac{d\Pi}{dA} + \frac{dW_s}{dA} = 0 \quad (2.5)$$

And therefore:

$$-\frac{d\Pi}{dA} = \frac{dW_s}{dA}$$

where  $\Pi$  is the potential energy (internal strain energy + external work) and  $W_s$  is the work required to create new surfaces. Since the formation of a crack simultaneously creates two surfaces ( $A_s$ ),  $W_s$  can be expressed by Eq. (2.6):

$$W_s = 2A_s\gamma_s = 4at\gamma_s \quad (2.6)$$

Where  $\gamma_s$  is the surface energy density. Using this approach, Griffith [30] found that the fracture stress can be expressed as Eq. (2.7) for plane stress. Equation (2.7) is known as the

Griffith's failure criterion [30].

$$\sigma_f = \sqrt{\frac{2E\gamma_s}{\pi a}} \quad (2.7)$$

Parallel to the energy approach proposed by Griffith [30], a stress-based approach to fracture was developed in the late 1930's. For linear elastic isotropic material behavior, it is possible to derive closed form solutions for the stresses in the neighborhood of a crack tip. Westergaard [79] was the first to publish such a solution, followed by Sneddon [64], Irwin [39] and Williams [80].

A crack can be loaded in three different modes and combinations thereof. For Mode I loading the principle load is applied normal to the crack plane, which is referred to as the *opening mode*. Mode II loading occurs when the crack faces slide in opposite directions with respect to each other, corresponding to in-plane shear loading. Mode III is the out-of-plane shear mode, sometimes also referred to as the *tearing mode* [5]. The three modes are rendered in Figure 2.2.

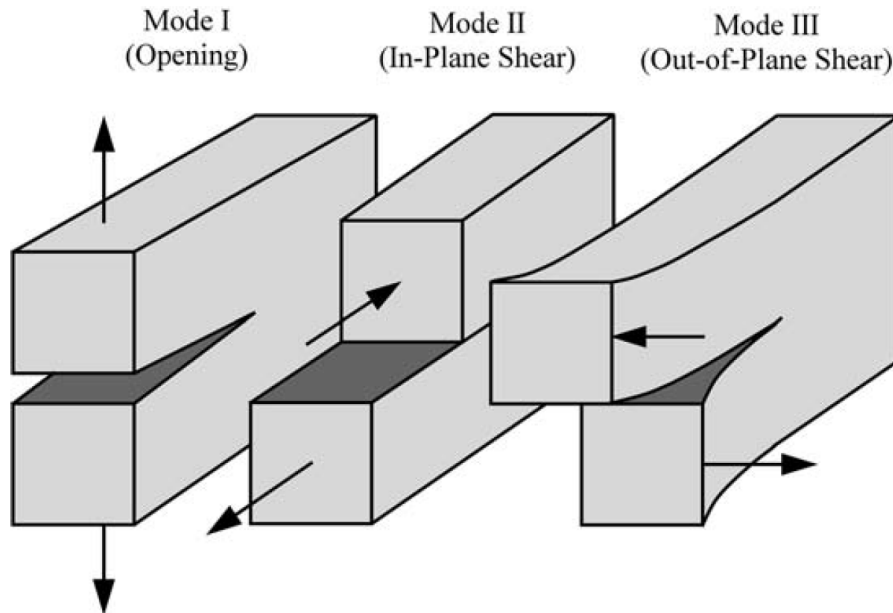


**Figure 2.2:** The three modes of loading that can be applied to a crack [5]

The Stress Intensity Factor (SIF), denoted  $K$ , defines the amplitude of the crack tip stress singularity - meaning the stresses near the crack tip increase proportional to  $K$ . The SIF is not a material property, rather it is a function of crack geometry and remote stress with units of  $\text{stress} \cdot \sqrt{\text{length}}$ . The SIF is different for each loading mode and therefore  $K_I$ ,  $K_{II}$  and  $K_{III}$

are distinguished. The stress field ahead of a crack tip can be written as:

$$\sigma_{ij}^{\text{I}} = \frac{K_{\text{I}}}{\sqrt{2\pi r}} f(\theta) \quad (2.8a)$$

$$\sigma_{ij}^{\text{II}} = \frac{K_{\text{II}}}{\sqrt{2\pi r}} f(\theta) \quad (2.8b)$$

$$\sigma_{ij}^{\text{III}} = \frac{K_{\text{III}}}{\sqrt{2\pi r}} f(\theta) \quad (2.8c)$$

Superposition of the stresses can be used for mixed mode problems:

$$\sigma_{ij} = \sigma_{ij}^{\text{I}} + \sigma_{ij}^{\text{II}} + \sigma_{ij}^{\text{III}}$$

The SIF can be compared to material property critical values ( $K_{\text{I}}^c$ ,  $K_{\text{II}}^c$  and  $K_{\text{III}}^c$ ) to model crack growth. It has been proven that the energy release rate and the stress intensity factor are related. For a mixed mode crack loading, the strain energy release rate is given by Eq. (2.9):

$$G = \frac{K_{\text{I}}^2}{E'} + \frac{K_{\text{II}}^2}{E'} + \frac{K_{\text{III}}^2}{2\mu} \quad (2.9)$$

where  $E'$  is either the plane stress ( $E' = E$ ) or plane strain ( $E' = E/(1 + \nu^2)$ ) longitudinal modulus and  $\mu$  is the shear modulus.

### 2.1.2 Elastic Plastic Fracture Mechanics

LEFM is limited to materials that have global linear elastic behavior. Small scale non-linear behavior can be compensated, but must be confined to a minuscule region surrounding the crack tip [5]. For tougher materials it is impossible to accurately model fracture using LEFM. EPFM can be used for materials that exhibit time-independent, non-linear behavior, such as plastic deformation. In this section two common approaches will be discussed, namely the Crack Tip Opening Displacement (CTOD) and the J contour integral.

While studying the fracture behavior of high-toughness steels, Wells [77] discovered that crack faces opened prior to fracture by plastic deformation, blunting an initially sharp crack. The measure of crack tip blunting increased proportionally to the toughness of the material. Wells [77] proposed to use the opening of the crack tip as a fracture toughness parameter, which became known as the CTOD.

Irwin [40] further developed the theory of Wells [77] and related the CTOD to the SIF, given by Eq. (2.10).

$$\delta = \frac{4}{\pi} \frac{K_{\text{I}}^2}{E\sigma_{YS}} \quad (2.10)$$

Where  $\sigma_{YS}$  is the yield stress. The CTOD can also be related to the energy release rate by Eq. (2.11).

$$\delta = \frac{4}{\pi} \frac{G}{\sigma_{YS}} \quad (2.11)$$

Rice [60] presented a path-independent contour integral for the analysis of cracks, known as the *J Contour Integral*. By idealizing elastic-plastic behavior as nonlinear elastic, Rice [60]

revolutionized the field of fracture mechanics and opened up possibilities well beyond the applicability of LEFM.

The difference between a non-linear elastic and elastic-plastic material lies in the unloading behavior. A non-linear elastic material simply unloads along the same path it was loaded, while an elastic-plastic material will unload linearly, with the slope of the path equal to the Young's modulus, and dissipate energy. Provided that no unloading occurs, the idealization to a non-linear elastic material is valid.

The nonlinear energy release rate  $J$  is given by Eq. (2.12).

$$J = -\frac{d\Pi}{dA} \quad (2.12)$$

Rice [60] proved that the value of a contour integral on an arbitrary counter-clockwise path around the tip of a crack, as illustrated in Figure 2.3, is independent of the path and equals the non-linear energy release rate Eq. (2.13).

$$J = \int_{\Gamma} \left( w dy - T_i \frac{\partial u_i}{\partial x} ds \right) \quad (2.13)$$

The strain energy is defined by Eq. (2.14).

$$w = \int_0^{\epsilon_{ij}} \sigma_{ij} d\epsilon_{ij} \quad (2.14)$$

The traction vector  $T_i$  is given by Eq. (2.15).

$$T_i = \sigma_{ij} n_j \quad (2.15)$$

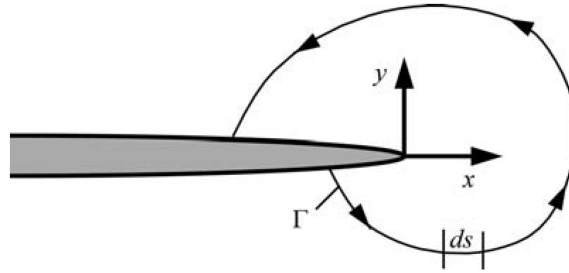


**Figure 2.3:** Arbitrary contour around the tip of a crack [5]

The non-linear energy release rate and the CTOD are related through Eq. (2.16):

$$J = m\sigma_Y \delta \quad (2.16)$$

where  $m$  is a dimensionless parameter determined by the stress state and material properties. Equation (2.16) applies to fracture processes well beyond the validity limits of LEFM [5].

### 2.1.3 Failure in Fiber Reinforced Plastics

Predicting failure in Fiber Reinforced Plastic (FRP) is quite complex when compared to predicting failure in homogeneous isotropic materials. One of the challenging aspects of computing the strength of a composite, is the multitude of differing failure mechanisms simultaneously at work. In Figure 2.4 some of the failure mechanisms that can occur in fiber-reinforced composites are illustrated.

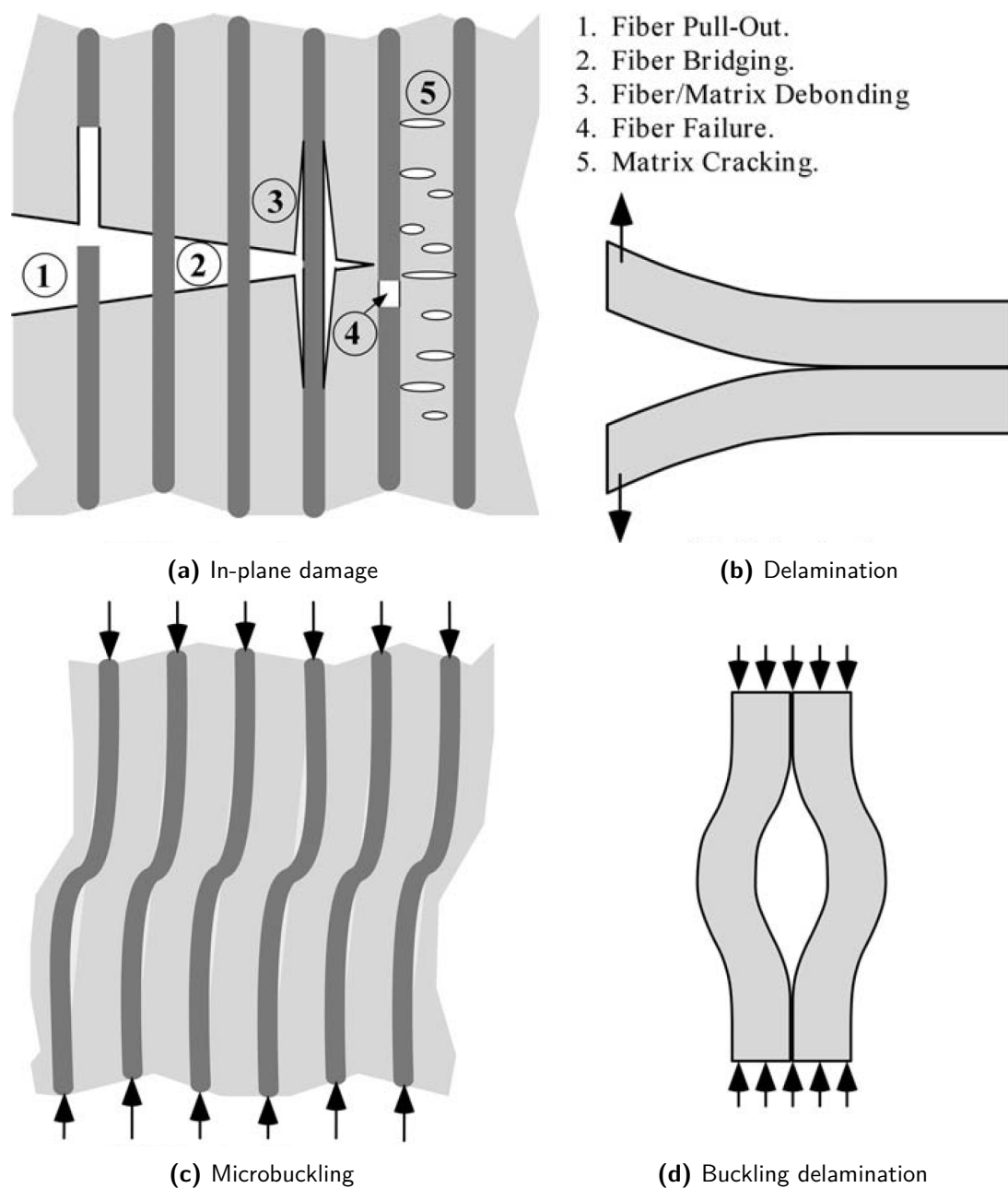


**Figure 2.4:** Examples of damage and fracture mechanisms in fiber-composites [5]

Global failure of lamina is often the result of damage coalescence and interaction of multiple mechanisms. Analytical methods have been developed to compute the strength allowables inside a ply for each of the failure modes shown in Figure 2.4. The allowables computed using these analytical criteria are directional and do not allow for any failure-mode interaction. Phenomenological failure criteria descended from the desire to have a strength allowable for a lamina in any arbitrary direction, based on a number of basic and experimentally obtainable strength parameters. Common lamina failure theories can be classified in three distinctive groups [17]:

- Limit or noninteractive theories (e.g. Maximum Stress/Maximum Strain)
- Interactive theories (e.g. Tsai-Hill [67], Tsai-Wu [68])
- Partially interactive failure-mode-based theories (e.g. Hashin-Rotem [33], Puck [58])

According to the maximum stress and strain theories, failure occurs when respectively principal stresses or strains exceed the corresponding ultimate values in that direction. The maximum strain theory allows for some interaction of stress components caused by Poisson's ratio effects [17].

Hill [35] proposed a modification to the Von Mises yield criterion for anisotropic metals, given by Eq. (2.17):

$$A\sigma_{11}^2 + B\sigma_{22}^2 + C\sigma_{11}\sigma_{22} + D\tau_{66}^2 = 1 \quad (2.17)$$

where  $A$ ,  $B$ ,  $C$  and  $D$  are material parameters corresponding to the anisotropy. Tsai [67] used this as a basis to come up with a failure criterion for composites, known as the Tsai-Hill failure criterion, which is given by Eq. (2.18).

$$\frac{\sigma_{11}^2}{F_{11}^2} + \frac{\sigma_{22}^2}{F_{22}^2} - \frac{\sigma_{11}\sigma_{22}}{F_{11}^2} + \frac{\tau_{66}^2}{F_{66}^2} = 1 \quad (2.18)$$

Tsai and Wu [68] developed a modified polynomial tensor theory with linear terms to allow for a distinction between tensile and compressive strengths. For a two-dimensional stress state the Tsai-Wu failure criterion is given by Eq. (2.19).

$$\begin{aligned} \frac{1}{F_{11,t}F_{11,c}}\sigma_{11}^2 + \frac{1}{F_{22,t}F_{22,c}}\sigma_{22}^2 + \left(\frac{1}{F_{11,t}} - \frac{1}{F_{11,c}}\right)\sigma_{11} + \left(\frac{1}{F_{22,t}} - \frac{1}{F_{22,c}}\right)\sigma_{22} \\ + \frac{1}{F_{66}^2}\tau_{66} - \sqrt{\frac{1}{F_{11,t}F_{11,c}}\frac{1}{F_{22,t}F_{22,c}}}\sigma_{11}\sigma_{22} = 1 \end{aligned} \quad (2.19)$$

Hashin and Rotem [33] proposed using two failure criteria in parallel, one for the fiber failure and one for inter-fiber failure.

$$\frac{|\sigma_{11}|}{F_{11}} = 1 \quad (2.20a)$$

$$\left(\frac{\sigma_{22}}{F_{22}}\right)^2 + \left(\frac{\tau_{66}}{F_{66}}\right)^2 = 1 \quad (2.20b)$$

In these equations the normal strengths ( $F_{11}$  and  $F_{22}$ ) are equal to the tensile or compressive value depending to the state of stress.

The Puck failure criterion [58] also distinguishes between fiber and interfiber failures and allows for non-linear stress strain relationships. The need for extra material parameters make the Puck approach less attractive than the Hashin-Rotem failure theory for practical applications.

## 2.2 Cohesive Element Modeling

This section deals with the implementation of the Cohesive Zone Model (CZM) in the Finite Element Method (FEM), with the purpose of modeling fracture. The CZM was proposed to handle non-linear fracture behavior and is an idealization of damage processes in front of the crack-tip. The CZM will be discussed in detail in Section 2.2.1.

CZMs have been implemented in the FEM by cohesive elements. Cohesive elements were primarily developed for analyzing finite-thickness cohesive interfaces, such as bond-lines, but found their way into computational fracture modeling in the form of zero-thickness cohesive elements. The cohesive elements are introduced at the boundaries of continuum elements. Examples of the usage of cohesive elements for computational fracture analysis can be found in references [2, 4, 73]. The element formulation of zero-thickness cohesive elements is included in Section 2.2.2.

A distinction can be made between intrinsic and extrinsic methods. Intrinsic methods have the cohesive elements included in the mesh prior to the loading whereas extrinsic methods add cohesive elements to the mesh during the simulated crack growth. Both methods have consequential advantages and disadvantages, which will be discussed in Section 2.2.3.

### 2.2.1 Cohesive Zone Models

For typical materials some sort of non-linear behavior is to be expected at the crack-tip, caused by yielding, micro-cracking and void nucleation, growth and coalescence. When modeling fracture using LEFM, the assumption is made that the non-linear behavior at the crack-tip is sufficiently small compared to the structural dimensions. In a CZM the softening mechanisms in front of the crack are lumped into a discrete line/plane and models separation by a stress-displacement relationship [18]. According to Xie and Waas [82], if the length scale  $l^*$  is larger than any of the characteristic dimensions in the problem, LEFM is no longer valid and CZMs are required Eq. (2.21).

$$l^* = \frac{E\Gamma}{\sigma_c^2} \quad (2.21)$$

Pioneering work for a CZM in elastic-plastic materials was performed by the the Russian mathematician Barenblatt during his time at the Academy of Sciences, Moscow, U.S.S.R. The original article (1961) was translated to English a year later [6]. Dugdale [21] came up with a relation for the extent of plastic yielding at the tip of a slit in a steel sheet, using stress functions proposed in Soviet-Georgian mathematician Muskhelishvili's book [47]. The first work for quasi-brittle materials was done by Hillerborg et al. [37].

The CZM idealizes the contribution of the various types of damage, which form in front of the crack-tip, as a loss in stiffness. Material at the crack-tip is assumed to open up according to

a cohesive constitutive relation, which is also referred to as Traction-Separation Law (TSL). CZMs have been implemented in the FEM, by allowing elements to split at the element boundaries, with load being transferred by interface elements through cohesive tractions as shown in Figure 2.5. The interface elements are always one dimension smaller than the elements they connect.

The rightmost section in Figure 2.5 depicts examples of two cohesive laws, one for ductile fracture (top) and one for brittle fracture (bottom). The failure process of an interface element is completed when the element can no longer support any traction (in the figure:  $\delta/\delta_0 = 1$ ). When considering brittle decohesion relations, the shape of the TSL can play a large role and can, in some cases, be more important than the ultimate traction strength [18] - therefore a review of different kinds of TSLs is necessary.

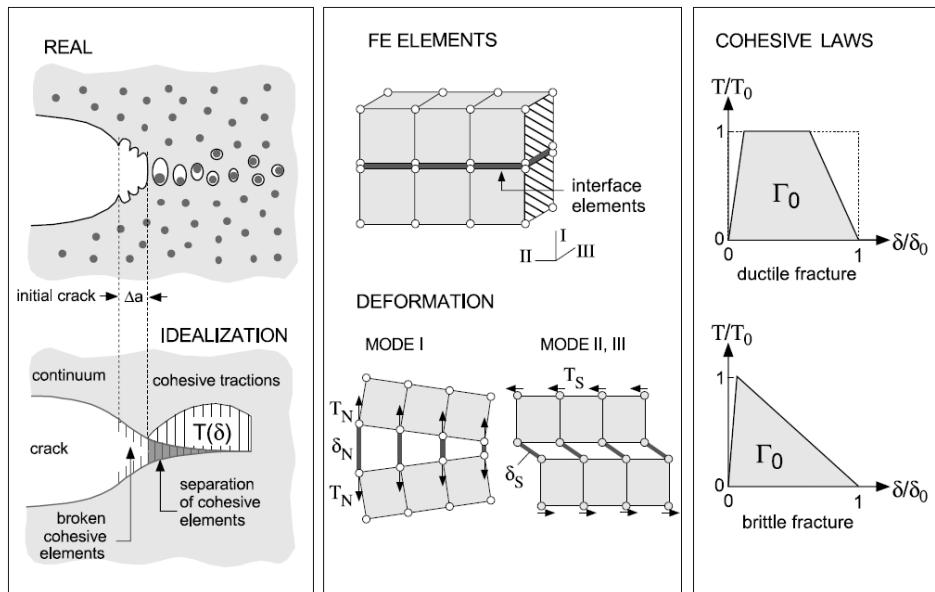


**Figure 2.5:** Representation of the ductile failure process by the CZM [15]

Cohesive constitutive relationships have some general required characteristics, which were summarized by Park and Paulino [55]:

- The traction separation relationship is independent of any superposed rigid body motion.
- The work to create a new surface is finite, and it's value corresponds to the fracture energy, i.e. area under the traction-separation curve.
- The mode I fracture energy is usually different from the mode II fracture energy.
- A finite characteristic length scale exists, which leads to a complete failure condition, i.e. no load-bearing capacity.
- The cohesive traction across the fracture surface generally decreases to zero while the separation increases under the softening condition, which results in negative stiffness.

- A potential for the cohesive constitutive relationship may exist, and thus the energy dissipation associated with unloading/reloading is independent of a potential.

TSLs can be classified as either non-potential based or potential based models. Non-potential based methods are relatively simple and take the form of one-dimensional effective displacement relations. The potential based methods use a potential function to obtain traction-separation relationships. The first derivative provides the traction over the fracture surface, while the second derivative provides the constitutive relationship [55].

- Non-potential or one-dimensional effective displacement TSLs:
  - Cubic polynomial [70]
  - Trapezoidal [71]
  - Smoothed trapezoidal [63]
  - Exponential [53]
  - Linear softening [10, 27, 23]
  - Bi-linear softening [57, 81]
- General potential-based TSLs:
  - Polynomial [48, 26]
  - Based on universal binding energy [62, 49, 83, 7]
  - Park-Paulino-Roesler (PPR) unified potential-based [56]

There have been a number of cohesive constitutive relationships developed using an effective displacement ( $\bar{\Delta}$ ) and an effective Traction ( $\bar{T}$ ), which are listed above. Tvergaard [70] related the effective components ( $\bar{T}$ ,  $\bar{\Delta}$ ) to the normal and tangential components given respectively by Eq. (2.22) and Eq. (2.23).

$$T_n = \frac{\bar{T}(\bar{\Delta})}{\bar{\Delta}} \frac{\Delta_n}{\delta_n} \quad (2.22)$$

$$T_t = \frac{\bar{T}(\bar{\Delta})}{\bar{\Delta}} \alpha_e \frac{\Delta_t}{\delta_t} \quad (2.23)$$

In these relations the subscripts  $n$  and  $t$  are used to denote normal and tangential components, i.e.  $T_n$  and  $T_t$  are the tractions and  $\Delta_n$  and  $\Delta_t$  are the displacements in normal and tangential directions respectively. The normal and tangential characteristic lengths associated with the fracture energy and the cohesive strengths are  $\delta_n$  and  $\delta_t$ . The non-dimensional constant  $\alpha_e$  gives the mode-mixity (Mode I & II).

Tvergaard [70] then introduced the non-dimensional effective displacement Eq. (2.24), using the Pythagorean Theorem. Tvergaard [70] defined effective traction as a cubic function of the effective displacement Eq. (2.25), which provides the shape of the TSL (Figure 2.6a).

$$\bar{\Delta} = \sqrt{\left(\frac{\Delta_n}{\delta_n}\right)^2 + \left(\frac{\Delta_t}{\delta_t}\right)^2} \quad (2.24)$$

$$\bar{T} = \frac{27}{4} \sigma_{\max} \bar{\Delta} (1 - 2\bar{\Delta} + \bar{\Delta}^2) \quad (2.25)$$

Tvergaard and Hutchinson [71] extended the use of Eq. (2.22) and Eq. (2.23) by modifying the effective traction relationship and using the mode-mixity, given by Eq. (2.26), resulting from a one-dimensional potential based model described in the same paper [71].

$$\alpha_e = \frac{\delta_n}{\delta_t} \quad (2.26)$$

Resulting in a symmetric system, i.e.

$$\frac{\partial T_n}{\partial \Delta_t} = \frac{\partial T_t}{\partial \Delta_n}$$

A model like this is not suitable when fracture energies along normal and tangential directions are different, which is generally the case as previously mentioned.

Tvergaard and Hutchinson [71] used trapezoidal shape models (Figure 2.6b), in combination with their one-dimensional potential based method, to describe fracture in elasto-plastic materials.

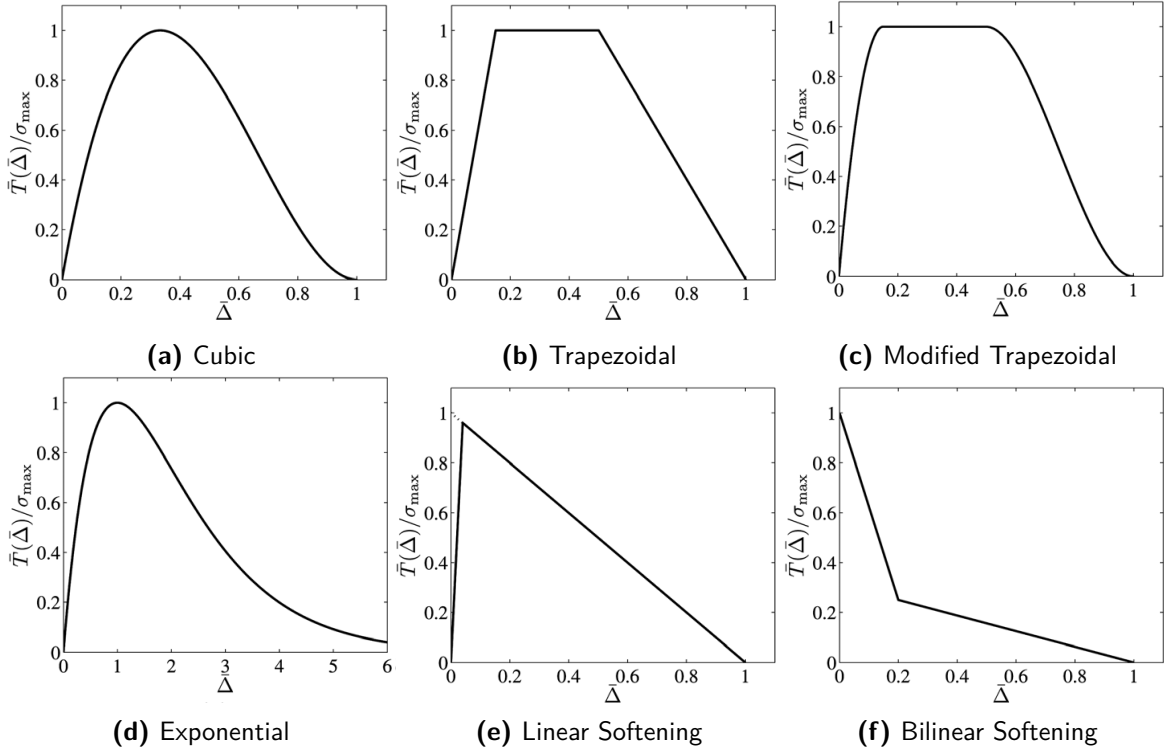


**Figure 2.6:** One-Dimensional Effective Displacement TSLs [55]

The linear softening model by Geubelle and Baylor [27] makes use of an internal residual strength variable ( $D_s$ ), which is defined by Eq. (2.27).

$$D_s = \min(D_{\min}, \max(0, 1 - \bar{\Delta})) \quad (2.27)$$

The normal and tangential tractions are given by:

$$T_n = \sigma_{\max} \frac{D_s}{1 - D_s} \frac{\Delta_n}{\delta_n} \quad (2.28)$$

$$T_t = \tau_{\max} \frac{D_s}{1 - D_s} \frac{\Delta_t}{\delta_t} \quad (2.29)$$

The parameter  $D_{\min}$  is related to the effective displacement for which the maximum cohesive traction is reached, i.e. the cohesive strength. When the effective displacement is smaller than  $(1 - D_{\min})$ , the cohesive traction increases with the effective displacement, following the artificial initial elastic range, visible in Figure 2.6e. After the cohesive strength is reached, the softening condition starts and the cohesive traction can be expressed as:

$$T_n = \sigma_{\max} \frac{1 - \Delta}{\Delta} \frac{\Delta_n}{\delta_n} \quad (2.30)$$

$$T_t = \tau_{\max} \frac{1 - \Delta}{\Delta} \frac{\Delta_t}{\delta_t} \quad (2.31)$$

which is a special case of Eq. (2.22) and Eq. (2.23) respectively, with  $\alpha_e = \tau_{\max}/\sigma_{\max}$  and

$$\bar{T} = \sigma_{\max}(1 - \bar{\Delta})$$

This type of cohesive constitutive law has been used to model fracture in polycrystalline brittle materials by Espinosa and Zavattieri [23].

### 2.2.2 Cohesive Element Formulation

The governing equations of a cracked solid include the equilibrium equation, the natural and essential boundary conditions and traction continuity on the cracked surface [50]:

$$\nabla \cdot \boldsymbol{\sigma} + \mathbf{b} = 0 \quad \mathbf{x} \in \Omega \quad (2.32a)$$

$$\mathbf{n} \cdot \boldsymbol{\sigma} = \bar{\mathbf{t}} \quad \mathbf{x} \in \Gamma_t \quad (2.32b)$$

$$\mathbf{u} = \bar{\mathbf{u}} \quad \mathbf{x} \in \Gamma_u \quad (2.32c)$$

$$\mathbf{n}_d^+ \cdot \boldsymbol{\sigma} = \mathbf{t}_c^+; \quad \mathbf{n}_d^- \cdot \boldsymbol{\sigma} = \mathbf{t}_c^-; \quad \mathbf{t}_c^+ = -\mathbf{t}_c = -\mathbf{t}_c^- \quad \mathbf{x} \in \Gamma_d \quad (2.32d)$$

where  $\boldsymbol{\sigma}$  is the Cauchy stress tensor,  $\mathbf{b}$  the body force vector and  $\mathbf{u}$  the displacement field. The applied tractions and displacements on the boundaries are denoted  $\bar{\mathbf{t}}$  and  $\bar{\mathbf{u}}$  respectively. The cohesive traction on the crack boundary  $\Gamma_d$  is  $\mathbf{t}_c$ , with normal vector  $\mathbf{n}_d$  as shown in Figure 2.7.

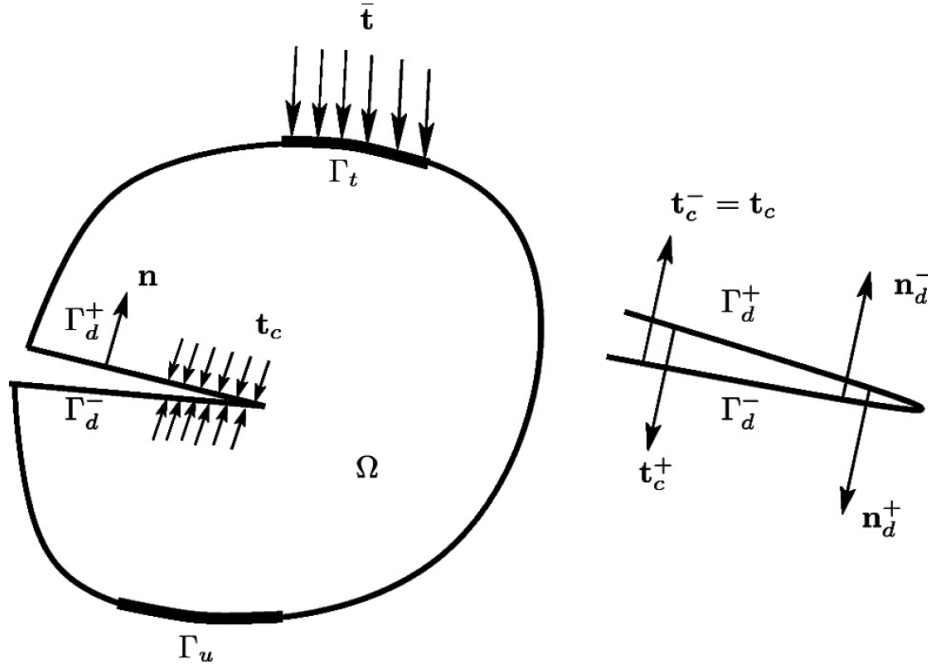


Figure 2.7: A two-dimensional solid containing a cohesive crack [50]

The weak form of the governing equation was derived in [8] and is given by:

$$\delta W^{\text{ext}} = \delta W^{\text{int}} + \delta W^{\text{coh}} \quad (2.33)$$

with:

$$\delta W^{\text{ext}} = \int_{\Omega} \delta \mathbf{u} \cdot \mathbf{b} \, d\Omega + \int_{\Gamma_t} \delta \mathbf{u} \cdot \mathbf{t} \, d\Gamma_t \quad (2.34a)$$

$$\delta W^{\text{int}} = \int_{\Omega} \nabla^s \delta \mathbf{u} : \boldsymbol{\sigma} \, d\Omega \quad (2.34b)$$

$$\delta W^{\text{coh}} = \int_{\Gamma_d} \delta [\![\mathbf{u}]\!] \cdot \mathbf{t}^c \, d\Gamma_d \quad (2.34c)$$

where  $[\![\mathbf{u}]\!]$  is the displacement jump over the crack. The solid is discretized by standard continuum elements, whereas the crack is discretized using zero-thickness interface elements as shown in Figure 2.8. In the figure the continuum elements are two-dimensional quads, whereas the zero-thickness interface elements are one-dimensional.

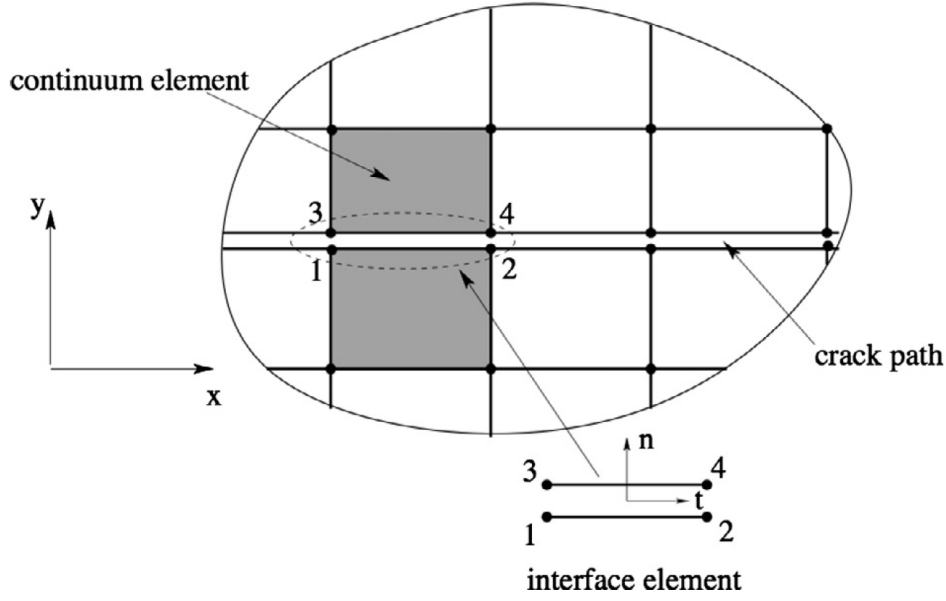


**Figure 2.8:** Discretization of the solid into continuum elements and zero-thickness interface elements [50]

The nodal displacements on the upper and lower faces of the interface element are given by Eq. (2.35). To make a distinction "+" denotes upper and the "-" denotes lower, as these elements are zero-thickness and the distance between the upper and lower faces is infinitesimally small for a closed interface element.

$$\mathbf{u}^+ = \mathbf{N}^{\text{int}} \mathbf{u}^+ \quad (2.35a)$$

$$\mathbf{u}^- = \mathbf{N}^{\text{int}} \mathbf{u}^- \quad (2.35b)$$

Where  $\mathbf{N}^{\text{int}}$  is the matrix of shape functions:

$$\mathbf{N}^{\text{int}} = \begin{bmatrix} N_1 & 0 & N_2 & 0 \\ 0 & N_1 & 0 & N_2 \end{bmatrix} \quad (2.36)$$

with  $N_1$  and  $N_2$  being the two-node line element shape functions  $N_1(\xi)$  and  $N_2(\xi)$ .

Using the displacement on the upper and lower crack faces, the displacement jump can be written as:

$$[[\mathbf{u}]] = \mathbf{u}^+ - \mathbf{u}^- = \mathbf{N}^{\text{int}}(\mathbf{u}^+ - \mathbf{u}^-) \quad (2.37)$$

The displacement of the continuum elements and the virtual displacements are given by Eq. (2.38).

$$\mathbf{u} = \mathbf{N}\mathbf{u} \quad (2.38a)$$

$$\delta\mathbf{u} = \mathbf{N}\delta\mathbf{u} \quad (2.38b)$$

Substituting Eq. (2.35) and Eq. (2.38) into the weak formulation Eq. (2.33) provides:

$$\mathbf{f}^{\text{ext}} = \mathbf{f}^{\text{int}} + \mathbf{f}^{\text{coh}} \quad (2.39)$$

Where  $\mathbf{f}^{\text{ext}}$ ,  $\mathbf{f}^{\text{int}}$  and  $\mathbf{f}^{\text{coh}}$  are the external, internal and cohesive forces.

The internal and external force vectors are computed from elemental contributions as is done with standard FEM:

$$\mathbf{f}_e^{\text{int}} = \int_{\Omega_e} \mathbf{B}^T \boldsymbol{\sigma} \, d\Omega_e \quad (2.40)$$

$$\mathbf{f}_e^{\text{ext}} = \int_{\Omega_e} \mathbf{N}^T \mathbf{b} \, d\Omega_e + \int_{\Gamma_t^e} \mathbf{N}^T \mathbf{t} \, d\Gamma_t^e \quad (2.41)$$

The cohesive force vector is assembled from all the contributions of interface elements. For an arbitrary interface element (subscript  $ie$ ), the cohesive force vector is given by Eq. (2.42).

$$\mathbf{f}_{ie,+}^{\text{coh}} = \int_{\Gamma_d} (\mathbf{N}^{\text{int}})^T \mathbf{t}^c \, d\Gamma_d \quad (2.42a)$$

$$\mathbf{f}_{ie,-}^{\text{coh}} = - \int_{\Gamma_d} (\mathbf{N}^{\text{int}})^T \mathbf{t}^c \, d\Gamma_d \quad (2.42b)$$

The nonlinear behavior is assumed to be limited to the cohesive crack interface, i.e. the continuum elements have simple linear elastic material behavior. The behavior of the interface elements is modeled with a TSL. The constitutive equations in rate form are then given by Eq. (2.43) and Eq. (2.44).

$$\dot{\boldsymbol{\sigma}} = \mathbf{D} \dot{\boldsymbol{\epsilon}} \quad (2.43)$$

$$\dot{\mathbf{t}}^c = \mathbf{T} [\dot{\mathbf{u}}] \quad (2.44)$$

Where  $\mathbf{D}$  is the bulk tangent matrix or stiffness matrix and  $\mathbf{T}$  is the cohesive tangent matrix whose form is determined by the TSL.

For the continuum elements the standard material tangent stiffness matrix is obtained by linearization of the internal force vector and is given by:

$$\mathbf{K}_e = \int_{\Omega} \mathbf{B}_e^T \mathbf{D} \mathbf{B}_e \, d\Omega \quad (2.45)$$

Substituting Eq. (2.37) in Eq. (2.44) yields:

$$\dot{\mathbf{t}}^c = \mathbf{T} \mathbf{N}^{\text{int}} (\dot{\mathbf{u}}^+ - \dot{\mathbf{u}}^-) \quad (2.46)$$

Transformation to the global coordinate system is performed using rotation matrix  $\mathbf{Q}$ .

$$\dot{\mathbf{t}}^c = \mathbf{Q} \mathbf{T} \mathbf{Q}^T \mathbf{N}^{\text{int}} (\dot{\mathbf{u}}^+ - \dot{\mathbf{u}}^-) \quad (2.47)$$

Where  $\mathbf{Q}$  is given by:

$$\mathbf{Q} = [\mathbf{n} \quad \mathbf{s} \quad \mathbf{t}] \quad (2.48)$$

with  $\mathbf{n}$ ,  $\mathbf{s}$  and  $\mathbf{t}$  the unit normal vector and the two unit tangential vectors of the interface element respectively.

The linearization of the cohesive force vector requires differentiating the forces with respect to the the nodal displacements ( $\mathbf{u}^+$  and  $\mathbf{u}^-$ ):

$$\begin{bmatrix} \frac{\partial \mathbf{f}_{ie,+}^{\text{coh}}}{\partial \mathbf{u}} \\ \frac{\partial \mathbf{f}_{ie,-}^{\text{coh}}}{\partial \mathbf{u}} \end{bmatrix} = \begin{bmatrix} \frac{\partial \mathbf{f}_{ie,+}^{\text{coh}}}{\partial \mathbf{u}^+} & \frac{\partial \mathbf{f}_{ie,+}^{\text{coh}}}{\partial \mathbf{u}^-} \\ \frac{\partial \mathbf{f}_{ie,-}^{\text{coh}}}{\partial \mathbf{u}^+} & \frac{\partial \mathbf{f}_{ie,-}^{\text{coh}}}{\partial \mathbf{u}^-} \end{bmatrix} \begin{bmatrix} \delta \mathbf{u}^+ \\ \delta \mathbf{u}^- \end{bmatrix} \quad (2.49)$$

The resulting cohesive element tangent stiffness matrix is given by Eq. (2.50).

$$\mathbf{K}_{ie}^{\text{coh}} = \begin{bmatrix} \int_{\Gamma_d} \mathbf{N}^T \mathbf{Q} \mathbf{T} \mathbf{Q}^T \mathbf{N} \, d\Gamma_d & - \int_{\Gamma_d} \mathbf{N}^T \mathbf{Q} \mathbf{T} \mathbf{Q}^T \mathbf{N} \, d\Gamma_d \\ - \int_{\Gamma_d} \mathbf{N}^T \mathbf{Q} \mathbf{T} \mathbf{Q}^T \mathbf{N} \, d\Gamma_d & \int_{\Gamma_d} \mathbf{N}^T \mathbf{Q} \mathbf{T} \mathbf{Q}^T \mathbf{N} \, d\Gamma_d \end{bmatrix} \quad (2.50)$$

### 2.2.3 Intrinsic and Extrinsic Methods

All the TSLs /constitutive relationships that have been discussed until now have been intrinsic methods [48, 70, 71, 27, 83]. In intrinsic methods the TSL includes an initial elastic deformation for which the element opens up, i.e. the TSL starts in the origin with a hardening portion. When a certain separation is reached, the cohesive traction will equal the maximum cohesive strength of the material. The TSL then follows a weakening/softening, which is associated with the failure process. The softening process continues until the traction has completely vanished, at which point the critical separation ( $\delta_c$ ) has been reached. The traction-free surface that is created during this process, is the crack surface [41].

The most consequential disadvantage of the intrinsic approach is that the initial elastic slope in the constitutive relation can result in an artificial compliance [51, 86, 61]. Moreover, the elastic portion of the TSL affects the propagation of elastic stress-waves in the continuum, resulting in a crack-tip speed divergent from the Rayleigh Wave speed [51]. One possible solution to minimize artificial compliance and improve the wave-speed approximation, is to increase the "dummy" stiffness of the initial elastic behavior. Unfortunately for dynamic problems, increasing the dummy stiffness will result in severe stable-time-step restrictions.

The extrinsic approach models the softening/failure portion of the TSL only. In such a model the cohesive traction equals the material strength. A number of models have been proposed to represent the damage dependence of cohesive strength. Initially Dugdale [21] and Barenblatt [6] assumed a constant cohesive strength up to the displacement jump, where the traction is suddenly reduced to zero. Yoshiaki and Aki [85] modified this constitutive relation by adding a softening portion to the TSL, where the traction is linearly reduced to zero. However, the most common model of the extrinsic type used in fracture problems is the linear model [41]. In this model the traction is linearly reduced from the ultimate strength value for a completely closed cohesive element, to zero traction at the critical separation.

Extrinsic cohesive fracture simulations require cohesive elements to be adaptively inserted into the mesh as the crack propagates. There are no issues with artificial compliance for extrinsic cohesive element models, as the extrinsic cohesive elements are absent in the uncracked solid. The absence of embedded cohesive elements makes this type of modeling more suitable for explicit dynamic analysis, where larger time-steps can save a lot of computational time. Nguyen [51] used a hybrid discontinuous Galerkin and an extrinsic cohesive zone model and applied it to microcracking in fiber-reinforced composite materials.

Although compliance and stability is improved, extrinsic methods come at a cost in parallelization. Current massively parallel environments are based on so-called distributed memory architectures [25], i.e. each processor of a computing node has its own allocated region of the global system memory. Processors on different nodes communicate over a network, by sending messages to receive data. In the scope of a FEM, the model/mesh is divided into a number of regions, which are distributed over the available processors. Obviously, adaptations to the mesh in an extrinsic cohesive fracture simulation would need to be communicated between the processors, making it computationally expensive.

### 2.2.4 Mesh dependency

When compared to the eXtended Finite Element Method (XFEM) or meshless methods, cohesive element fracture modeling presents a disadvantage when it comes to mesh dependency. Cohesive elements are inserted on the boundaries of continuum elements and as such, the crack can only propagate by following element boundaries. The advantage of knowing the preferred crack path or direction is that intrinsic cohesive elements can be placed only where needed, minimizing the risk of artificial compliance. Examples of this advantage in action include glued interfaces under a peel tress or a crack propagation problem for a simple pre-cracked specimen, as was done in sources [84, 53].

In problems where the crack path is unknown, the orientation of the mesh becomes an important factor. This is illustrated in Figure 2.9, where the shortest distance between two points is compared to the shortest distance over the mesh. Even from a LEFM point of view, it is clear that forcing a crack to follow a longer path due to the discretization of the continuum, will in general require more energy per unit crack extension when compared to the original continuum. The introduction of a discrete mesh necessarily leads to a larger energy dissipation of the discrete model when compared to the continuum. This effect is known as *mesh-induced toughness* [61].

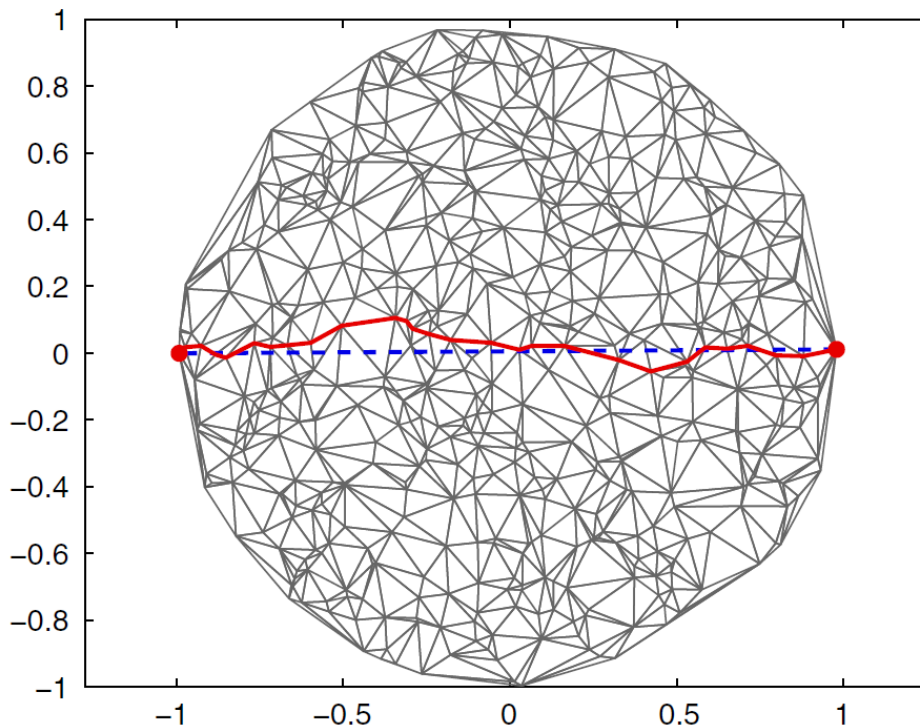


**Figure 2.9:** Shortest Euclidean distance and shortest path over the mesh between two random points [61]

In structured meshes the error is minimized for a preferred crack-direction aligned with the mesh. Conversely, the error will be maximized for a preferred crack-direction exactly in-between element boundary directions. The effect of a structured mesh on the error is known as *mesh-induced anisotropy* [61].

Rimoli and Rojas [61] constructed an improved meshing strategy by applying a barycentric subdivision to a K-means mesh. The obtained mesh is referred to as a *conjugate-directions* mesh. With this meshing strategy, the mesh-induced anisotropy is completely removed and the mesh-induced toughness is approximately halved when compared to a random mesh.

## 2.3 Multiscale Approach to Fracture

This section deals with the multiscale method used for spatial scale coupling in this thesis project. First, the different multiscale concepts will be explained briefly in Section 2.3.1. The fundamentals of computational homogenization will be given in Section 2.3.2. The existence and size of a Representative Volume Element (RVE) will be discussed in Section 2.3.3, followed by periodicity of boundary conditions in Section 2.3.4. In the last section, some concluding remarks regarding the method of choice will be presented.

### 2.3.1 Multiscale Concepts

The mesoscopic failure response of fiber-reinforced plastics is characterized by coalescing failure events at the microscopic level, including fiber debonding, matrix cracking and fiber pull-out. The optimization of the design and manufacturing of fiber-reinforced composites requires a detailed understanding of these failure modes [4]. One approach to incorporate microscopic failure modes is to model the heterogeneities of the microscopic scale explicitly in the macroscopic scale, an approach referred to as Direct Numerical Simulation (DNS) or brute-force fullscale simulation [52]. Even with the current capabilities of supercomputers, the DNS is rarely an option due to the cost of memory and computational time [43], allowing the concept of a multiscale to come into play.

As previously mentioned, failure in fiber-reinforced plastics spans multiple spatial scales and can be classified as a multi-scale phenomenon. A multiscale model is a numerical tool that can handle problems spanning multiple scales, both spatial and temporal [43]. In a multiscale analysis only part of the microscale complexity is carried over to the macroscale [75]. The analysis assumes the existence of a RVE, that is much smaller than the structure and simultaneously large enough to be constitutively valid, in which the microstructure is incorporated. Computational analysis performed on this RVE can be used to describe macroscopic behavior, such as constitutive relations for cohesive fracture (see Figure 2.10) [29].

In a multiscale model, information must be exchanged between the length scales. Homogenization is one of the techniques to create coupling and dates back to the rules of mixtures developed by Voigt [76] (1889) and Reuss [59] (1929) to find effective macroscale properties. In more recent history, unit cell methods have been developed that employ numerical solutions at the microscale to determine effective material properties and homogenized constitutive laws. A major disadvantage of the unit cell method is the necessity to make assumptions regarding the form of the macroscopic constitutive behavior, making it less appropriate for non-linear problems [75].

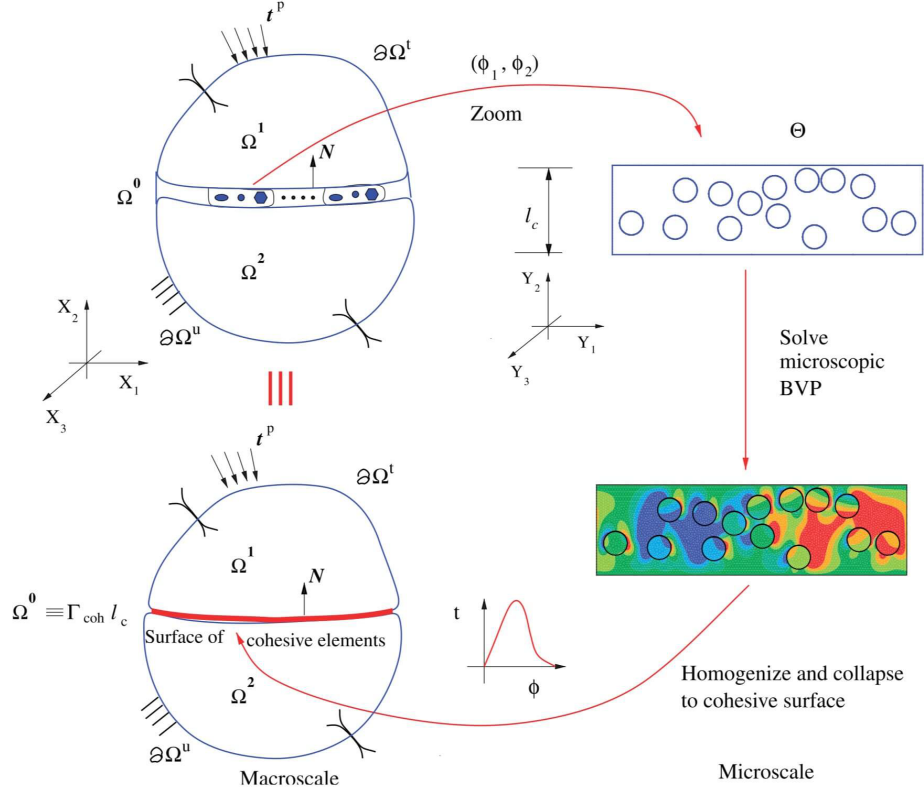


**Figure 2.10:** The multiscale cohesive scheme: The left half shows the macroscopic modeling, whereas the right half depicts microscopic modeling details in the RVE [43]

Computational homogenization on a microstructural volume element can overcome the aforementioned limitations of unit cell methods and will be discussed in more detail in the next section.

### 2.3.2 Computational Homogenization of Fracture Processes

Quasi-static equilibrium of body  $\Omega^M$ , with internal boundary  $\Gamma_d^M$  representing a cohesive crack, boundary conditions on  $\Gamma_{\bar{u}}^M$  and applied traction on  $\Gamma_{\bar{t}}^M$  is given by Eq. (2.51) [75]. The body is portrayed in Figure 2.11.

$$\operatorname{div}(\boldsymbol{\sigma}^M) = \mathbf{b}^M \quad \mathbf{x}^M \in \Omega^M \quad (2.51a)$$

$$\boldsymbol{\sigma}^M \cdot \mathbf{n}^M = \mathbf{t}^M(\tilde{\mathbf{u}}^M) \quad \mathbf{x}^M \in \Gamma_d^M \quad (2.51b)$$

$$\boldsymbol{\sigma}^M \cdot \mathbf{n}^M = \bar{\mathbf{t}}^M \quad \mathbf{x}^M \in \Gamma_{\bar{t}}^M \quad (2.51c)$$

$$\mathbf{u}^M = \bar{\mathbf{u}}^M \quad \mathbf{x}^M \in \Gamma_{\bar{u}}^M \quad (2.51d)$$

The (cohesive) traction on  $\Gamma_d^M$  is a function of the displacement jump  $\tilde{\mathbf{u}}^M$ .

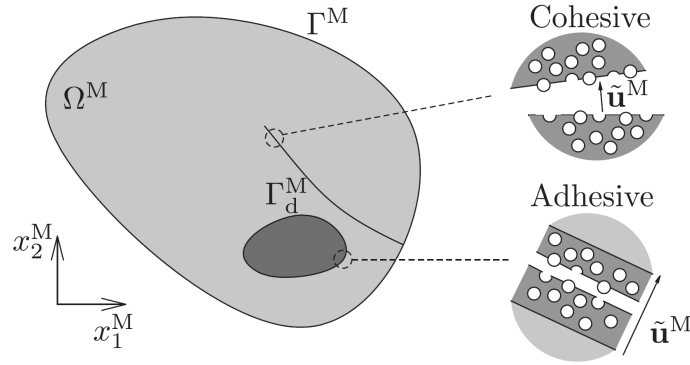


**Figure 2.11:** Schematic representation of the macroscale model. The internal boundary  $\Gamma_d^M$  represents the cohesive crack [75]

The microscale model incorporates failure models with a localized damage zone and is consistent with the macroscale formulation, i.e. the microscale model must show softening behavior. This microscale model will be referred to as the RVE and is shown schematically in the leftmost portion of Figure 2.12. Defining the size of the RVE is not straightforward and as such, the method for doing so will be discussed in detail in Section 2.3.3.

Quasi-static equilibrium of the microscale model or RVE is given by Eq. (2.52) [75].

$$\operatorname{div}(\boldsymbol{\sigma}^m) = \mathbf{b}^m \quad \mathbf{x}^m \in \Omega^m \quad (2.52a)$$

$$\boldsymbol{\sigma}^m \cdot \mathbf{n}^m = \mathbf{t}^m(\tilde{\mathbf{u}}^m) \quad \mathbf{x}^m \in \Gamma_d^m \quad (2.52b)$$

$$\mathbf{u}^m = \tilde{\mathbf{u}}^m \quad \mathbf{x}^m \in \Gamma_{\tilde{\mathbf{u}}}^m \quad (2.52c)$$

These relations resemble the macroscale equilibrium equations, with the lowercase  $m$  denoting microscale ( $M$ : macroscale). The microscale is fundamentally different in that the microscale Cauchy stress  $\boldsymbol{\sigma}^m$  and traction  $\mathbf{t}^m$  are analytically derived (averaged) quantities. The multiscale framework solely uses displacement boundary conditions (including periodic) and introduces stress by prescribed displacements at the corner nodes of the RVE [75].

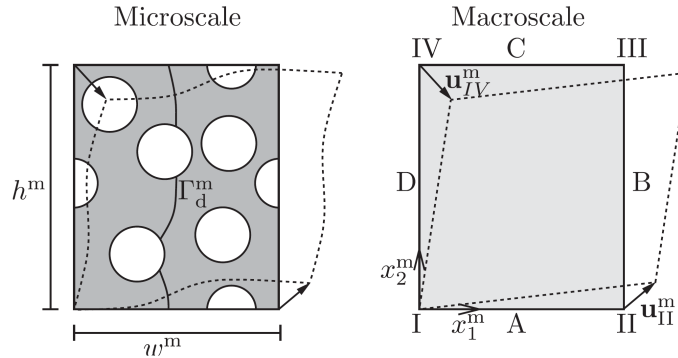


**Figure 2.12:** Schematic representation of the homogenization of bulk material properties [75]

The bulk constitutive behavior of the RVE is shown in Figure 2.12. Although the figure only shows one cohesive crack, the approach is not limited to a single discontinuity. For periodic geometry and periodic boundary conditions, which will be discussed in Section 2.3.4, the homogenized engineering strain  $\langle \boldsymbol{\epsilon}^m \rangle_{\Omega^m}$  is defined as the volume average of the corresponding microscopic fields. In this equation the divergence theorem is used to rewrite the volume integral as a boundary integral. Since the periodic boundary conditions will integrate to zero, the homogenized strain can be expressed as a function of the nodal displacement of the corner nodes [75]:

$$\langle \boldsymbol{\epsilon}^m \rangle_{\Omega^m} = \frac{1}{w^m h^m} \int_{\Omega^m} \boldsymbol{\epsilon}^m d\Omega^m = \frac{1}{w^m} \mathbf{a}_{\text{II}}^m \otimes^s \mathbf{n}^M + \frac{1}{h^m} \mathbf{a}_{\text{IV}}^m \otimes^s \mathbf{s}^M \quad (2.53)$$

where  $\mathbf{a}_{\text{II}}^M$  and  $\mathbf{a}_{\text{IV}}^M$  are the displacements of the finite element nodes at points II and IV, with numbering given by Figure 2.12. The vectors  $\mathbf{n}^M$  and  $\mathbf{s}^M$  are the macroscopic normal and orthogonal shear vectors and  $\otimes^s$  is the symmetric dyadic product.

The homogenized Cauchy stress is derived using the Hill-Mandel energy condition [36]. To formulate the reduced expression given by Eq. (2.54), the divergence theorem and microscale equilibrium were used to rewrite the volume integral along with the anti-periodicity of the traction following from the periodic boundary conditions [75].

$$\langle \boldsymbol{\sigma}^m \rangle_{\Omega^m} = \frac{1}{w^m h^m} \int_{\Omega^m} \boldsymbol{\sigma}^m d\Omega^m = \frac{1}{w^m} \mathbf{f}_B^m \otimes \mathbf{n}^M + \frac{1}{h^m} \mathbf{f}_C^m \otimes \mathbf{s}^M \quad (2.54)$$

Figure 2.13 depicts the "homogenization" scheme used to derive the macroscopic TSL of the cohesive crack. The traction is defined as the macroscopic Cauchy stress projected on the macroscopic crack plane, as given by Eq. (2.55) [75].

$$\mathbf{t}^M = \boldsymbol{\sigma}^M \cdot \mathbf{n}^M = \frac{1}{h^m} \mathbf{f}_B^m \quad (2.55)$$

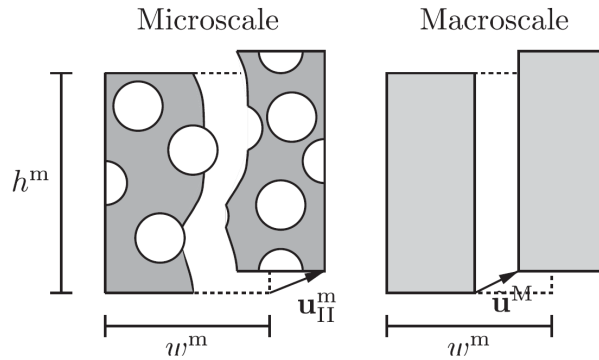


**Figure 2.13:** Schematic representation of homogenization of cohesive fracture [75]

The macroscopic crack opening  $\tilde{\mathbf{u}}^M$  can be equated to the displacement at the microscale using Eq. (2.56) [75].

$$\tilde{\mathbf{u}}^M = \mathbf{u}_{\text{II}}^m = \mathbf{a}_{\text{II}}^m \quad (2.56)$$

Turteltaub et al. [69] have proposed a new method for computational homogenization of fracture processes on a microscopic scale. The method uses a novel crack-based averaging technique. This thesis will make use of the homogenization scheme described in [69], which will be discussed in more detail in Chapter 3.

### 2.3.3 Representative Volume Element

Academic consensus over what sample size makes an element representative is far from being established, which might be best illustrated by the multitude of definitions for a RVE used in literature. Gitman et al. [29] summarized the following existing definitions of the RVE in their paper:

- The RVE is a sample that (a) is structurally entirely typical of the whole mixture on average, and (b) contains a sufficient number of inclusions for the apparent moduli to be effectively independent of the surface values of traction and displacement, as long as these values are macroscopically uniform [36].
- An RVE is the minimal material volume, which contains statistically enough mechanisms of deformation processes. The increasing of this volume should not lead to changes of evolution equations for field-values, describing these mechanisms [66].
- The RVE must be chosen sufficiently large compared to the microstructural size for the approach to be valid, and it is the smallest material volume element of the composite for which usual spatially constant overall modulus macroscopic constitutive representation is a sufficiently accurate model to represent the mean constitutive response [19].
- The RVE is a model of the material to be used to determine the corresponding effective properties for the homogenized macroscopic model. The RVE should be large enough to contain sufficient information about the microstructure in order to be representative, however it should be much smaller than the macroscopic body (Micro-Meso-Macro principle) [32].
- The RVE is defined as the minimum volume of laboratory scale specimen, such that the results obtained from this specimen can still be regarded as representative for a continuum [74].
- The size of the RVE should be large enough with respect to the individual grain size in order to define overall quantities such as stress and strain, but this size should also be small enough in order not to hide macroscopic heterogeneity [24].

The definitions above show a trade-off in size, where the RVE should simultaneously be much smaller than the macroscopic structure but still large enough to be constitutively valid, an idea known as the *separation of scales*. Ostoja-Starzewski [54] formulated a more elaborate definition of the RVE and how the size is determined:

- The RVE is very clearly defined in two situations only: (i) For a unit cell in a periodic microstructure, and (ii) For a volume containing a very large (mathematically infinite) set of microscale elements (e.g. grains, fibers), possessing statistically homogeneous and

erodic properties. In other words, in order to determine a RVE it is necessary to have (a) statistical homogeneity and ergodicity of the material; these two properties assure the RVE to be statistically representative of the macro response, and (b) some scale  $L$  of the material domain, sufficiently large relative to the microscale  $d$  (inclusion size) so as to ensure independence of boundary conditions [54].

Gitman et al. [29] propose the block scheme shown in Figure 2.14 as a suitable technique to determine the size of an existing RVE.

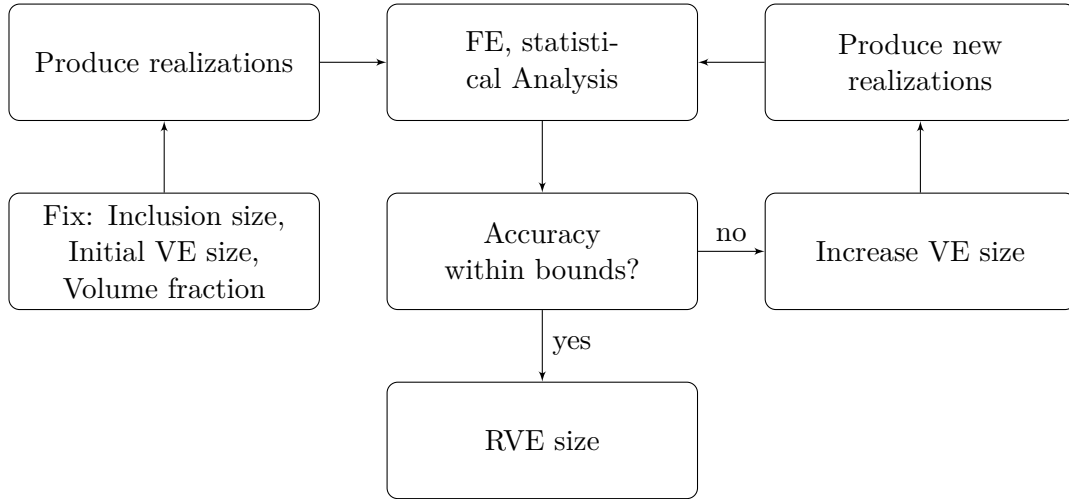


Figure 2.14: RVE size determination procedure [29]

### 2.3.4 Periodicity

The use of Periodic Boundary Conditions (PBC) was mentioned in Section 2.3.2. In this section, this type of boundary condition and its applicability will be explored. Periodicity in a material guarantees more-or-less identical stiffness on opposite sides.

The RVE is assumed to be part of a much larger sample (theoretically infinite) and the boundaries of the RVE are in reality, not boundaries. Displacement boundary conditions are used to impose deformations on the RVE, however the boundary conditions should also assimilate the presence of "surrounding material" and reduce the effects of the non-physical RVE-edges [13] as much as possible. Miehe [45] mentioned the following boundary conditions as those commonly applied for RVEs:

- Linear Displacement Boundary Conditions
- Periodic Boundary Conditions
- Minimal kinematical Boundary Conditions (equivalent to uniform traction)

Linear Displacement Boundary Conditions force the boundaries of the RVE to remain straight and are known to overestimate the stiffness (upper bound). Uniform traction appears in the lower bound for the stiffness, since it imposes macroscopic deformation in the weakest sense.

Periodic Boundary Conditions have been shown to provide a more accurate apparent stiffness for both periodic and random microstructures [14, 45].

PBCs are applied between the control (corner) nodes to arrive at an effective stress-strain relationship [14]. PBC kinematically ties material points located on opposite boundaries together. This requires a specific mesh construction where nodes on the borders identically repeat before (and after) the deformation is applied. This means that for a square  $l \times l$  RVE on the top and bottom, the  $x$ -coordinates of opposing nodes are identical and the  $y$ -coordinates differ by  $l$  and vice versa for the left and right borders. In Figure 2.15 the deformation of a square, to which periodic boundary conditions were applied, is pictured.

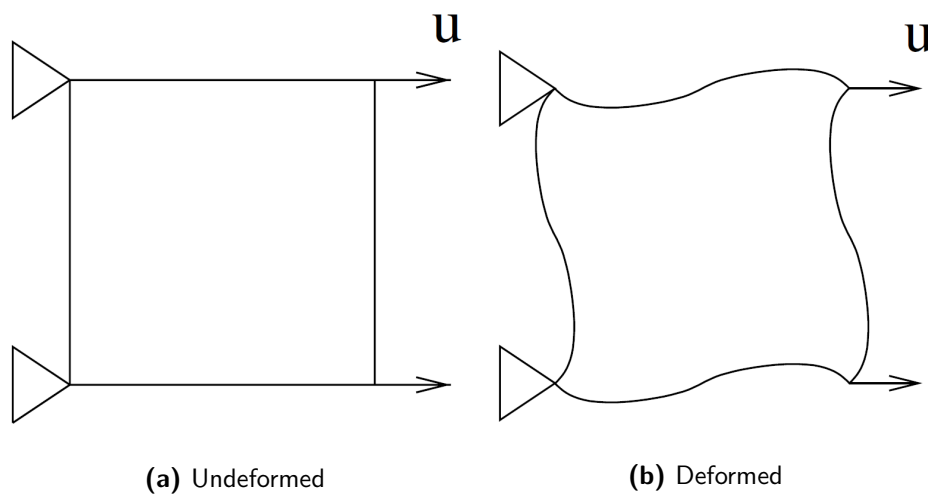


**Figure 2.15:** Periodic Boundary Conditions [29]

Periodic Boundary Conditions are applied in almost every multiscale method [2, 4, 29, 42, 43, 44, 75]. Anti-periodicity of the tractions was used in [52]. Coenen et al. [13] developed an alternative to PBCs referred to as percolation path aligned boundary conditions. For this type of boundary condition, nodes are still tied together, but now according to the direction of the (developing) strain localization bands instead of by a rectangular geometry-based coupling. In conclusion, in all consulted literature some sort of periodicity was applied.

Periodicity of boundary conditions normally requires *periodicity of material* to ensure equal stiffness and node locations on opposing sides. Gitman et al. [29] define periodicity of material as a material experiencing no *wall-effects*, where wall-effects are defined as the inability of inclusions to penetrate boundaries. They avoid wall-effects by allowing inclusions to penetrate through the borders, making them reappear on the opposite edge, as shown in Figure 2.16a. This same approach was taken in references [2, 4, 29, 52, 75].

Material periodicity for a RVE containing multiple inclusions is shown in Figure 2.16b. Inclusion penetrating the boundary reappear, but the rest of the inclusion distribution is random.

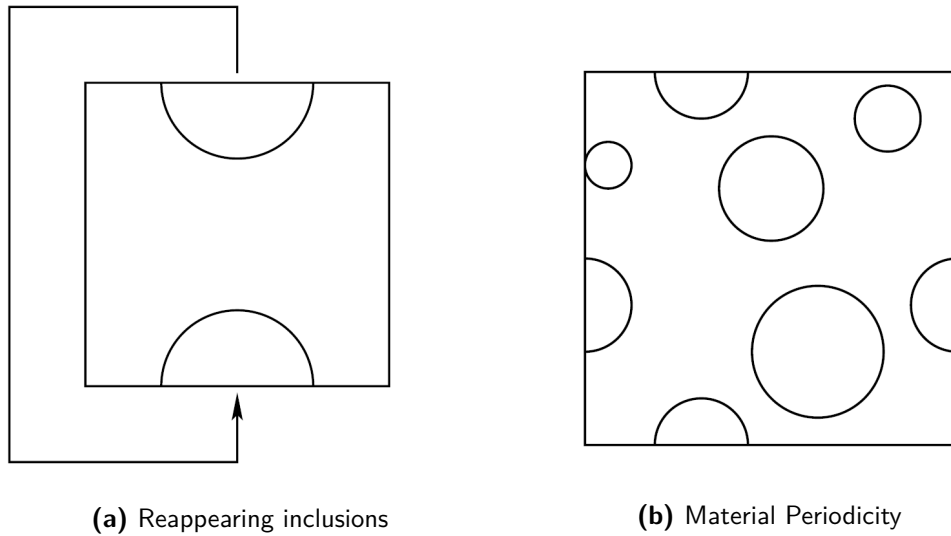


**Figure 2.16:** Avoiding wall effects by material periodicity [29]

## 2.4 Conclusion

In this chapter, the history of fracture mechanics analysis beginning from pre-1960s to modern day was discussed in detail. Original research was only applicable to linear elastic behavior whereas modern techniques allow for non-linear, multiscale analysis.

Beginning work led to the development of LEFM which applies to materials whose global behavior is linear elastic. With this method, there are three modes in which a crack can be loaded (independently or in combination), namely: opening, in-plane shear, and out-of-plane shear. In order to solve mixed mode problems, the SIF for each loading mode can be used to calculate the stress field ahead of a crack and then by tabulating the individual stresses, the overall stress may be calculated.

Evolving from LEFM, EPFM was developed for more broad, time-independent non-linear behavior in materials. EPFM differs from LEFM in the method of unloading. Although EPFM was more accurate for a wider range of analysis, the introduction of FRPs prompted a need for fracture mechanics which would take a large amount of different failure mechanisms (at once) into account, thus lamina failure theories were developed.

Further study of FRP failure led to development of CZMs, which lump softening mechanisms in front of a crack into a discrete line or plane. Through the use of CZMs, separation by a stress-displacement relationship can be modeled and the various types of damage are idealized as a loss in stiffness.

In conclusion, the legacy methods for analyzing and modeling fracture mechanics fell short in various regards, thus leading to the development of multiscale modeling using CZMs. This thesis will aim to employ multiscale modeling techniques through the use of CZMs with embedded intrinsic zero-thickness cohesive elements.

## Methodology

Chapter 3 describes the methodology and approach taken to develop a multiscale model. In Section 3.1, the multiscale implementation is discussed in detail, followed by information on the creation of the Microstructural Volume Element (MVE) in Section 3.2. Chapter 3 culminates in an explanation of the steps taken to produce effective properties by homogenization.

### 3.1 Multiscale Implementation

The multiscale method was discussed in Section 2.3. It was decided to use the eXtended Finite Element Method (XFEM) on the macroscale and Cohesive Element Modeling (CEM) on the microscale. For XFEM two distinct types of damage modeling are implemented in ABAQUS® [20]:

- Linear Elastic Fracture Mechanics (LEFM) approach (Classic XFEM)
- Cohesive Segment Approach (phantom-node method)

The cohesive segment approach or phantom-node method was conceptualized by Hansbo and Hansbo [31]. The method allows cracks to propagate through bulk elements, with the crack-opening governed by a cohesive law. Instead of adding extra degrees of freedom via enrichment, as is done in the classical XFEM, the phantom-node method duplicates homologous nodes to construct overlapping elements capable of representing the kinematics of a crack (see Figure 3.1).

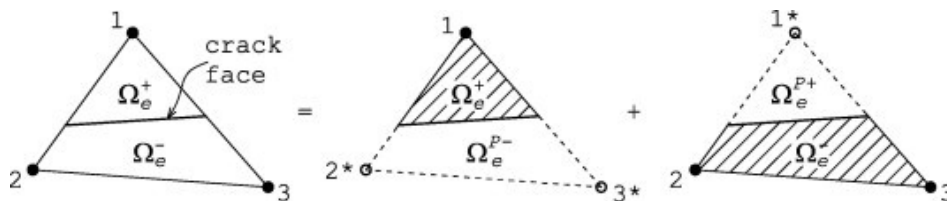


**Figure 3.1:** Phantom nodes and phantom domains for a cracked element [11]

The cohesive constitutive behavior on the macroscale can be obtained using the results of microscale simulations. For the microscale simulations, cohesive constitutive behavior, in the form of a bilinear Traction-Separation Law (TSL), will be defined for every constituent as an input. The results of the microscale simulations will describe an effective cohesive fracture process for the composite. This makes the cohesive segment approach ideal for the macroscopic portion of the multiscale analysis.

The microscale analysis is performed on a microstructural model with embedded zero-thickness cohesive elements. The cohesive elements are inserted at the element boundaries of continuum elements, corresponding to the intrinsic cohesive element modeling approach to fracture discussed in Section 2.2. The composite is a combination of two materials, i.e. fiber and matrix; however three different cohesive constitutive relationships are needed to describe fiber, matrix and interface behavior. While for all three a bilinear shaped (brittle fracture) TSL will be used, the values of the ultimate traction, fracture energy and critical opening will vary per phase.

A bilinear TSL has an initial (unphysical) linear hardening portion and a linear softening portion, as shown in Figure 3.2. The initial elastic opening ( $K$ ) is artificial and should mimic a rigid connection between the two bulk elements, corresponding to an uncracked solid. As was mentioned in Section 2.2.3, artificial compliance can occur when the initial elastic slope is not high enough.

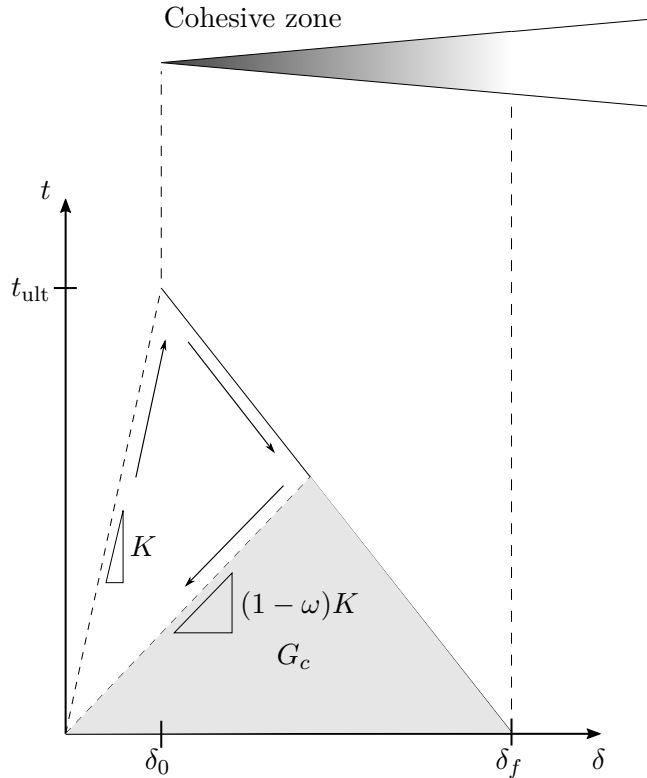


**Figure 3.2:** A bilinear traction-separation relation that describes the fracture behavior

The cohesive element will open elastically until the ultimate traction is reached. At this moment the cohesive element will have opened by  $\delta_0$ . Any opening beyond this separation

is damage. The damage process is represented by a linear softening relation. The cohesive element is failed once the traction ( $t$ ) reaches zero. The corresponding failure opening is denoted  $\delta_f$ .

The fracture energy ( $G$ ) required to complete the damage process is given by the area under the TSL. For an undamaged element the fracture energy is given by Eq. (3.1).

$$G = \frac{1}{2}\delta_f t_{\text{ult}} \quad (3.1)$$

If a cohesive element is unloaded before the damage process is completed it will follow a linear path back to the origin, with slope:

$$K' = (1 - \omega)K$$

Upon reloading the same slope is followed until the softening portion is reached. If not unloaded again, the softening slope is then followed until the damage process is completed. The remaining fracture energy at separation  $\delta$  is bound by the softening and the unloading slope as can be seen in Figure 3.2 and is given by Eq. (3.2).

$$G_c = \frac{1}{2}(1 - \omega)K\delta \delta_f \quad (3.2)$$

The parameter  $\omega$  is a measure of the stiffness degradation and is bound between 0 (undamaged) and 1 (fully damaged). The stiffness degradation factor can be used as a history parameter, although for high initial elastic slopes a fine very resolution might be required, as can be seen in Figure 3.3. Instead of using  $\omega$ , the history parameter  $\kappa$  is introduced, which stores the maximum separation that has occurred during damage process.

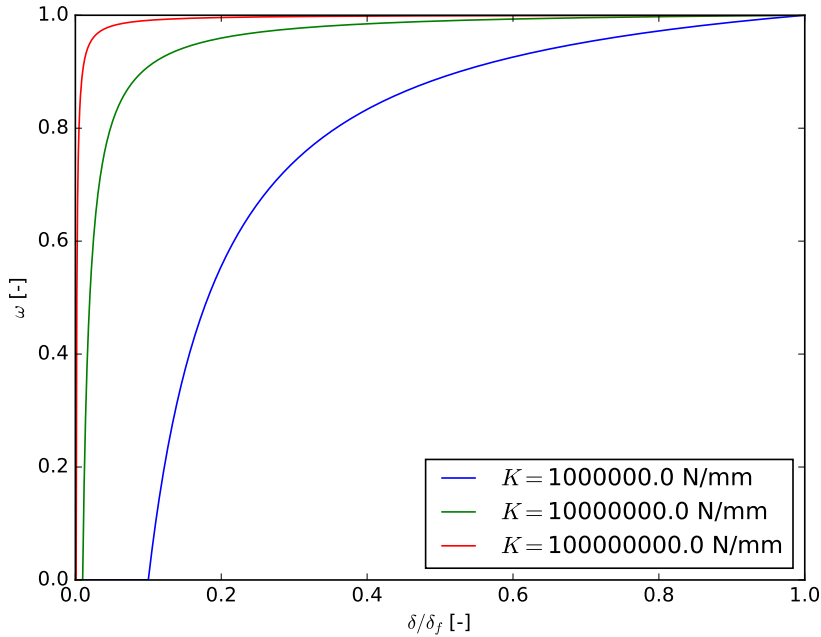


**Figure 3.3:** Stiffness degradation ( $t_{\text{ult}} = 100 \text{ N/mm}^2$ ,  $d_f = 0.001 \text{ mm}$ )

### 3.2 Modeling: The Microstructural Volume Element

The notion of a Representative Volume Element (RVE) was discussed in Section 2.3.3. In absence of a straightforward definition, regarding the size of a RVE, a size-convergence scheme was proposed by Gitman et al. [29] as a suitable method to determine the geometric properties of the RVE. In this thesis a model on the microscopic scale, that is not necessarily representative, will be referred to as a MVE. In other words, the RVE is a MVE for which increasing the size does not change the results.

The MVE should capture the microstructure of the composite material. In Figure 3.4 Scanning Electron Microscope (SEM) images of a Fiber Reinforced Plastic (FRP) plies are given. Although the fiber dimensions differ by approximately one order of magnitude, the Glass Fiber Reinforced Plastic (GFRP) and Carbon Fiber Reinforced Plastic (CFRP) microstructures are very similar; circular fibers distributed randomly. The carbon fiber reinforced epoxy (Figure 3.4b) appears more structured, but this can be attributed to the higher fiber volume fraction. In conclusion, the modeling technique should be able to produce MVEs containing randomly distributed circular fibers.

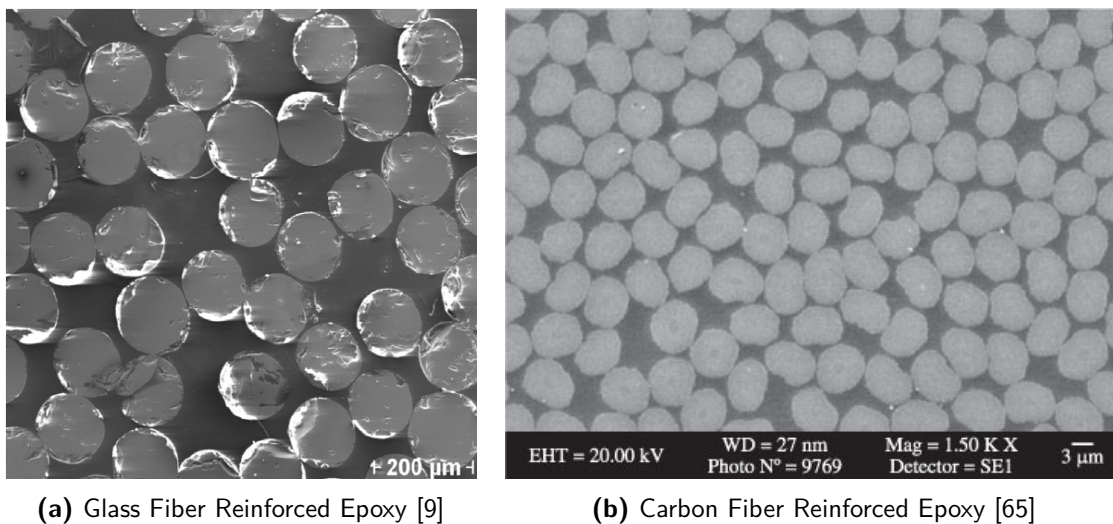


**Figure 3.4:** SEM micrograph of Fiber Reinforced Epoxy

As was discussed in Section 2.3.3, imposing Periodic Boundary Conditions (PBC) on the boundaries of the MVE results in the most accurate apparent stiffness compared to other types of boundary conditions. Moreover the PBC are sufficient to satisfy the global Hill-Mandel condition, i.e. conservation of energy for the bulk and crack combined, as was discussed in Section 2.3.2.

In a Finite Element Method (FEM) the application of PBC can be done by tying nodes on opposing edges, meaning that the displacement of opposing nodes is coupled via a constraint. This coupling requires equal node locations on either side of the MVE. Material periodicity ensures equal stiffness at opposing edges and is achieved by letting inclusions, that penetrate boundaries, reappear on the other side. In Figure 3.5 a periodic MVE is shown.

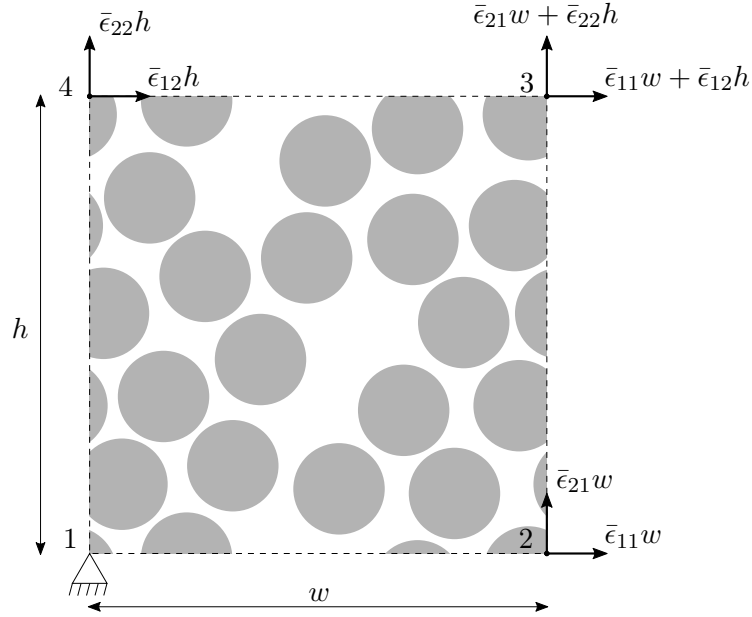


**Figure 3.5:** Microstructural Volume Element

The load application is done via control nodes in the four corners of the MVE. Instead of forces, the MVE is loaded via prescribed displacements, since in the multiscale method the displacement and displacement increment are inputs for the microscale analysis (see: Section 2.3.2). Moreover the softening occurring during the fracture process makes a displacement controlled method preferable over load controlled.

A strain tensor  $\bar{\epsilon}$  acting on a  $w \times h$  MVE can be translated to applied displacements with respect to an arbitrary position. The choice was made to pick the lower left corner, which will be referred to as corner 1, as the static node, meaning that all degrees of freedom will be constrained for this node. The position vectors of the remaining corners with respect to corner 1 are given below:

$$\mathbf{x}_2 - \mathbf{x}_1 = \begin{bmatrix} w \\ 0 \end{bmatrix} \quad \mathbf{x}_3 - \mathbf{x}_1 = \begin{bmatrix} w \\ h \end{bmatrix} \quad \mathbf{x}_4 - \mathbf{x}_1 = \begin{bmatrix} 0 \\ h \end{bmatrix}$$

With corner 1 fixed, the applied displacement to corner 2 as a result of  $\bar{\epsilon}$  can be computed to be:

$$\begin{bmatrix} \bar{\epsilon}_{11} & \bar{\epsilon}_{12} \\ \bar{\epsilon}_{21} & \bar{\epsilon}_{22} \end{bmatrix} \begin{bmatrix} w \\ 0 \end{bmatrix} = \begin{bmatrix} \bar{\epsilon}_{11} w \\ \bar{\epsilon}_{21} w \end{bmatrix}$$

The applied displacement vectors of the other two corners can be computed similarly. The boundary conditions applied to all corners are included in Figure 3.5.

### 3.3 Homogenization

In a multiscale framework the homogenization process is the coupling between the length scales. The information of the microscale is condensed to macroscopic constitutive behavior.

Homogenization techniques include elementary procedures such as Rule of Mixtures (RoM), analytical or numerical unit cell methods and computational homogenization on RVEs as was discussed in Section 2.3.2. This section will discuss two computational homogenization schemes; First a bulk homogenization process to obtain the effective Coefficient of Thermal Expansion (CTE) of the composite is discussed in Section 3.3.1. Subsequently, in Section 3.3.2, the fracture homogenization process used in this project is included. Lastly, the decomposition technique into mode-dependent fracture properties to be used at the macroscopic scale is explained in Section 3.3.3.

### 3.3.1 Bulk Homogenization

The bulk homogenization process refers to homogenization done prior to the onset fracture. The process uses the volume averaged stress and strain tensors and can be used to determine bulk constitutive behavior such as the effective longitudinal and shear stiffness. The volume-averaged stress is given by Eq. (3.3)

$$\langle \boldsymbol{\sigma} \rangle_{\Omega} = \frac{1}{|\Omega|} \int_{\Omega} \boldsymbol{\sigma} \, dv \quad (3.3)$$

And the volume averaged strain is given by Eq. (3.4).

$$\langle \boldsymbol{\epsilon} \rangle_{\Omega} = \frac{1}{|\Omega|} \int_{\Omega} \boldsymbol{\epsilon} \, dv \quad (3.4)$$

The volume averaged stress and strain are related through the effective stiffness tensor as given by Eq. (3.5). The components of the effective stiffness tensor ( $\mathbb{C}$ ) can be obtained using the results of multiple load cases.

$$\langle \boldsymbol{\sigma} \rangle_{\Omega} = \mathbb{C} \langle \boldsymbol{\epsilon} \rangle_{\Omega} \quad (3.5)$$

For a full multiscale implementation of a composite model, the pre-fracture constitutive behavior would be obtained in this manner. For the purpose of this thesis, the computation of the effective stiffness tensor is left out of the scope. Bulk homogenization is, however, used to compute the effective CTE of the composite.

By applying a thermal load to the RVE and using boundary conditions corresponding to free contraction, the effective thermal strain is obtained as a function of applied temperature. The effective CTE of the composite is then obtained as the gradient of the thermal strain evolution. The CTE in 1-direction is given by Eq. (3.6).

$$\alpha_{11} = \frac{d\langle \epsilon_{11} \rangle_{\Omega}}{dT} \quad (3.6)$$

And, similarly, the CTE in 2-direction is evaluated computed using Eq. (3.7).

$$\alpha_{22} = \frac{d\langle \epsilon_{22} \rangle_{\Omega}}{dT} \quad (3.7)$$

FRPs are transversely isotropic. The transverse isotropy extends to the thermal behavior and the CTE in any direction inside the transverse plane is equal:

$$\alpha_{11} \approx \alpha_{22}$$

The MVE should therefore show transversely isotropic thermal expansion to be considered constitutively valid and representative of macroscopic composite behavior..

### 3.3.2 Effective Fracture Properties

The effective fracture properties that can be used on the macroscopic scale are obtained by homogenization. Turteltaub et al. [69] have proposed a new method of homogenizing the microscopic fracture process. The motive for developing this method was to overcome issues caused by periodic cracks, that can form as a result of the periodic boundary conditions.

The microscale Boundary Value Problem (BVP) of a quasi-static fracture process is given by Eq. (3.8) [69].

$$\operatorname{div} \boldsymbol{\sigma}(\mathbf{x}, t) = \mathbf{0} \quad \mathbf{x} \text{ in } \Omega \setminus \Gamma \quad (3.8a)$$

$$\mathbf{t}^+(\mathbf{x}^+, t) = -\mathbf{t}^-(\mathbf{x}^-, t) \quad \mathbf{x} \text{ on } \Gamma \quad (3.8b)$$

$$\begin{aligned} \mathbf{u}(\mathbf{x} + w\mathbf{e}_1, t) - \mathbf{u}(\mathbf{x}, t) &= w\bar{\boldsymbol{\epsilon}}(t)\mathbf{e}_1 \\ \mathbf{t}(\mathbf{x} + w\mathbf{e}_1, t) &= -\mathbf{t}(\mathbf{x}, t) \end{aligned} \quad \mathbf{x} \text{ on } \partial\Omega_3 \setminus \Gamma \quad (3.8c)$$

$$\begin{aligned} \mathbf{u}(\mathbf{x} + h\mathbf{e}_2, t) - \mathbf{u}(\mathbf{x}, t) &= h\bar{\boldsymbol{\epsilon}}(t)\mathbf{e}_2 \\ \mathbf{t}(\mathbf{x} + h\mathbf{e}_2, t) &= -\mathbf{t}(\mathbf{x}, t) \end{aligned} \quad \mathbf{x} \text{ on } \partial\Omega_4 \setminus \Gamma \quad (3.8d)$$

$$\begin{aligned} \mathbf{u}^\pm(\mathbf{x}^\pm + w\mathbf{e}_1, t) - \mathbf{u}^\pm(\mathbf{x}^\pm, t) &= w\bar{\boldsymbol{\epsilon}}(t)\mathbf{e}_1 \\ \mathbf{t}^\pm(\mathbf{x}^\pm + w\mathbf{e}_1, t) &= -\mathbf{t}^\pm(\mathbf{x}^\pm, t) \end{aligned} \quad \mathbf{x} \text{ on } \partial\Omega_3 \cap \Gamma \quad (3.8e)$$

$$\begin{aligned} \mathbf{u}^\pm(\mathbf{x}^\pm + h\mathbf{e}_2, t) - \mathbf{u}^\pm(\mathbf{x}^\pm, t) &= h\bar{\boldsymbol{\epsilon}}(t)\mathbf{e}_2 \\ \mathbf{t}^\pm(\mathbf{x}^\pm + h\mathbf{e}_2, t) &= -\mathbf{t}^\pm(\mathbf{x}^\pm, t) \end{aligned} \quad \mathbf{x} \text{ on } \partial\Omega_4 \cap \Gamma \quad (3.8f)$$

In the absence of body forces, the local balance of linear momentum is given by Eq. (3.8a). The traction-continuity on the crack surface is given by Eq. (3.8b). The periodic boundary conditions are given by Eq. (3.8c)-(3.8f). For completion the relation between the strain and displacement fields is given below.

$$\boldsymbol{\epsilon} = \frac{1}{2} (\nabla \mathbf{u} + \nabla \mathbf{u}^T) \quad \mathbf{x} \in \Omega \setminus \Gamma \quad (3.9)$$

Note that Eq. (3.9) is only valid for material points  $\mathbf{x}$  that are not on the crack. The relation between the applied strain  $\bar{\boldsymbol{\epsilon}}$ , the average strain  $\langle \boldsymbol{\epsilon} \rangle_\Omega$  in the bulk material and the fracture strain  $\boldsymbol{\epsilon}^f$  is given by Eq. (3.10) [69].

$$\bar{\boldsymbol{\epsilon}} = \langle \boldsymbol{\epsilon} \rangle_\Omega + \boldsymbol{\epsilon}^f \quad (3.10)$$

where the notation  $\langle \cdot \rangle_\Omega = (1/|\Omega|) \int_\Omega (\cdot) dv$ , representing volume averaged quantities, is introduced for convenience. The fracture strain is defined by Eq. (3.11).

$$\boldsymbol{\epsilon}^f := \frac{1}{|\Omega|} \int_\Gamma [[\mathbf{u}]] \otimes \mathbf{m}]_{\text{sym}} ds \quad (3.11)$$

Rather than satisfying the Hill-Mandel energy condition *a priori*, e.g. through boundary conditions as discussed in Section 2.3.2, Turteltaub et al. [69] chose to approximately enforce the macrohomogeneity condition *a posteriori* through the definition of the effective macroscopic quantities. The macrohomogeneity condition for the crack is given by Eq. (3.12) [69].

$$\left\langle (\langle \boldsymbol{\sigma} \rangle_\Omega - \boldsymbol{\sigma}) \cdot [[\dot{\mathbf{u}}]] \otimes \mathbf{m}]_{\text{sym}} \right\rangle_\Gamma = 0 \quad (3.12)$$

The crack average on  $\Gamma$  contains all crack segments, i.e. including bifurcations and isolated parts. The relation given by Eq. (3.12) states that the volume-averaged stress acting on the local crack normal  $\mathbf{m}$  and working on the crack opening rate  $[[\dot{\mathbf{u}}]]$  has to, on average, equal the work done by the local crack surface traction  $\mathbf{t} = \boldsymbol{\sigma} \mathbf{m}$  [69].

Equation (3.13) gives the relation between the macroscopic crack normal  $\mathbf{m}^f$ , macroscopic crack length  $\Gamma^f$  and macroscopic crack opening rate  $[[\dot{\mathbf{u}}]]^f$ , and their microscopic counterparts.

$$|\Gamma^f| [[\dot{\mathbf{u}}]]^f \otimes \mathbf{m}^f \approx |\Gamma| \langle [[\dot{\mathbf{u}}]] \otimes \mathbf{m} \rangle_\Gamma \quad (3.13)$$

where the notation  $\langle \cdot \rangle_\Gamma = (1/|\Gamma|) \int_\Gamma (\cdot) ds$ , representing crack averaged quantities, is introduced for convenience. The equation is approximate as the tensor  $\langle [[\dot{\mathbf{u}}]] \otimes \mathbf{m} \rangle_\Gamma$ , on the right hand side of Eq. (3.13), is generally not rank-one, as opposed to the macroscopic kinematical description of the crack.

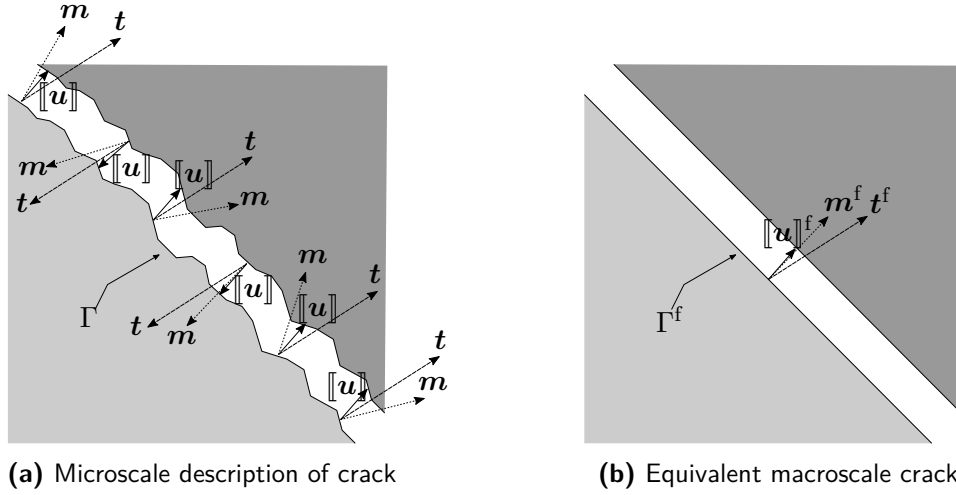


**Figure 3.6:** Hill-Mandel requirement for an equivalent crack. The figure also illustrates the complication caused by the arbitrary orientation of the cohesive elements.

The micro- and macroscale kinetics of the crack are shown in Figure 3.6. A relation between the openings is either scale has already been established, be it in rate form, in Eq. (3.13). Equation (3.14) defines the crack averaged macroscopic traction ( $\mathbf{t}_\Gamma^f$ ).

$$|\Gamma^f| \mathbf{t}_\Gamma^f \otimes \mathbf{m}^f := |\Gamma| \langle \mathbf{t} \otimes \mathbf{m} \rangle_\Gamma \quad (3.14)$$

The right side of Eq. (3.14) represents the integral of the *cohesive stress* over the crack surface. Although it is only defined using a single plane, it can be seen as a stress by recognizing that the local crack normal coincides with the cohesive element normal. By integrating the cohesive stress instead of directly integrating the traction, the practical issues caused by the arbitrary definition of the element normals is overcome.

The equivalent macroscopic crack length  $\Gamma^f$  can be computed using the MVE geometry and the effective normal. Recognizing that the periodic boundaries will force cracks to reappear on either side, Eq. (3.15) was formulated. In this equation the length  $\Gamma_0$  is the longest straight

line with normal  $\mathbf{m}^f$  passing once through the MVE domain. The length  $\Gamma_0$  is computed using Eq. (3.16).

$$|\Gamma^f| = \begin{cases} |\Gamma_0| & \text{if } r > r_{\max} \\ r|\Gamma_0| & \text{otherwise} \end{cases} \quad (3.15)$$

$$|\Gamma_0| = \min \left( \frac{w}{|\mathbf{n}_2 \cdot \mathbf{m}^f|}, \frac{h}{|\mathbf{n}_1 \cdot \mathbf{m}^f|} \right) \quad (3.16)$$

The factor  $r$  gives the number of times a straight crack of length  $\Gamma_0$  and normal  $\mathbf{m}^f$  can pass through the domain, starting from one corner and reappearing periodically as shown in Figure 3.7.

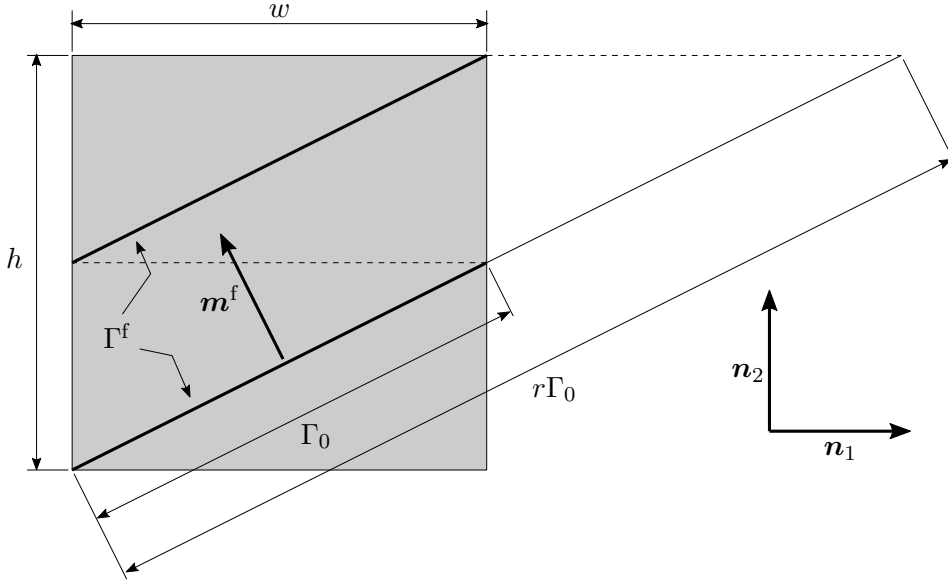


**Figure 3.7:** Macroscopic crack length

For a perfectly horizontal or vertical crack the factor  $r \rightarrow \infty$ . In Eq. (3.15) this is handled by specifying a condition for the maximum value of  $r$ . When  $r$  is above this maximum value ( $r_{\max}$ ) the crack is assumed to be approximately vertical or horizontal with length  $\Gamma_0$ . The factor  $r$  can be computed using Eq. (3.17).

$$r = \frac{1}{|\Gamma_0|} \max \left( \frac{w}{|\mathbf{n}_2 \cdot \mathbf{m}^f|}, \frac{h}{|\mathbf{n}_1 \cdot \mathbf{m}^f|} \right) \quad (3.17)$$

The Hill-Mandel condition for the crack is given by Eq. (3.18) [69].

$$|\Gamma^f| \mathbf{t}^f \cdot \llbracket \dot{\mathbf{u}} \rrbracket^f \approx |\Gamma| \langle \mathbf{t} \cdot \llbracket \dot{\mathbf{u}} \rrbracket \rangle_{\Gamma} \quad (3.18a)$$

$$|\Gamma^f| \mathbf{t}^f \cdot \llbracket \dot{\mathbf{u}} \rrbracket^f \approx |\Gamma| \langle \langle \boldsymbol{\sigma} \rangle_{\Omega} \mathbf{m} \cdot \llbracket \dot{\mathbf{u}} \rrbracket \rangle = \langle \boldsymbol{\sigma} \rangle_{\Omega} \cdot |\Gamma| \langle \llbracket \dot{\mathbf{u}} \rrbracket \otimes \mathbf{m} \rangle_{\text{sym}} \quad (3.18b)$$

The power-requirements formulated in Eq. (3.18) motivated the definition of  $\mathbf{t}^f$  given by Eq. (3.19) [69].

$$\mathbf{t}^f = \alpha \mathbf{t}_\Gamma^f + (1 - \alpha) \mathbf{t}_\Omega^f \quad (3.19)$$

Where  $\mathbf{t}_\Omega^f$  is the volume-averaged stress acting on the crack surface as given by Eq. (3.20).

$$\mathbf{t}_\Omega^f = \langle \boldsymbol{\sigma} \rangle_\Omega \mathbf{m}^f \quad (3.20)$$

The Hill-Mandel conditions for the crack is approximately enforced by selecting an appropriate value for  $\alpha$ . The Hill-Mandel condition given by Eq. (3.18a) can be combined with Eq. (3.19) to arrive at:

$$\alpha |\Gamma^f| \mathbf{t}_\Gamma^f \cdot \llbracket \dot{\mathbf{u}} \rrbracket^f + (1 - \alpha) |\Gamma^f| \mathbf{t}_\Omega^f \cdot \llbracket \dot{\mathbf{u}} \rrbracket^f \approx |\Gamma| \langle \mathbf{t} \cdot \llbracket \dot{\mathbf{u}} \rrbracket \rangle_\Gamma$$

Which is equal to:

$$\alpha |\Gamma^f| \mathbf{t}_\Gamma^f \cdot \llbracket \dot{\mathbf{u}} \rrbracket^f + (1 - \alpha) |\Gamma^f| \mathbf{t}_\Omega^f \cdot \llbracket \dot{\mathbf{u}} \rrbracket^f \approx \int_\Gamma \mathbf{t} \cdot \llbracket \dot{\mathbf{u}} \rrbracket d\Gamma$$

Both sides are subsequently divided by the volume to obtain volume-averaged powers:

$$\alpha \frac{1}{\Omega} |\Gamma^f| \mathbf{t}_\Gamma^f \cdot \llbracket \dot{\mathbf{u}} \rrbracket^f + (1 - \alpha) \frac{1}{\Omega} |\Gamma^f| \mathbf{t}_\Omega^f \cdot \llbracket \dot{\mathbf{u}} \rrbracket^f \approx \frac{1}{\Omega} \int_\Gamma \mathbf{t} \cdot \llbracket \dot{\mathbf{u}} \rrbracket d\Gamma$$

Which can be rewritten to:

$$\alpha P_\Gamma^f + (1 - \alpha) P_\Omega^f \approx P^f \quad (3.21)$$

Where the three volume average crack power terms are given by Eq. (3.22).

$$P_\Gamma^f = \frac{1}{\Omega} |\Gamma^f| \mathbf{t}_\Gamma^f \cdot \llbracket \dot{\mathbf{u}} \rrbracket^f \quad (3.22a)$$

$$P_\Omega^f = \frac{1}{\Omega} |\Gamma^f| \mathbf{t}_\Omega^f \cdot \llbracket \dot{\mathbf{u}} \rrbracket^f \quad (3.22b)$$

$$P^f = \frac{1}{\Omega} \int_\Gamma \mathbf{t} \cdot \llbracket \dot{\mathbf{u}} \rrbracket d\Gamma \quad (3.22c)$$

Similarly, instead of a rate form, a work version of Eq. (3.21) can be formulated.

$$\alpha W_\Gamma^f + (1 - \alpha) W_\Omega^f = W^f \quad (3.23)$$

Where the three volume average crack work terms are given by Eq. (3.24).

$$W_\Gamma^f = \frac{1}{\Omega} |\Gamma^f| \mathbf{t}_\Gamma^f \cdot \llbracket \mathbf{u} \rrbracket^f \quad (3.24a)$$

$$W_\Omega^f = \frac{1}{\Omega} |\Gamma^f| \mathbf{t}_\Omega^f \cdot \llbracket \mathbf{u} \rrbracket^f \quad (3.24b)$$

$$W^f = \frac{1}{\Omega} \int_\Gamma \mathbf{t} \cdot \llbracket \mathbf{u} \rrbracket d\Gamma \quad (3.24c)$$

The macroscopic crack opening  $\llbracket \mathbf{u} \rrbracket^f$  is defined by Eq. (3.25), which is similar to the rate form given by Eq. (3.13).

$$|\Gamma^f| \llbracket \mathbf{u} \rrbracket^f \otimes \mathbf{m}^f \approx |\Gamma| \langle \llbracket \mathbf{u} \rrbracket \otimes \mathbf{m} \rangle_\Gamma \quad (3.25)$$

The exact value of  $\alpha$  needs to be determined by inspection and may vary per MVE size or load case. With  $\alpha$  known, the macroscopic traction vector can be determined and related to the macroscopic crack opening. The resulting relation is the homogenized traction-separation relation, also known as the Effective Traction Separation Law (ETSL), which is the result of interest:

$$\mathbf{t}^f = \mathbf{t}^f(\llbracket \mathbf{u} \rrbracket^f)$$

All the ingredients for the complete cohesive fracture homogenization process have been described above. The sequential steps of the cohesive fracture homogenization process are as follows; First the fully-failed state, corresponding to the last frame in the simulation, is used to compute the geometrical characteristics of the macroscopic crack, followed by the time-incremental post-processing of the results of interest. Lastly the Hill-Mandel condition is approximated resulting in the weighting parameter  $\alpha$  and the ETSL. The algorithm is as follows:

1. Macroscopic crack normal  $\mathbf{m}^f$  and nominal crack length  $|\Gamma^f|$ :
  - 1.1 Determine the set of failed (cohesive) elements that form the crack surface  $\Gamma$  and compute the tensor  $\langle \llbracket \mathbf{u} \rrbracket \otimes \mathbf{m} \rangle_\Gamma$  at  $t = t_F$  (fully-failed state); typically the last state in an incrementally loaded simulation.
  - 1.2 Compute the vector  $|\Gamma^f| \llbracket \mathbf{u} \rrbracket^f$  and equivalent crack normal  $\mathbf{m}^f$  using the Eckart-Young theorem, with the requirement that  $|\mathbf{m}^f| = 1$ . Singular Value Decomposition (SVD) of the right side of Eq. (3.25)
$$|\Gamma^f| \llbracket \mathbf{u} \rrbracket^f \otimes \mathbf{m}^f \approx |\Gamma| \langle \llbracket \mathbf{u} \rrbracket \otimes \mathbf{m} \rangle_\Gamma \quad \text{at } t = t_F$$

results in  $\mathbf{m}^f$  and the product  $|\Gamma^f| \llbracket \mathbf{u} \rrbracket^f$ . At this point  $|\Gamma^f|$  and  $\llbracket \mathbf{u} \rrbracket^f$  are not known individually.
  - 1.3 Use  $\mathbf{m}^f$  and the MVE dimensions to compute  $|\Gamma^f|$  from Eq. (3.15).
  - 1.4 Use  $|\Gamma^f|$  and the product  $|\Gamma^f| \llbracket \mathbf{u} \rrbracket^f$  to compute the effective macroscopic crack opening  $\llbracket \mathbf{u} \rrbracket^f$ .

2. Time-incremental post-processing at time step  $t_n$ :

- 2.1 Compute volume averaged stress  $\langle \boldsymbol{\sigma}_n \rangle_\Omega$ .
- 2.2 Use the Eckart-Young theorem to compute the effective macroscopic crack opening vector  $\llbracket \mathbf{u} \rrbracket_n^f$  at time  $t_n$  as

$$|\Gamma^f| \llbracket \mathbf{u} \rrbracket_n^f \otimes \mathbf{m}^f \approx |\Gamma| \langle \llbracket \mathbf{u} \rrbracket_n \otimes \mathbf{m} \rangle_\Gamma \quad \text{at } t = t_n$$

with  $\mathbf{m}^f$ ,  $|\Gamma|$  and  $|\Gamma^f|$  computed for  $t = t_F$ .

- 2.3 Compute the effective traction acting on the crack surface  $(\mathbf{t}_n)_\Gamma^f$  at time  $t = t_n$  using Eq. (3.14):

$$|\Gamma^f| (\mathbf{t}_n)_\Gamma^f \otimes \mathbf{m}^f = |\Gamma| \langle \mathbf{t}_n \otimes \mathbf{m} \rangle_\Gamma \quad \text{at } t = t_n$$

3. Approximate the Hill-Mandel Condition

- 3.1 Determine the  $\alpha$  weighting factor as the best fit for the crack-based Hill-Mandel condition on the rate of work (power).
- 3.2 Compute the effective macroscopic traction at time  $t = t_n$  as a weighed average of the crack-averaged and volume averaged traction acting on the crack surface using Eq. (3.19):

$$\mathbf{t}_n^f = \alpha(\mathbf{t}_n)_\Gamma^f + (1 - \alpha)\langle\boldsymbol{\sigma}_n\rangle_\Omega \mathbf{m}^f \quad \text{at } t = t_n$$

### 3.3.3 Mode mixity

The effective macroscopic traction vector and the effective macroscopic opening vector were determined using the approach described in Section 3.3.2. The simulations at the macroscopic scale use the cohesive segment approach, as was discussed in Section 3.1. The crack-opening at the macroscopic scale is governed by a mode-dependent cohesive law. The final step in implementing the multiscale is therefore the decomposition of the effective vectors in modal components. To this end the mode-mixity parameter ( $\beta$ ) is introduced. The mode-mixity is defined as the opening angle as given by Eq. (3.26).

$$\beta = \tan^{-1} \left( \frac{\delta_{II}^f}{\delta_I^f} \right) \quad (3.26)$$

The definition of the mode I and mode II opening is illustrated in Figure 3.8.

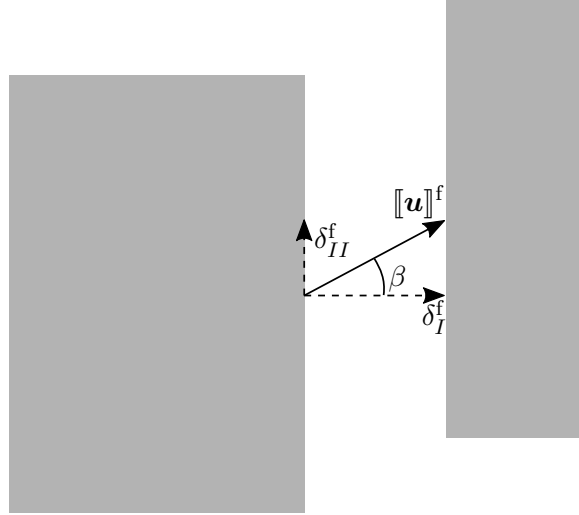


**Figure 3.8:** Mode mixity parameter  $\beta$

The effective macroscopic opening vector is decomposed using the dot product with the macroscopic crack normal, as given by Eq. (3.27).

$$\delta_I^f = \llbracket \mathbf{u} \rrbracket^f \cdot \mathbf{m}^f \quad (3.27a)$$

$$\delta_{II}^f = \left| \llbracket \mathbf{u} \rrbracket^f - \delta_I^f \mathbf{m}^f \right| \quad (3.27b)$$

The effective macroscopic traction vector is decomposed using the same approach, as given by Eq. (3.28).

$$t_I^f = \mathbf{t}^f \cdot \mathbf{m}^f \quad (3.28a)$$

$$t_{II}^f = \left| \mathbf{t}^f - t_I^f \mathbf{m}^f \right| \quad (3.28b)$$

As a result of the modal decomposition two scalar traction-separation laws are obtained (see Eq. (3.29)). These ETSLs define the mode-dependent macroscopic cohesive laws.

$$t_I^f = t_I^f(\delta_I^f) \quad (3.29a)$$

$$t_{II}^f = t_{II}^f(\delta_{II}^f) \quad (3.29b)$$



## Numerical Experimental Setup

Chapter 4 communicates the numerical experimental setup. First, in Section 4.1, the background behind the model generation is discussed, including the definition of input variables, geometry, mesh, boundary conditions, and the generation of the Abaqus input file. Section 4.2 covers the settings that influence the analysis and convergence of the Abaqus solver. Chapter 4 concludes with Section 4.3, which illuminates the postprocessing methods, including data extraction, processing, and multiscale coupling.

### 4.1 Preprocessing: Model generation

During the preprocessing a Finite Element (FE) model is generated from the input variables. The preprocessing occurs entirely in `python` scrips, with the exception of the bulk mesh generation. The latter is done using `gmsh`, a finite element mesh generator with built-in pre- and postprocessing facilities distributed under the terms of the GNU General Public License. The preprocessing framework is shown schematically in Figure 4.1.

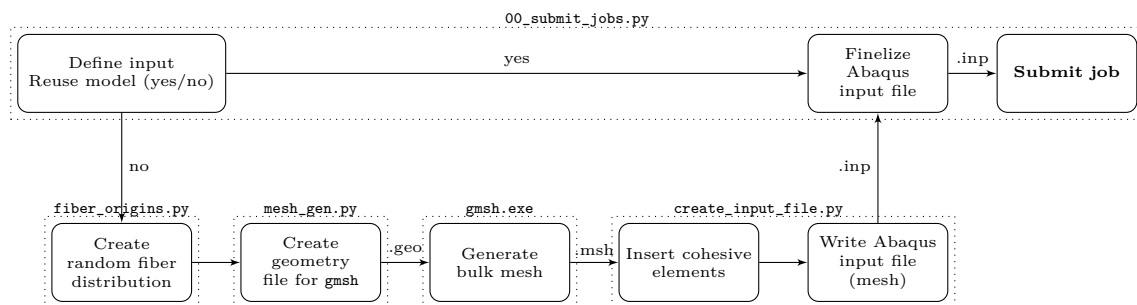


**Figure 4.1:** Schematic representation of the preprocessing computational framework

In reality only is single `python` script (`00_submit_jobs.py`) is executed and all other `python` files contain functions that are imported at the start of this script. The final result of the

preprocessing is an ABAQUS<sup>®</sup> input file (.inp). The input file is uploaded to the computational cluster<sup>1</sup> of Delft University of Technology (TU Delft) and executed with ABAQUS<sup>®</sup>.

Each of the steps will be addressed in more detail in the remainder of this section, starting with a discussion of the input variables in Section 4.1.1. Thereafter, in Section 4.1.2, the periodic geometry definition of the Microstructural Volume Element (MVE) and the method for finding random fiber distributions is explained. The mesh generation approach using a combination of `gms` and `python` is included in Section 4.1.3, followed by the computational formulation of the boundary conditions in Section 4.1.4. The section is concluded with the ABAQUS<sup>®</sup> input file generation.

### 4.1.1 Input variables

The input specification is done at the start of the computational framework. The geometry of the MVE is specified by four dimensions and a (target) fiber volume fraction (see: Table 4.1). For a unit cell generation, the volume fraction is unused and a single fiber (with semi-axes dimensions  $a$ ,  $b$ ) is placed at the center of the  $w \times h$  mm MVE.

Variable	Description	Symbol	Units
<code>w</code>	Width	$w$	mm
<code>h</code>	Height	$h$	mm
<code>a</code>	Semi-axis ( $x$ )	$a$	mm
<code>b</code>	Semi-axis ( $y$ )	$b$	mm
<code>V_f</code>	Fiber volume fraction	$V_f$	[-]

**Table 4.1:** Input parameters: Geometry

In-line with the project objective, the framework requires an initial and operating temperature to be specified. The simulation will include a temperature step, in which the temperature can be increased or reduced to the operating temperature, which will be discussed in more detail in Section 4.1.4. Besides the thermal loading, the applied strain is specified as an input. The applied strain will be used to compute the prescribed displacements for the corners of the MVE (see: Section 4.1.4). Table 4.2 lists the input parameters that stipulate the loading of the MVE with the corresponding symbol and units.

Variable	Description	Symbol	Units
<code>T_0</code>	Initial Temperature <sup>2</sup>	$T_0$	K
<code>T_1</code>	Operating Temperature	$T_1$	K
<code>load_cases</code>	Applied strain	$\bar{\epsilon}$	[-]

**Table 4.2:** Input parameters: Loading

The thermal/mechanical nature of the problem requires the specification of quite a lot of material properties of the fiber and matrix. The density ( $\rho$ ) and elastic properties ( $E$  and  $\nu$ )

<sup>1</sup>[hpc12.tudelft.net](http://hpc12.tudelft.net)

<sup>2</sup>The initial temperature is also the residual stress-free temperature of the composite

along with the coefficient of thermal expansion ( $\alpha$ ), the specific heat ( $C_p$ ) and the thermal conductivity ( $\kappa$ ) need to be specified for both the fiber and the matrix. Moreover the fracture properties, in the form of an ultimate strength value and either the fracture toughness or failure opening, is required input for the fiber, the matrix as well as the fiber-matrix interface.

Some of the material properties may vary with temperature. During the literature study [78] it became apparent that while the fiber properties can be assumed temperature-independent, the matrix stiffness, strength, toughness and expansion coefficient are definitely not. The computational framework allows these properties to be specified as a linear function of temperature, which is in-line with temperature-dependent material behavior obtained for epoxy from physical experiments. A list of the material input is included in Table 4.3.

Variable	Description	Symbol	Units
p_F	Fiber Density	$\rho_F$	kg/mm <sup>3</sup>
E_Ft	Fiber Transverse Elastic Modulus	$E_{F,t}$	MPa
nu_F	Fiber Poisson's ratio	$\nu_F$	[-]
a_Ft	Fiber Transverse Coefficient of Thermal Expansion	$\alpha_{F,t}$	K <sup>-1</sup>
Cp_F	Fiber Specific Heat	$C_{pF}$	mJ/(kg K)
k_F	Fiber Thermal Conductivity	$\kappa_F$	mW/(mm K)
p_M	Matrix Density	$\rho_M$	kg/mm <sup>3</sup>
E_M	Matrix Elastic Modulus	$E_M$	MPa
nu_M	Matrix Poisson's ratio	$\nu_M$	[-]
a_M	Matrix Coefficient of Thermal Expansion	$\alpha_M$	K <sup>-1</sup>
Cp_M	Matrix Specific Heat	$C_{pM}$	mJ/(kg K)
k_M	Matrix Thermal Conductivity	$\kappa_M$	mW/(mm K)
E_COH	Initial Elastic Stiffness	$K$	MPa
t_ult['CF']	Fiber Ultimate Traction		
t_ult['CM']	Matrix Ultimate Traction	$t_{ult}$	MPa
t_ult['CI']	Interface Ultimate Traction		
d_f['CF']	Fiber Failure Opening		
d_f['CM']	Matrix Failure Opening	$\delta_f$	mm
d_f['CI']	Interface Failure Opening		
G_f['CF']	Fiber Fracture Energy		
G_f['CM']	Matrix Fracture Energy	$G_f$	N/mm
G_f['CI']	Interface Fracture Energy		

**Table 4.3:** Input parameters: Material Properties

There is a large number of other input variables, including mesh density, number of realizations, solver settings, output requests, preferences, etc., which will not be discussed in detail.

#### 4.1.2 Geometry

The geometry of the MVE has been discussed in Section 3.2. The automatic creation of MVEs of different sizes, fiber volume fractions and fiber geometries is done at the start of

the computational framework. The important considerations regarding the geometry of the MVE are repeated below:

- Needs to be large enough to be constitutively valid
- The distribution of inclusions has to be random
- Inclusions that cross boundaries need to reappear on the opposite side

A python function (`fiber_origins.py`) was created to pick the random locations of the fibers. The fiber volume fraction specified as an input is used to compute how many fibers should be placed in the MVE. The specified fiber volume fraction can only be used as a target, since all other dimensions are fixed and fibers can only be discretely added. The program computes the maximum amount of fibers that results in a fiber volume fraction still below the target fiber volume fraction. The computed number of fibers  $N_f$  is subsequently used to compute the real fiber volume fraction, as shown below:

```
N_f = np.floor(V_ftarget*w*h/(np.pi*a*b)).astype('int')
V_f = N_f*np.pi*a*b/(w*h)
```

Now that the number of fibers that need to be distributed over the MVE is known, an equal amount of random fiber origins has to be picked. A fiber origin is the  $x$ - and  $y$ -coordinate of the center the fiber. In order to do so, first a regular fine mesh grid is created in the empty MVE, i.e. the MVE without fibers. Using a random integer generator from `numpy`, an index is generated and used to select a node from the mesh grid as the first fiber origin. The elliptical definition of the fiber is used to exclude all mesh grid nodes that are too close to the selected node, as shown in Figure 4.2. Thereafter the mesh grid is updated, by removing the picked origin and the excluded origins from the array. This process is repeated (a new random index is generated, the second fiber origin is picked, the mesh grid is updated) until the all fibers are placed.

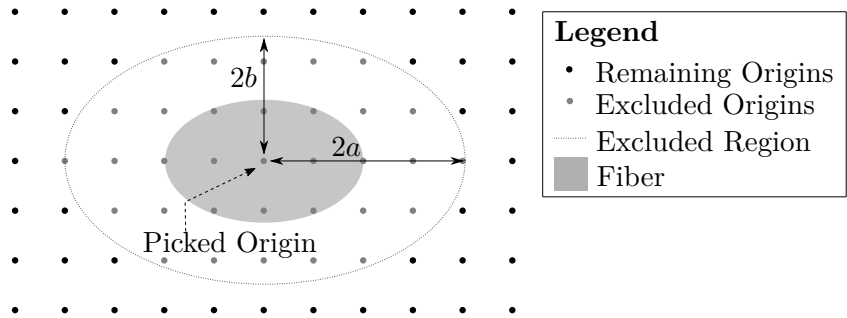


**Figure 4.2:** Method for picking fiber origins

The exclusion process of mesh grid nodes was made such that fibers crossing borders can reappear on the other side without collision. When an origin is picked within  $2a$  from a vertical border, or  $2b$  from a horizontal border, mesh grid points on the opposing edge are also removed.

For higher volume fractions and larger MVEs, the method described above can run out of possible fiber origins (mesh grid nodes) before all fibers are placed. Mesh grid nodes are removed each time a fiber is placed, which can therefore only be repeated a limited amount of times until the mesh grid array is empty. Since it is a random process the amount of fibers that can be placed before the mesh grid is empty is not constant. The program handles this issue by starting from scratch when it runs out of mesh grid nodes before all fiber origins are picked; the original mesh grid is regenerated; picked fiber origins are deleted and the process restarts. The process is very slow when larger MVEs with high fiber volume fractions are considered. The maximum MVE with  $V_f = 50\%$  and circular inclusions of  $r = 5\mu\text{m}$  created during testing was  $100 \times 100 \mu\text{m}$ . Using the same inclusion size and  $V_f = 60\%$  the maximum MVE obtained was  $75 \times 75 \mu\text{m}$ .

In Figure 4.3b, the geometry of an MVE created with the method outlined above is given as an example. Note that a fiber crossing one of the corners reappears in the three other corners. When compared to a Scanning Electron Microscope (SEM) image of an actual Fiber Reinforced Plastic (FRP), as shown in Figure 4.3a, it can be concluded that the methodology is able to mimic the random microstructure seen in reality very well.

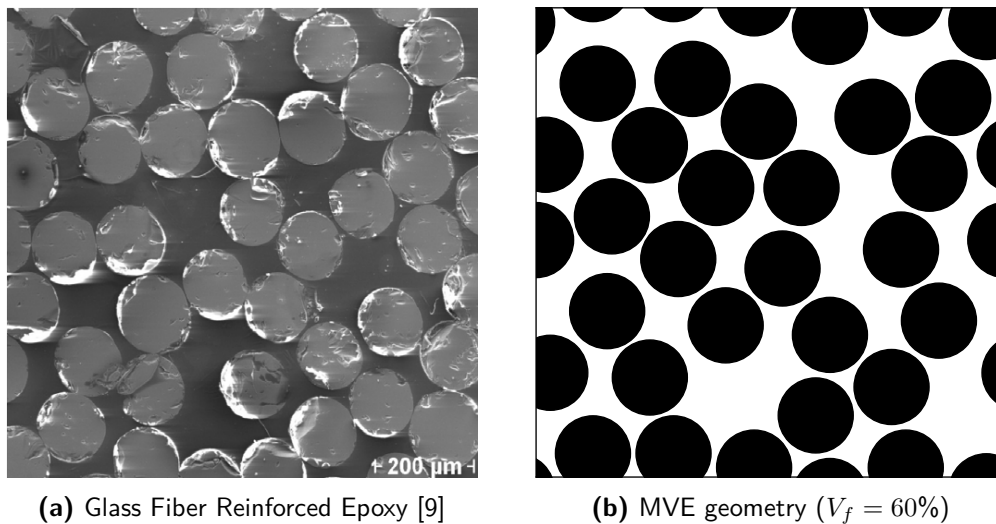


**Figure 4.3:** Microstructure comparison: SEM and MVE

### 4.1.3 Mesh

The MVE is meshed using `gms`, an open-source finite element mesh generator. Creating random meshes of low-aspect ratio elements is very straightforward in `gms`. Moreover the program allows input specification via ASCII text files in a `gms`-specific program language. This input-file provides the geometry to the mesher and is referred to as the geometry file, with the file-extension `.geo`. The standard mesh output file (`.msh`) of `gms` is also an ASCII text file.

The interaction between python and `gms` takes place via the `.geo` and `.msh` files. A python function (`mesh_gen.py`) was created to write `.geo` files using the MVE and fiber dimensions, as well as the randomly-picked fiber origin coordinates. The target node spacing, or grid size,

is also an input for `mesh_gen.py` and is passed on directly to `gmsh`. The remaining inputs are the installation folder of `gmsh`, the name of the temporary file folder where the `.geo` and `.msh` files are (over)written and the input and output file names. The usage of `mesh_gen.py` is shown below:

```
from mesh_gen import MeshGen
...
MeshGen(gmsh_bin,temp_folder,gmsh_input,gmsh_output,w,h,a,b,fiber_origins,
        grid_size)
```

When `MeshGen` is called a `.geo` file is written and stored in the temporary file folder. Thereafter the `.geo` file is executed in `gmsh` through a shell:

```
# Run GMSH
command = (gmsh_bin_windows,
mesh_input,
"-2", #Output model, then exit
)

subprocess.call(command, shell=True, stderr=subprocess.STDOUT, )
```

The mesh generation by `gmsh` follows a bottom-up approach; lines are discretized first using the specified target node spacing. The target node spacing is defined at points in the geometry and is not necessarily equal; therefore allowing for biasing/refinement. The 1D-elements created on every line are subsequently used to mesh the surfaces. This means faces of 2D-elements coinciding with internal/external boundaries share nodes with the 1D-elements used to discretize these lines. A number of meshing strategies are included in `gmsh`. The Delaunay-algorithm (`gmsh: Mesh.Algorithm=5`) was used, since it creates a random mesh of only triangular elements [28].

The output file (`.msh`) contains the mesh, i.e. nodes (node index and location) and elements (element index and connectivity). This includes the (unwanted) 1D-elements formed at the internal/external boundaries, which are disregarded when reading the mesh file in python. The mesh created using `gmsh` does not yet have embedded zero-thickness cohesive elements as this is not among the capabilities of the program. The 2D triangular mesh without cohesive elements will be referred to as the bulk-mesh.

The implementation of Periodic Boundary Conditions (PBC) requires opposing nodes on the MVE-boundaries, as will be discussed in more detail in Section 4.1.4. In practice this means every node on the left boundary needs to have a pairing-node on the right boundary with the same  $y$ -coordinate. Similarly node-pairs with the same  $x$ -coordinate are located on the top and bottom boundaries. The bulk-mesh created by `gmsh` needs to have the same mesh on opposing MVE-boundaries.

In `gmsh` there is an option that allows to specify lines that require opposing nodes. After lines have been defined in the `.geo` file, periodic lines can be defined as follows:

```
Periodic Line { expression-list } = { expression-list } ;
```

The mesh on the lines on the left-hand side (slaves) is forced to match the mesh create on the lines on the right-hand side (masters). The expression-list consists of line-numbers. Figure 4.4 shows two examples of bulk-meshes created via the python-`gmsh` framework explained above.

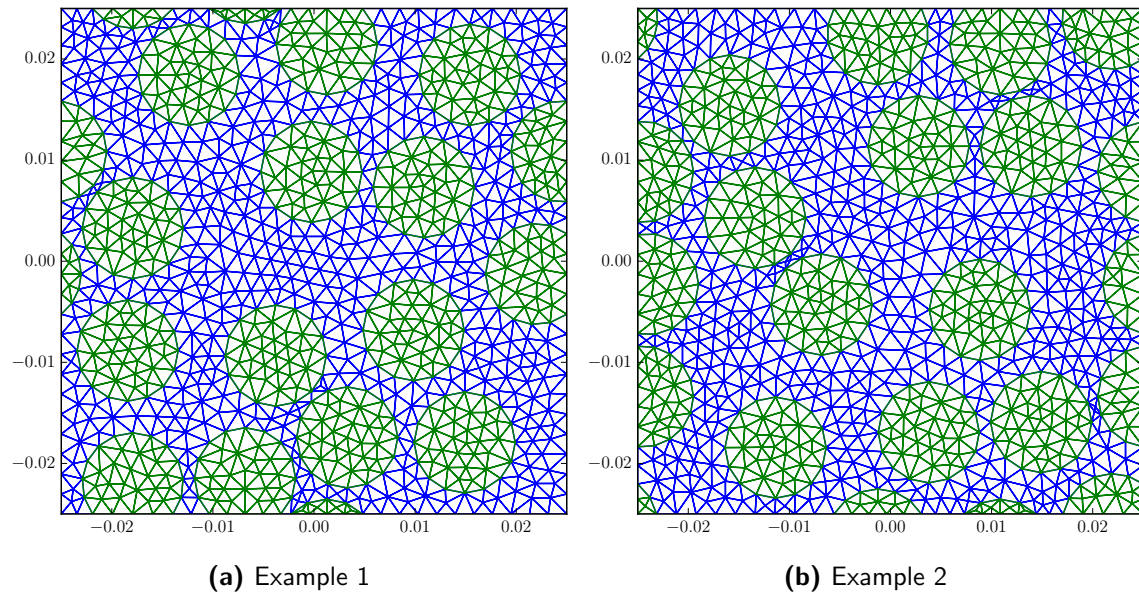


**Figure 4.4:** Two MVE meshes created using `gmsh` ( $V_f = 0.5$ ,  $w = h = 5e-2$  mm,  $a = b = 5e-3$  mm)

The mesh file created by `gmsh` is stored in the temporary file folder, where it is read by `create_input_file.py`. The usage of the function is shown below:

```
from create_input_file import CreateInputFile
...
CreateInputFile(V_f, fiber_origins, input_folder, input_file, output_folder,
                output_file)
```

The `input_folder` and `input_file` provide the location and name of the `.msh` file written by `gmsh`. The bulk-mesh of nodes and triangular elements is read stored into separate python arrays, i.e. one array with node indices and coordinates and one array with element indices and connectivity. Subsequently a loop over all elements is done to find all common faces, these are the element boundaries that are shared with other elements, i.e. all element faces except the faces that make up the boundary of the MVE. The common faces are the locations of the embedded cohesive elements.

In a number of subsequent loops, the nodes on the common faces are copied, the bulk element connectivity is updated and cohesive elements are inserted in the mesh. Three new arrays contain the information of old and new node indices and coordinates, the updated bulk element connectivity and the cohesive element connectivity. By looping over the data, the mesh is written to the ABAQUS<sup>®</sup> input file as will be discussed in more detail Section 4.1.5. The computational implementation of the boundary conditions will be discussed first in the following section.

#### 4.1.4 Thermal/Mechanical Boundary Conditions

The theoretical implementation of PBC is given by Eq. (3.8c)-(3.8f). The condition on the displacement states that the deformation field on opposing edges should be equal, making the deformed MVE repeatable through space.

In the Finite Element Method (FEM) the displacement field is solved at the node locations. The FE implementation of the PBC is therefore achieved by coupling the displacements of node-pairs located on opposite boundaries. The node-pairs on the left and right boundary are found by identifying which nodes have the same  $y$ -coordinate. Similarly the  $x$ -coordinate is used to find node-pairs on the top and bottom edges. The meshing method discussed in Section 4.1.3 ensures that these node-pairs exist.

The displacement conditions given by Eq. (3.8c) and Eq. (3.8e) result in coupling equation Eq. (4.1) for nodes located on the right ( $R$ ) and left ( $L$ ) boundary with the same  $y$ -coordinate.

$$u_1^{(R)} - u_1^{(L)} = \bar{\epsilon}_{11}w \quad (4.1a)$$

$$u_2^{(R)} - u_2^{(L)} = \bar{\epsilon}_{21}w \quad (4.1b)$$

Similarly Eq. (3.8d) and Eq. (3.8f) result in the coupling given by Eq. (4.2).

$$u_1^{(T)} - u_1^{(B)} = \bar{\epsilon}_{12}h \quad (4.2a)$$

$$u_2^{(T)} - u_2^{(B)} = \bar{\epsilon}_{22}h \quad (4.2b)$$

In ABAQUS<sup>®</sup> coupling equations can be written for nodal displacements. The right side of equations (4.1) and (4.2), the applied displacements, was imposed on two dummy nodes as shown in Figure 4.5. Equation (4.1) can now be rewritten to Eq. (4.3), a format convenient for implementation in ABAQUS<sup>®</sup>.

$$u_1^{(R)} - u_1^{(L)} - u_1^{(D-LR)} = 0 \quad (4.3a)$$

$$u_2^{(R)} - u_2^{(L)} - u_2^{(D-LR)} = 0 \quad (4.3b)$$

Similarly equation (4.2) can be rewritten to Eq. (4.4).

$$u_1^{(T)} - u_1^{(B)} - u_1^{(D-TB)} = 0 \quad (4.4a)$$

$$u_2^{(T)} - u_2^{(B)} - u_2^{(D-TB)} = 0 \quad (4.4b)$$

The coupling equations are written to the ABAQUS<sup>®</sup> input file by `CreateInputFile`, which will be discussed in Section 4.1.5.

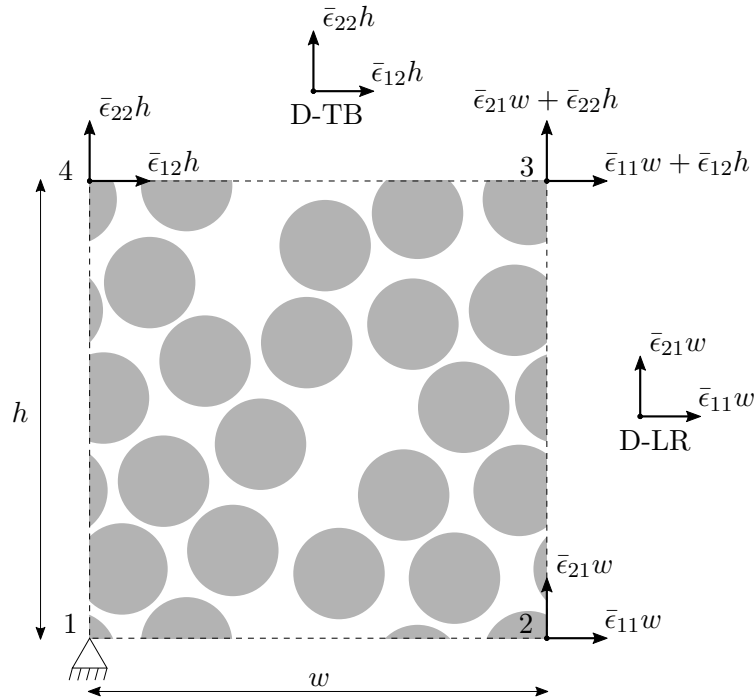


Figure 4.5: Definition of boundary conditions to the MVE

As discussed in Section 4.1.3, special care was taken, while creating the bulk-mesh in `gms`, to have a matching mesh on opposing sides of the MVE. The introduction of cohesive elements, however, complicates the formation of node-pairs for the periodicity equations. While, in the base-mesh, a node on one side of the MVE always has a pairing node on the other boundary, these two nodes are not necessarily part of the same number of elements. For example, a node on the bottom boundary might be the vertex of three elements, whereas the pairing-node on the top boundary, i.e. the node with the same  $x$ -coordinate, is the vertex of four elements. The introduction of cohesive elements will then duplicate the node on the bottom boundary two times, and the node on the top boundary three times, complicating the formation of node-pairs.

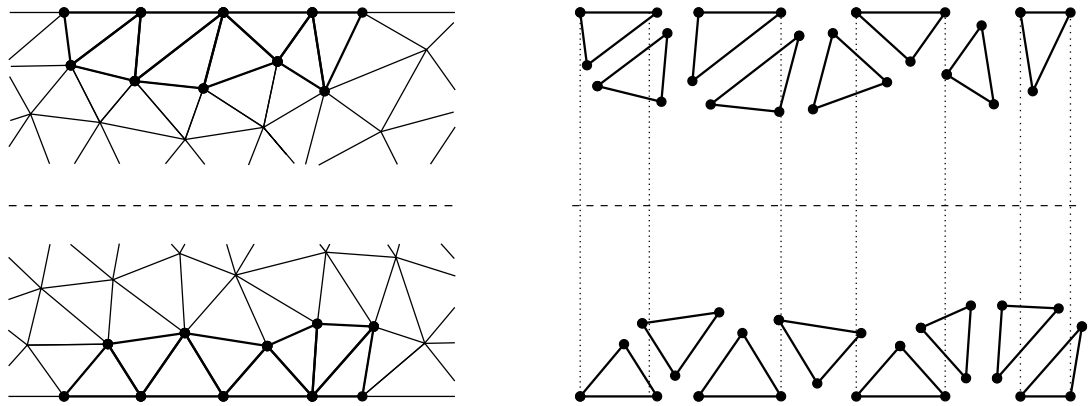
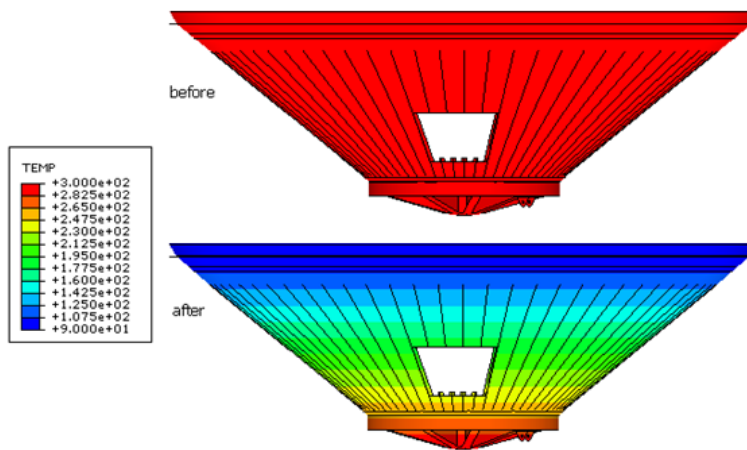


Figure 4.6: Method for defining the node pairs used for the periodic boundary conditions in a mesh with embedded cohesive elements

A method for implementing PBC in a MVE with embedded cohesive elements was proposed by van Hoorn [73]. The method implements coupling equations only to nodes belonging to elements that have two nodes on the boundary as shown in Figure 4.6.

The objective of the thesis, developing a macroscopic progressive failure criterion for Carbon Fiber Reinforced Plastic (CFRP) at cryogenic temperatures, requires a simulated temperature reduction to compute thermal residual stresses. The thermal/mechanical loads applied to the MVEs are based on the proposed application of CFRP in an Engine Thrust Frame (ETF). The ETF is a conical structure that introduces the thrust from the rocket engine into the load carrying shell of the fuel tank above. When the fuel tank is filled with Liquid Oxygen (LOX) and Liquid Hydrogen (LH<sub>2</sub>), the temperature at the fuel tank-ETF interface is reduced to as low as 77 K. Figure 4.7 shows the ETF connecting the upper stage of the Ariane 6 to the Vinci rocket engine, currently under development at Airbus Safran Launchers.



**Figure 4.7:** Initial temperature distribution (above) and temperature distribution after cooling down (below) [72]

All mechanical loads applied to the ETF before launch are negligible when compared to the forces and bending moments occurring after firing the rocket engine. The most accurate representation of the thermal/mechanical loading applied to a composite ply located close to the fuel tank-ETF interface is temperature reduction followed by mechanical loading. In the simulation this can be done by including two separate steps; a thermal load step and a mechanical load step.

The division of the problem history into steps is a basic concept in ABAQUS<sup>®</sup>. A step is any convenient phase of the history; a thermal transient, a creep hold, a dynamic transient, etc. The thermal load step is simulated using a coupled-temperature displacement step in ABAQUS<sup>®</sup>. The temperature field inside the MVE is assumed uniform through space, since the temperature gradient is not on the scale of the MVE. Like all degrees of freedom in a FE simulation, the temperature field is solved or specified at the node locations. The thermal load will be applied as a constant temperature imposed on all the nodes.

The displacement boundary conditions during the temperature step simulate free thermal expansion/contraction. The periodic boundary conditions are applied, but the dummy nodes

are left free to translate. Every constraint equation involves a displacement of one of the dummy nodes. By leaving the dummy nodes free, the displacement of these nodes will be equal to the displacement as a result of the average thermal strain. The periodicity is retained and the MVE remains repeatable through space. The displacement boundary conditions for the thermal load step are shown schematically in Figure 4.8a. Figure 4.8b shows the boundary conditions for a mechanical load step (uniaxial extension). The boundary conditions shown in Figure 4.8b are obtained by setting  $\epsilon_{11} \neq 0$ ,  $\epsilon_{12} = \epsilon_{21} = \epsilon_{22} = 0$  in Figure 4.5

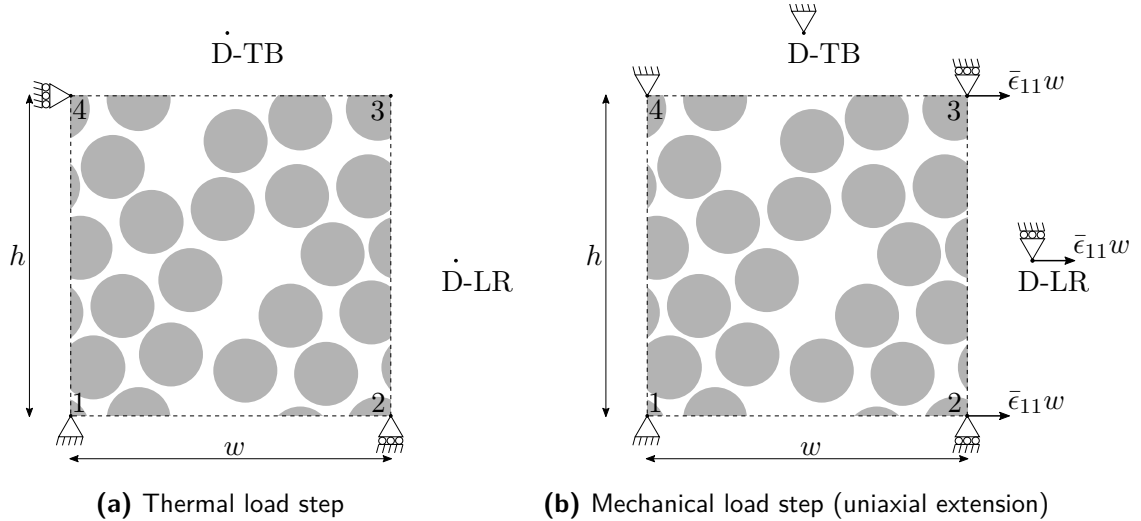


Figure 4.8: Boundary conditions applied in either load step

#### 4.1.5 Abaqus input file

As was mentioned the microscale simulations are done using the ABAQUS<sup>®</sup> solver. Normally the ABAQUS<sup>®</sup> Graphical User Interface (GUI) is used to define the geometry, create the mesh and apply the loads and boundary conditions, as well as altering options and settings related to the analysis method, convergence, assumptions, etc. When the job is submitted for analysis, an ABAQUS<sup>®</sup> input file (.inp) is written which is passed on to the solver. A job is terminology for a single Finite Element Analysis (FEA) to be performed by ABAQUS<sup>®</sup>. Multiple jobs can be created for the same model, which is often done when different load cases, meshes or analysis types are investigated. For every job a separate input file is written containing only the necessary information for that specific analysis.

The (parametrically-defined) geometry is not part of the input file, leaving the mesh as the only spatial information of the model included in the input file. The input file is an ASCII text file and is written in an ABAQUS<sup>®</sup> specific format. The computational framework writes the input file line by line using python, therefore completely bypassing the ABAQUS<sup>®</sup> GUI. The first few lines of the input file contain the header. As an example the header of the second realization of a  $62.5 \times 62.5 \mu\text{m}$  MVE is given below.

```
*Heading
** Job name: Vf50_w62um_h62um_R2 Model name: Vf50_w62um_h62um_R2
** Generated by: Abaqus/CAE 6.14-2
```

```
*Preprint, echo=NO, model=NO, history=NO, contact=NO
**
```

The header is followed by the **Part** definition. A total of three parts are defined; The MVE part followed by the two dummy nodes, each in their own part definition. A part definition contains the mesh (nodes, elements), and the section assignment. The nodes are defined by a node label and two coordinates (2D). Elements are defined by the element label and the connectivity. The connectivity are the node labels of the nodes that are vertices of the element. The bulk elements are 3-Node (triangular) full-integration plane strain elements with an extra Degree of Freedom (DOF) for the temperature (CPE3T). For the embedded cohesive elements a 4-Node cohesive element with two integration points is used (COH2D4). The node labels have to be ordered counter-clockwise for both element types, as shown in Figure 4.9. The embedded cohesive elements are zero-thickness, i.e. node 1 coincides with node 4 and node 2 coincides with node 3 in Figure 4.9b, making the counter-clockwise specification more cumbersome to enact.

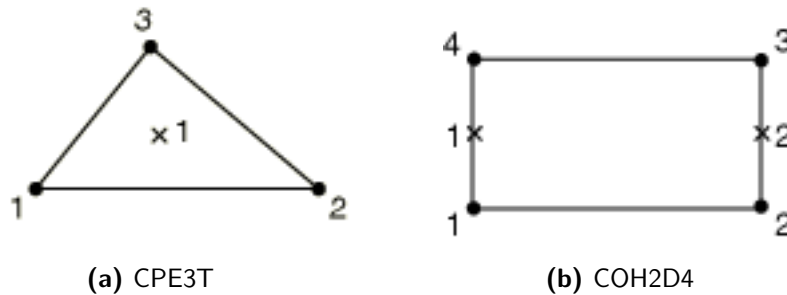


**Figure 4.9:** Element Definition: Counter-Clockwise node numbering [1]

Subsequently all elements are divided into element sets, which are used later to assign constitutive behavior, which means a total of 5 element sets are required, namely:

- **FIBER\_ELEMENTS:** Bulk elements belonging to a fiber
- **MATRIX\_ELEMENTS:** Bulk elements belonging to the matrix
- **FIBER\_COH\_ELEMENTS:** Cohesive elements embedded between two fiber bulk elements
- **MATRIX\_COH\_ELEMENTS:** Cohesive elements embedded between two matrix bulk elements
- **INTERFACE\_COH\_ELEMENTS:** Cohesive elements embedded between a fiber and a matrix bulk element

An extra two element sets are defined for output requests; a set containing all bulk elements and a set made up of all cohesive elements. After the sets are defined the section assignment is written to the input file. In the section assignment the material and element controls (element deletion, viscosity) are specified using the element sets. An overview of the part definition of all three parts is included below.

```

** PARTS
**
*Part, name= EXAMPLE_PART
**
*Node
1, X-COORD, Y-COORD
...
**
*Element, type=CPE3T
EL_ID, N_ID, N_ID, N_ID
...
**
*Element, type=COH2D4
EL_ID, N_ID, N_ID, N_ID, N_ID
...
**
*Elset, elset=EXAMPLE_SOLID_ELEMENTS
EL_ID, EL_ID, EL_ID, EL_ID,...
...
**
*Elset, elset=EXAMPLE_COHESIVE_ELEMENTS
EL_ID, EL_ID, EL_ID, EL_ID,...
...
**
** SECTION ASSIGNMENTS
**
** Section: EXAMPLE_SOLID_SECTION
*Solid Section, elset=EXAMPLE_SOLID_ELEMENTS, controls=EC-2, material=
    SOLID_MATERIAL
,
** Section: EXAMPLE_COHESIVE_SECTION
*Cohesive Section, elset=EXAMPLE_COHESIVE_ELEMENTS, controls=EC-2, material=
    COHESIVE_MATERIAL, response=TRACTION SEPARATION
,
...
**
*End Part
**
*Part, name=DUMMY_LR
*Node
DLR_ID, X-COORD , 0,
*End Part
**
*Part, name=DUMMY_TB
*Node
DTB_ID, 0, Y-COORD,
*End Part
**

```

The next section written to the input file is the **Assembly**. The assembly contains all part instances, node sets and constraint equations. The periodic boundary conditions are implemented by coupling equations for a subset of boundary nodes as was discussed in detail in Section 4.1.4. In ABAQUS<sup>®</sup>, coupling equations can only be applied to node sets. Therefore a node set is printed for every boundary node, that is to be coupled to a pairing node on the opposite boundary. After all the node sets are created, the constraint equations (see: Eq. (4.3) and Eq. (4.4)) are written. For every boundary-node-pair two constraint equations

are printed; one for  $x$ - and one for  $y$ -displacement coupling. The outline of the Assembly section is included below.

```

** ASSEMBLY
**
*Assembly, name=Assembly
**
*Instance, name=EXAMPLE_INSTANCE, part=EXAMPLE_PART
*End Instance
**
*Instance, name=DUMMY_LR-1, part=DUMMY_LR
*End Instance
**
*Instance, name=DUMMY_TB-1, part=DUMMY_TB
*End Instance
**
*Nset, nset=DUMMY_LR, instance = DUMMY_LR-1
DLR_ID
...
*Nset, nset=LEFT_NODE_N_ID, instance = EXAMPLE_INSTANCE
N_ID
*Nset, nset=RIGHT_NODE_N_ID, instance = EXAMPLE_INSTANCE
N_ID
...
** Left-Right PBC equations
*Equation
3
RIGHT_NODE_ID,1,1,LEFT_NODE_ID,1,-1,DUMMY_LR,1,-1
...
** Top-Bottom PBC equations
...
*End Assembly
**

```

At this point the input file is closed and stored in a designated storage folder. The input file is then copied to the output folder and reopened to add element controls, material properties and load steps. This framework allows for straightforward reuse of the model with different material properties and/or under altered thermal/mechanical loading. The section controls are printed directly after the assembly.

```

** ELEMENT CONTROLS
**
*Section Controls, name=EC-1, ELEMENT DELETION=NO
1., 1., 1.
*Section Controls, name=EC-2, ELEMENT DELETION=NO, VISCOSITY=0.0001
1., 1., 1.
*Section Controls, name=EC-3, ELEMENT DELETION=YES, VISCOSITY=0.0001
1., 1., 1.
**

```

Although all element controls have been investigated during testing, EC-2, i.e. no element deletion and with viscosity, has been used for most simulations. Element deletion is only applicable to the cohesive elements and when turned on (EC-3) it will remove fully damaged

cohesive elements in real time. The viscosity is used to specify the viscous coefficient in the viscous regularization scheme. The viscous regularization helps the simulation cope with a sudden change in stiffness, such as the peak in a bilinear cohesive zone material law.

The next section printed to the input file contains the material definition. The material properties are python variables, defined at the start of `00_submit_jobs.py`, and are for the most part directly printed to the input file. The exception is the Coefficient of Thermal Expansion (CTE). ABAQUS® can handle temperature-dependent thermal expansion coefficients, but only in so-called total form [1]. Experimental data on CTEs are usually presented as a current or tangent thermal expansion coefficient, because in contrast to a total thermal expansion coefficient the current thermal expansion coefficient does not require a reference temperature ( $\theta_0$ ). The input specification at the start of the preprocessing script requires the CTE to be given as a current value. The CTE therefore needs to be converted to the total format before it can be printed to the ABAQUS® input file. The difference between total and tangent CTEs is illustrated in Figure 4.10.

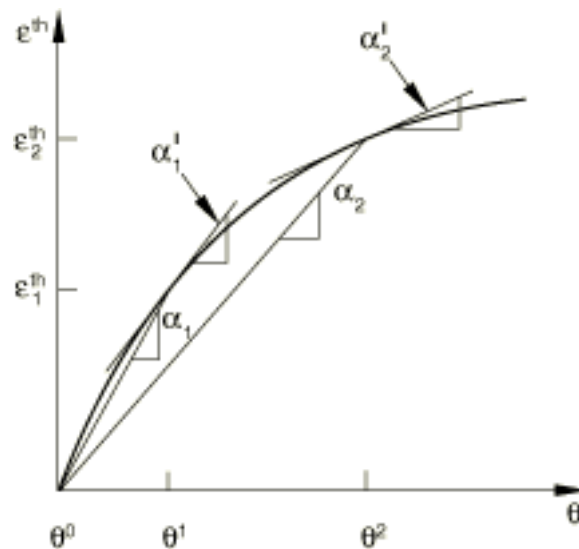


**Figure 4.10:** Definition of the thermal expansion coefficient (tangent:  $\alpha'$ , total:  $\alpha$ ) [1]

The material properties are printed to the ABAQUS® input file as follows:

```
** MATERIALS
**
*Material, name=SOLID_MATERIAL
*Conductivity
κ
*Density
ρ
*Elastic
E, ν, θ1
E, ν, θ2
*Expansion, ZERO=300.0
α, θ1
α, θ2
```

```

*Specific Heat
Cp
*Material, name=COHESIVE_MATERIAL
*Damage Initiation, criterion=MAXS
tult, tult, tult, θ1
tult, tult, tult, θ2
*Damage Evolution, type=ENERGY
Gf, θ1
Gf, θ2
*Elastic, type=TRACTION
K, K, K
**

```

The (thermal) loads and boundary conditions have been discussed in Section 4.1.4. The thermal and mechanical loads are introduced through prescribed uniform temperature and displacements at the control nodes respectively in two consecutive steps. The computational framework allows to control the order, i.e. thermal load followed by mechanical load or vice versa. The former is in keeping with the sequence seen in the launcher thrust frame of a cryogenic second stage, as discussed in Section 4.1.4. Moreover the framework can leave out either step entirely. The remainder of this section will focus on the case of interest; A reduction of temperature to cryogenic conditions followed by a mechanical load.

There is only one boundary condition constant regardless of the analysis, namely the pinned condition of the lower left corner (Corner 1), as shown in Figure 4.5. The node(s) located in this corner are fixed in both translational degrees of freedom, which is communicated to the ABAQUS<sup>®</sup> solver by:

```

** BOUNDARY CONDITIONS
**
** Name: BC_NODE_C1 Type: Displacement/Rotation
*Boundary
NODE_C1, 1, 1
NODE_C1, 2, 2

```

The initial temperature has to be specified for every simulation, even when the thermal load step is omitted, since some material properties are given as a function of temperature. The initial temperature is defined as a uniform predefined field, which shows up in the ABAQUS<sup>®</sup> input file as follows:

```

**PREDEFINED FIELDS
**
** Name: INITIAL_TEMP Type: Temperature
*Initial Conditions, type=TEMPERATURE
ALL_NODES, T0

```

The thermal load is applied through a boundary condition in a load step. This thermal boundary condition remains active throughout the rest of the simulation, i.e. also during the subsequent mechanical load step. During the thermal load step Corner 2 is constraint in  $y$ -direction, while Corner 4 is restricted to translate in  $x$ -direction as shown in Figure 4.8a. The boundary conditions applied in the thermal load step are included in the ABAQUS<sup>®</sup> input file as follows:

```

** BOUNDARY CONDITIONS
**
** Name: BC_NODE_C2 Type: Displacement/Rotation
*Boundary
NODE_C2, 2, 2
** Name: BC_NODE_C3 Type: Displacement/Rotation
*Boundary
NODE_C4, 1, 1
** Name: BC_TEMP Type: Temperature
*Boundary
ALL_NODES, 11, 11, 77

```

In the consecutive mechanical load step, some of the boundary conditions have to be updated or removed and new prescribed displacements are added. In ABAQUS® the keyword `op=NEW` is used to respecify a boundary condition. For a uniaxial extension step (see Figure 4.8b) the following boundary conditions are specified for Corner 3, which had been left completely free during the thermal load step.

```

** Name: BC_NODE_C3-1 Type: Displacement/Rotation
*Boundary, op=NEW
NODE_C3, 1, 1,  $\epsilon_{11w}$ 
** Name: BC_NODE_C3-2 Type: Displacement/Rotation
*Boundary, op=NEW, fixed
NODE_C3, 2, 2, 0.0

```

## 4.2 Solver: Settings and convergence

The ABAQUS® solver has a large number of settings influencing the convergence of the solution. As was mentioned before, the sudden change in stiffness after localization of the crack has a detrimental effect on the solution convergence. The `*Controls` keyword allows to reset solution controls in the input file. For standard ABAQUS® analyses, it is not recommended to change time increment parameters. The complexity and nonlinearity of the problem at hand, however, require to give the solver more means and time to converge. Therefore three time increment parameters are modified and are specified as inputs:

```

*Controls, parameters=time incrementation
I0, IR, , , , IA, , ,

```

The definition of the time increment parameters as listed in the ABAQUS® user guide [1] is included in Table 4.4.

Variable	Description	Symbol
<code>n_eqm_res</code>	Number of equilibrium iterations after which the check is made whether the residuals are increasing in two consecutive iterations	$I_0$
<code>n_eqm_log</code>	Number of consecutive equilibrium iterations at which logarithmic rate of convergence check begins	$I_R$
<code>n_attempts</code>	Maximum number of cutbacks allowed for an increment	$I_A$

**Table 4.4:** Input parameters: Solver Settings [1]

For severely discontinuous behavior, ABAQUS® recommends increasing the  $I_0$  and  $I_R$  parameters from their default values of 4 and 8 respectively to  $I_0 = 8$  and  $I_R = 10$  [1]. The maximum number of cutbacks was increased from 5 to 50. A cutback is a new attempt to converge by reducing the time increment in the load step by a factor 4 (default). This is necessary to handle the sharp transition from the hardening portion, where relatively large time increments are possible, to the softening portion of the simulation.

The maximum number of increments is specified as a procedure definition option of the `*Step`. The thermal load step is analyzed as a `*Coupled Temperature-Displacement`, which is used when a simultaneous solution of temperature and displacement fields is necessary. The mechanical load step is analyzed as a `*Static`, a static stress/displacement analysis. The macroscopic fracture process occurs during the mechanical load step. The automatic stabilization option (`stabilize`) is activated, allowing ABAQUS® to viscously dissipate energy to cope with local instabilities. The maximum allowable ratio of the stabilization energy to the total strain energy is kept at the default value of 5% (`allsdtol=0.05`).

In Figure 4.11, the energy evolution in a typical microscale fracture simulation is included. The energy dissipated by the automatic stabilization algorithm (cyan) does exceed the 5% threshold towards the end of the simulation ( $t > 0.6$  s). The ABAQUS® solver will attempt to keep the automatic stabilization energy below 5% of the total strain energy, but it is not a hard requirement and the simulation will not be aborted.

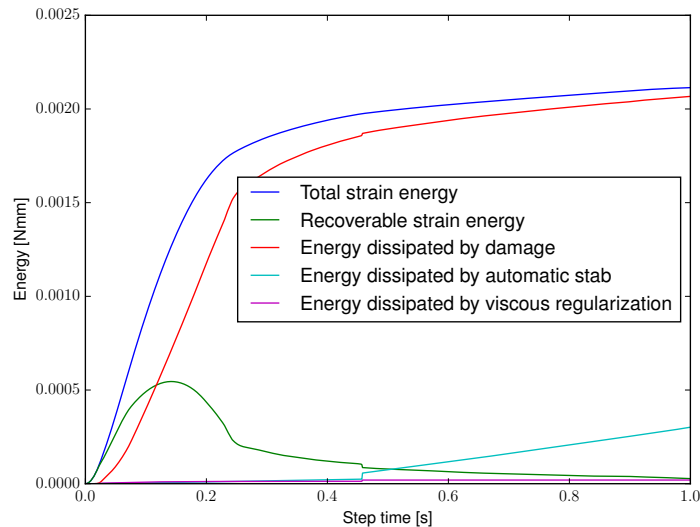


Figure 4.11: Energy evolution in a typical simulation

### 4.3 Postprocessing

The output files of a FE simulation are typically very large contain a range of nodal and elemental results for every node/element at every time step. The result files contain all the information, but are impossible to comprehend as a whole. The process with the goal of obtaining an understandable (graphical) representation of the results is referred to as postprocessing.

### 4.3.1 Data extraction and processing

The standard output file of an ABAQUS<sup>®</sup> simulation is the output database (.odb), a binary output file that can be read by ABAQUS<sup>®</sup> to view results. The output database cannot be opened directly in `python`. The postprocessing framework, however, will be `python` based to facilitate the extensive result analysis needed to achieve the project goal, including:

1. Graphical (a posteriori) approximation of the Hill-Mandel Condition
2. Averaging of constitutive (fracture) behavior of multiple realizations
3. Convergence checks on mesh and MVE size
4. Plotting and comparing results of interest for different load cases

ABAQUS<sup>®</sup> has to be incorporated in the postprocessing framework to handle the output file format. The Abaqus Scripting Interface (ASI) is an Application Programming Interface (API) that allows access to the model and data used by ABAQUS<sup>®</sup>. The ASI can, among other things, be used to read and write to an output database. ASI scripts are written in the `python` programming language (.py).

The postprocessing framework writes ASI scripts that are executed with ABAQUS<sup>®</sup> on the computational cluster, which is also where the output database files are stored after the simulation is completed. Besides reading the data from the output database, the ASI script performs the bulk and crack averaging operations discussed in Section 3.3 and computes a number of integrals to check the Hill-Mandel condition. The `python` object structures that contain the results of interest are serialized using the `pickle` module and written to a file. The pickle file is subsequently downloaded from the cluster and can be reopened in other `python` scripts.

The ASI script is created by modification of a base file. The base file is a `python` script that contains all operations. By inserting model-specific data (file name, geometrical data) to the input section of the base file, an ABAQUS<sup>®</sup> runnable ASI script is created. The activities in the postprocessing framework are shown schematically in Figure 4.12.

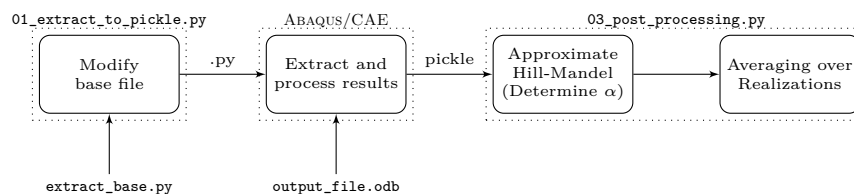


**Figure 4.12:** Schematic representation of the postprocessing framework

The rest of the section focuses on the extraction and data processing using the ASI script. The output database can be opened using `openOdb` imported from the `odbAccess` module:

```
odb_file = openOdb(os.sep.join([output_path, model_name + '.odb']), readOnly=True)
```

The homogenization method was discussed in detail in Section 3.3. The algorithm included at the end of Section 3.3 contains the sequentiality of the theoretical method. The practical implementation follows the same logic, but the first two steps, consisting of the processing of the final state and the time incremental postprocessing, are combined in a single backwards running loop over the time steps.

Inside the loop over the time steps are two nested loops; one over the bulk elements and one over all cohesive elements. These loops extract data for each element and perform the volume and crack integration procedures.

As part of the time incremental postprocessing, the volume averaged stress tensor is computed at every time step. The volume integral is approximated as the discrete sum given by Eq. (4.5).

$$\langle \boldsymbol{\sigma} \rangle_{\Omega} = \frac{1}{wh} \sum_{j=1}^{N_{\text{bulk}}} \boldsymbol{\sigma}_j A_j^e \quad (4.5)$$

where  $A_j^e$  is the area of the  $j^{\text{th}}$  element in the undeformed state. The volume averaged strain tensor is computed in a similar manner and is given by Eq. (4.6).

$$\langle \boldsymbol{\epsilon} \rangle_{\Omega} = \frac{1}{wh} \sum_{j=1}^{N_{\text{bulk}}} \boldsymbol{\epsilon}_j A_j^e \quad (4.6)$$

The Hill-Mandel condition on the energy requires that the work performed in the macroscale equals the work performed in the microscale. The aforementioned condition translates to "the product of the averages equals the average of the products". The Hill-Mandel condition in the bulk is given by Eq. (4.7).

$$\langle \boldsymbol{\sigma} \rangle_{\Omega} \cdot \langle \boldsymbol{\epsilon} \rangle_{\Omega} = \langle \boldsymbol{\sigma} \cdot \boldsymbol{\epsilon} \rangle_{\Omega} \quad (4.7)$$

The choice in boundary conditions (periodic) should ensure the bulk Hill-Mandel condition is satisfied a priori. It is, however, still useful to check as there is an expected influence of numerics, such as discretization and viscous regularization. The right-hand side of Eq. (4.7), referred to as the volume averaged stress work, is computed using Eq. (4.8).

$$\langle \boldsymbol{\sigma} \cdot \boldsymbol{\epsilon} \rangle_{\Omega} = \frac{1}{wh} \sum_{j=1}^{N_{\text{bulk}}} \boldsymbol{\sigma}_j \cdot \boldsymbol{\epsilon}_j A_j^e \quad (4.8)$$

As was discussed in Section 3.3, the Hill-Mandel condition in rate-form is used to determine the effective traction vector that is used to formulate the Effective Traction Separation Law (ETSL). The bulk stress power is computed as the inner product of the stress tensor with the strain rate tensor. The strain rate is obtained using a forward finite difference scheme, as given by Eq. (4.9).

$$\dot{\boldsymbol{\epsilon}}_n = \frac{\boldsymbol{\epsilon}_{n+1} - \boldsymbol{\epsilon}_n}{t_{n+1} - t_n} \quad (4.9)$$

The volume averaged strain rate tensor is computed by a summation, similar to Eq. (4.6) and the volume averaged stress power is computed by the rate equivalent of Eq. (4.8).

After the bulk integration completed, the crack averaged quantities are computed. Crack based integrals are computed numerically by summation over the subset of cohesive elements containing the cohesive elements that have failed. The first step is therefore to determine the

elements that belong to this subset. The final state of the simulation is used to determine whether a cohesive element has failed or not.

As was discussed in Section 3.1, the history parameter  $\kappa$  keeps track of the maximum separation that has occurred during the damage process. When the history parameter exceeds the failure opening of the Traction-Separation Law (TSL) the element is fully failed. ABAQUS® does not use the maximum separation to track the point on the TSL, but instead uses the stiffness degradation parameter  $\omega$  (see Figure 3.2). The stiffness degradation parameter is bound between 0 (completely intact) and 1 (fully failed) and is directly related to the history parameter in the interval  $\delta_0 \leq \kappa \leq \delta_f$ .

The stiffness degradation parameter is requested as a field output for every cohesive element. The stiffness degradation parameter of the element is taken as the average of the (two) integration points, as shown in the `python` code included below.

```
SDEG = 0
for k in range(0, n_int_points):
    SDEG += np.array(oddb_file.steps[load_step_name].frames[ind_frame]
                    .fieldOutputs['SDEG'].values[coh_value_idx+k].data)
SDEG = SDEG/n_int_points
```

Instead of only including cohesive elements for which the stiffness degradation is equal to 1, corresponding to fully failed, a cut-off value is specified based on the residual strength. When the maximum traction that can still be carried by the cohesive element is below a predefined percentage of the undamaged ultimate traction, the element is assumed to be failed. For most simulations a cut-off value of 20% of the undamaged strength was used. For all failed element the element index is stored to verify whether the method for selecting failed elements corresponds to the crack geometry visible in the deformation plot.

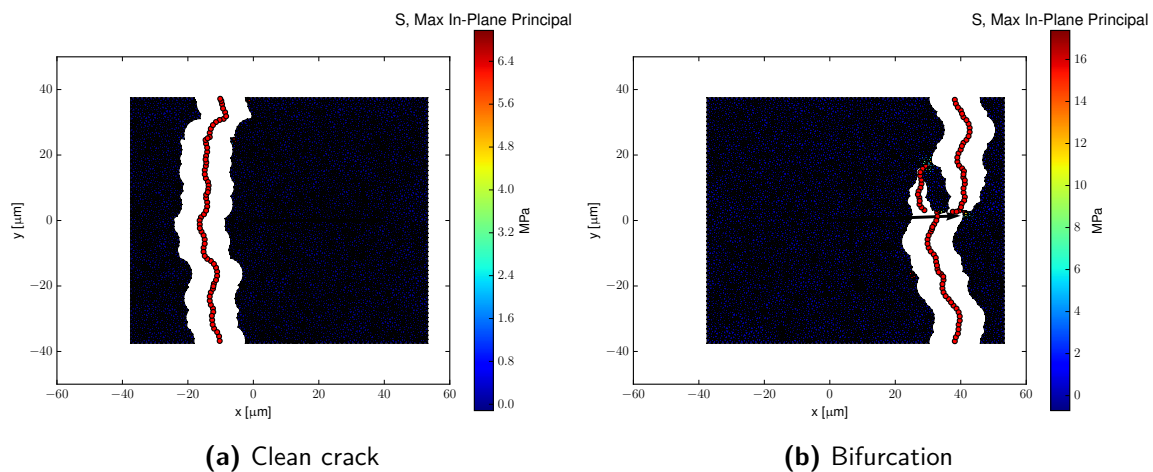


**Figure 4.13:** Deformation and maximum in-plane principal stress at the final state of the simulation (Failed cohesive elements: ●)

With the set of failed elements known it is possible to compute the microscopic crack length  $|\Gamma|$  by a simple addition of all the cohesive element lengths  $\Gamma^e$  of the elements that have failed,

as given by Eq. (4.10).

$$|\Gamma| = \sum_{j=1}^{N_{\text{coh}}^{\Gamma}} \Gamma_j^e \quad \text{at } t = t_F \quad (4.10)$$

As was discussed in Section 3.3, the product of the effective macroscopic crack, length, opening and normal form the best rank one approximation to the right hand side of Eq. (3.25). The right hand side is the integral of the tensor product of the local opening and the local crack normal over the crack, and is approximated as the discrete sum given by Eq. (4.11).

$$|\Gamma| \langle [\mathbf{u}] \otimes \mathbf{m} \rangle_{\Gamma} = \sum_{j=1}^{N_{\text{coh}}^{\Gamma}} [\mathbf{u}]_j \otimes \mathbf{m}_j \Gamma_j^e \quad (4.11)$$

The local opening vector is not directly available from the simulation and is computed using the displacements of the four corner nodes, as illustrated in Figure 4.14.

$$[\mathbf{u}] = \mathbf{u}_4 + \mathbf{u}_3 - \mathbf{u}_2 - \mathbf{u}_1 \quad (4.12)$$

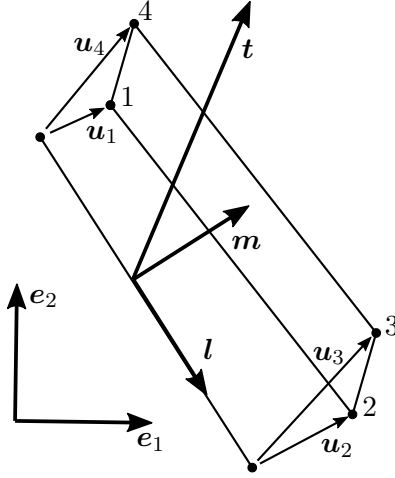


**Figure 4.14:** Cohesive element: Initial and deformed/opened state

Singular Value Decomposition (SVD) of a  $m \times n$  tensor  $\mathbf{M}$  is a factorization of the form:

$$\mathbf{M} = \mathbf{U} \mathbf{\Sigma} \mathbf{V}^T$$

Where  $\mathbf{U}$  is an  $m \times m$  unitary matrix,  $\mathbf{\Sigma}$  a  $m \times n$  diagonal matrix and  $\mathbf{V}$  is an  $n \times n$  unitary matrix. The diagonal entries of  $\mathbf{\Sigma}$ , denoted  $\sigma_i$  are the singular values. The Eckart-Young theorem states that the best rank  $k$  approximation, in terms of both the spectral as well as the Frobenius norm, to  $\mathbf{M}$  is given by Eq. (4.13) [22].

$$\mathbf{M}_k = \sum_{i=1}^k \sigma_i \mathbf{u}_i \mathbf{v}_i^T \quad (4.13)$$

where  $\mathbf{u}_i$  and  $\mathbf{v}_i$  are the  $i^{\text{th}}$  columns of  $\mathbf{U}$  and  $\mathbf{V}$  respectively. Using SVD the best rank one approximation to second order tensor computed using Eq. (4.11) can be computed. The effective macroscopic crack normal can then be extracted using the condition that the normal is of unit length as discussed in Section 3.3. In python the SVD is included in the `numpy.linalg` package:

```
U, S, V = np.linalg.svd(temp_E_int)
m_f = V[0, :].T
```

The effective macroscopic crack normal is used to compute the equivalent macroscopic crack length  $|\Gamma|^f$ , using Eq. (3.15). Subsequently the effective macroscopic crack opening can be computed for every time step.

$$\llbracket \mathbf{u} \rrbracket_n^f = \frac{|\Gamma| \langle \llbracket \mathbf{u} \rrbracket_n \otimes \mathbf{m} \rangle_\Gamma}{|\Gamma|^f} \mathbf{m}^f \quad \text{at } t = t_n$$

Combining the effective macroscopic crack opening vector and the effective macroscopic traction vector history results in the ETSL. The effective macroscopic traction vector is computed as a weighted average of the volume-averaged stress acting on the crack surface and the crack averaged traction. The former is computed by multiplication of the volume-averaged stress with the effective macroscopic crack normal, as given by Eq. (3.20). The crack averaged traction is computed using the definition given by Eq. (3.19) and is evaluated for every time step.

$$\langle \mathbf{t}_n \rangle_\Gamma^f = \frac{|\Gamma| \langle \mathbf{t}_n \otimes \mathbf{m} \rangle_\Gamma}{|\Gamma|^f} \mathbf{m}^f \quad \text{at } t = t_n$$

The integral term in de numerator is computed as a sum over all failed cohesive elements as given by Eq. (4.14).

$$|\Gamma| \langle \mathbf{t} \otimes \mathbf{m} \rangle_\Gamma = \sum_{j=1}^{N_{\text{coh}}^\Gamma} \mathbf{t}_j \otimes \mathbf{m}_j \Gamma_j^e \quad (4.14)$$

The traction of the  $j^{\text{th}}$  element at time step  $t = t_n$  is field output of the simulation and can be accessed as follows:

```
t = odb_file.steps[load_step_name].frames[ind_frame].fieldOutputs['S'].values[
    tot_value_idx].data
```

The traction is given per integration point and in the cohesive element coordinate system. The traction of the cohesive element is taken as the average of the traction vectors at the two integration points. The traction can be transformed to the global basis using the element normal and tangent vectors as shown in Figure 4.14.

$$t_l + t_m \mathbf{m}$$

Which is equivalent to the following rotation:

$$\mathbf{t} = \mathbf{Q}^T \mathbf{t}' \quad (4.15)$$

with  $\mathbf{t}'$  as the traction vector in the cohesive element basis:

$$\mathbf{t}' = \begin{bmatrix} t_l \\ t_m \end{bmatrix} \quad (4.16)$$

and rotation matrix  $\mathbf{Q}$  given by Eq. (4.17).

$$\mathbf{Q} = \begin{bmatrix} \mathbf{l}^T \\ \mathbf{m}^T \end{bmatrix} \quad (4.17)$$

### 4.3.2 Multiscale coupling: Hill-Mandel

The multiscale coupling is achieved through satisfying the Hill-Mandel condition. The periodic boundary conditions are sufficient to satisfy the global Hill-Mandel condition [69]. The scale transition of the crack is, however, not satisfied a priori.

In Section 3.3 the effective macroscopic traction vector  $\mathbf{t}^f$  has been defined as a linear combination of the volume- and crack-averaged tractions acting on the crack surface:

$$\mathbf{t}_n^f = \alpha(\mathbf{t}_n)_\Gamma^f + (1 - \alpha)(\mathbf{t}_n)_\Omega^f$$

The weighting factor  $\alpha$  is determined as the best approximation of the crack power in the microscale. All relevant power terms are computed for every time step. In Figure 4.15 the power evolution over a typical (uniaxial extension) simulation is included.

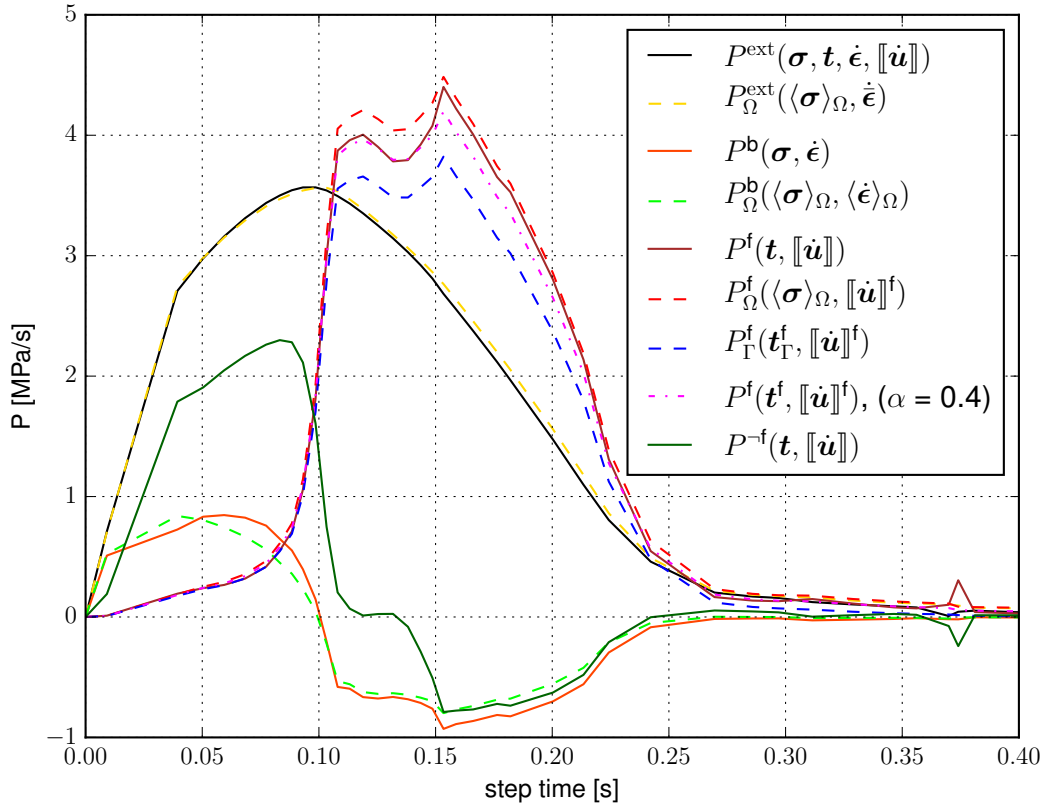


**Figure 4.15:** Power evolution for a typical uniaxial extension simulation ( $75 \times 75 \mu\text{m}$  MVE)

The definition of the power terms plotted in Figure 4.15 are included in Eq. (4.18). The rate terms ( $\dot{\epsilon}$ ,  $[[\dot{\mathbf{u}}]]$ ) are computed by a forward difference scheme.

$$P^{\text{ext}}(\boldsymbol{\sigma}, \mathbf{t}, \dot{\epsilon}, [[\dot{\mathbf{u}}]]) = P^{\text{b}} + P^{\text{f}} + P^{-\text{f}} \quad (4.18\text{a})$$

$$P_{\Omega}^{\text{ext}}(\langle \boldsymbol{\sigma} \rangle_{\Omega}, \dot{\boldsymbol{\epsilon}}) = \langle \boldsymbol{\sigma} \rangle_{\Omega} \cdot \dot{\boldsymbol{\epsilon}} \quad (4.18\text{b})$$

$$P^{\text{b}}(\boldsymbol{\sigma}, \dot{\epsilon}) = \frac{1}{\Omega} \int_{\Omega} \boldsymbol{\sigma} \cdot \dot{\epsilon} \, d\Omega \quad (4.18\text{c})$$

$$P_{\Omega}^{\text{b}}(\langle \boldsymbol{\sigma} \rangle_{\Omega}, \langle \dot{\epsilon} \rangle_{\Omega}) = \langle \boldsymbol{\sigma} \rangle_{\Omega} \cdot \langle \dot{\epsilon} \rangle_{\Omega} \quad (4.18\text{d})$$

$$P^{\text{f}}(\mathbf{t}, [[\dot{\mathbf{u}}]]) = \frac{1}{\Omega} \int_{\Gamma} \mathbf{t} \cdot [[\dot{\mathbf{u}}]] \, d\Gamma \quad (4.18\text{e})$$

$$P_{\Omega}^{\text{f}}(\langle \boldsymbol{\sigma} \rangle_{\Omega}, [[\dot{\mathbf{u}}]]^{\text{f}}) = \frac{1}{\Omega} |\Gamma^{\text{f}}| \langle \boldsymbol{\sigma} \rangle_{\Omega} \mathbf{m}^{\text{f}} \cdot [[\dot{\mathbf{u}}]]^{\text{f}} \quad (4.18\text{f})$$

$$P_{\Gamma}^{\text{f}}(\mathbf{t}_{\Gamma}^{\text{f}}, [[\dot{\mathbf{u}}]]^{\text{f}}) = \frac{1}{\Omega} |\Gamma^{\text{f}}| \mathbf{t}_{\Gamma}^{\text{f}} \cdot [[\dot{\mathbf{u}}]]^{\text{f}} \quad (4.18\text{g})$$

$$P^{\text{f}}(\mathbf{t}^{\text{f}}, [[\dot{\mathbf{u}}]]^{\text{f}}) = \frac{1}{\Omega} |\Gamma^{\text{f}}| \mathbf{t}^{\text{f}} \cdot [[\dot{\mathbf{u}}]]^{\text{f}} \quad (4.18\text{h})$$

$$P^{-\text{f}}(\mathbf{t}, [[\dot{\mathbf{u}}]]) = \frac{1}{\Omega} \int_{-\Gamma} \mathbf{t} \cdot [[\dot{\mathbf{u}}]] \, d\Gamma \quad (4.18\text{i})$$

The relation given by Eq. (4.18i) computes the power of the "not crack". There is no physical interpretation to this power as it relates to a purely numerical effect. The model has cohesive elements embedded between all bulk elements and not solely at the crack location, as the crack geometry is not known a priori. When the failed elements are identified at the end of the simulation, the majority of cohesive elements are excluded from the failed set. The initial elastic opening and limited damage in these not-failed cohesive elements, combined with the size of the not-failed element set, makes that the work rate in these elements is not negligible. The power of the not-failed cohesive elements also amounts to a significant portion of the total external power in the microscale, computed using Eq. (4.18a). The stress power integral performed for the failed elements is therefore also computed for the not-failed elements.

Figure 4.15 is used to verify all three Hill-Mandel conditions; the global, bulk and crack based scale transitions:

$$\begin{array}{lll} \text{Global:} & P_{\Omega}^{\text{ext}}(\langle \boldsymbol{\sigma} \rangle_{\Omega}, \dot{\boldsymbol{\epsilon}}) \approx P^{\text{ext}}(\boldsymbol{\sigma}, \mathbf{t}, \dot{\epsilon}, [[\dot{\mathbf{u}}]]) & \text{---} \approx \text{---} \\ \text{Bulk:} & P_{\Omega}^{\text{b}}(\langle \boldsymbol{\sigma} \rangle_{\Omega}, \langle \dot{\epsilon} \rangle_{\Omega}) \approx P^{\text{b}}(\boldsymbol{\sigma}, \dot{\epsilon}) & \text{---} \approx \text{---} \\ \text{Crack:} & P^{\text{f}}(\mathbf{t}^{\text{f}}, [[\dot{\mathbf{u}}]]^{\text{f}}) \approx P^{\text{f}}(\mathbf{t}, [[\dot{\mathbf{u}}]]) & \text{---} \approx \text{---} \end{array}$$

As expected the global Hill-Mandel condition is satisfied (see black solid and yellow dashed lines). The discrepancy in the curves belonging to the bulk material is noticeable, but still within reasonable a margin. Most important to the present analysis is the separate scale transition relation of the crack. By combining the stress power relations resulting from the volume-averaged and crack-averaged traction acting on the crack surface, the best match to the microscopic stress power of the crack was found for  $\alpha = 0.4$ . This value of  $\alpha$  is subsequently used to compute the effective macroscopic traction vector. Combining the effective macroscopic traction vector with the effective macroscopic crack opening vector the Mode I and Mode II ETSLs can be constructed. The Mode I ETSL of the example uniaxial extension simulation is included in Figure 4.16.

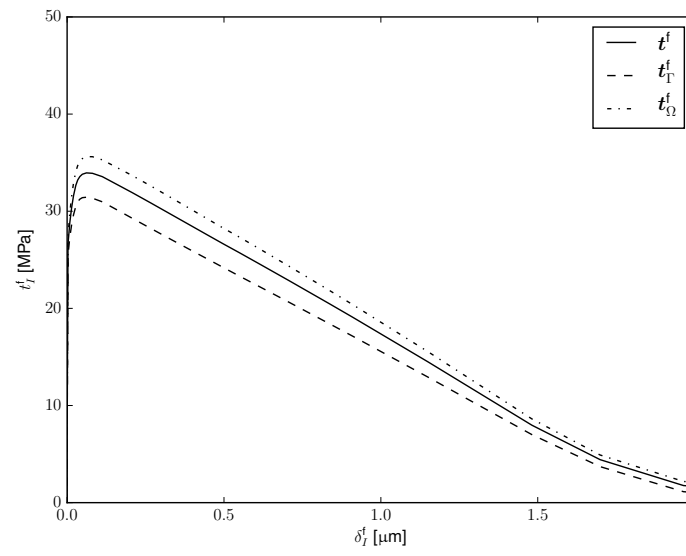


**Figure 4.16:** ETLS for Mode I obtained for  $\alpha = 0.4$

# Multiscale Traction-Separation Laws at Room Temperature

The computational framework discussed in Chapter 4 is able to create and analyze Microstructural Volume Elements of different sizes and process the results. Next to the outer dimensions, the fiber radii (elliptical definition) and volume fraction can be controlled. Before the homogenized microscale results can be used at the macroscopic scale convergence has to be established.

Two types of convergence are distinguished; namely *mesh convergence* and *size convergence*. Mesh convergence simply means that refining the mesh does not change the results. A common method of establishing mesh convergence requires data points of a critical result parameter and the corresponding mesh density. Typically the curve, obtained by connecting these data points, asymptotically approaches the unknown converged result. A minimum of three convergence runs, of different mesh densities, will therefore be required to plot a curve that can indicate whether convergence is achieved, an even finer mesh is required or the result is diverging.

The notion of size convergence refers to establishing the Representative Volume Element (RVE) size. As was discussed in Section 3.2, the RVE is a Microstructural Volume Element (MVE) for which increasing the size does not alter the results of interest, in this case the fracture behavior. The lack of a straightforward RVE size definition for softening behavior, such as cohesive fracture, motivated Gitman et al. [29] to propose a convergence study as the most suitable technique to determine the RVE size (see: Figure 2.14). For this thesis the same approach was followed. The smallest MVE tested is a square unit cell as shown in Figure 5.1. A unit cell, when repeated through space, results in a very ordered/regular microstructure.

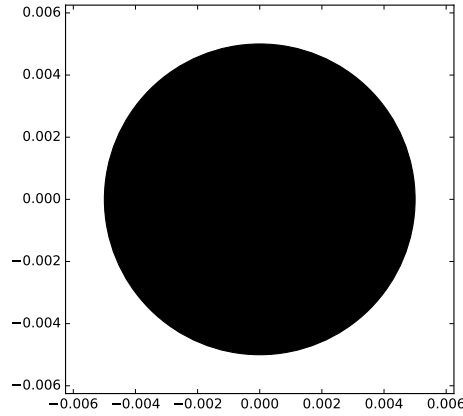


**Figure 5.1:** Unit cell ( $12.5 \times 12.5 \mu\text{m}$ )

The random fiber distribution, that exists in real lamina, is captured by the larger MVEs shown in Figure 5.2. The largest MVE tested in the size convergence study is  $75 \times 75 \mu\text{m}$ . Obviously there is an infinite number of possibilities to position the randomly distributed fibers and Figure 5.2 presents just one possibility per size. Since the fiber distribution has an effect on the results, five realizations are created for each of the considered dimensions to obtain a measure of the spread.

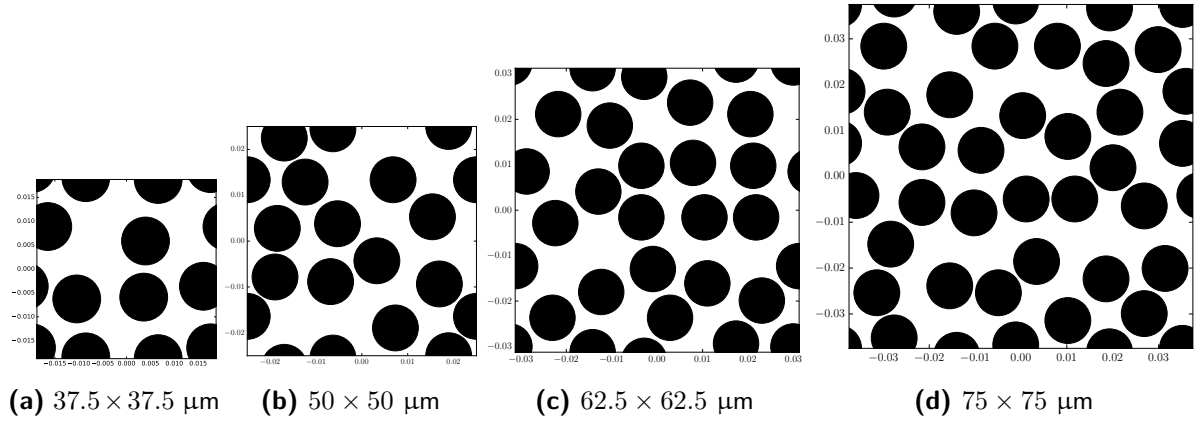


**Figure 5.2:** MVE sizes tested in the convergence study

The unit cell and the larger MVEs were obtained using a target fiber volume fraction of  $V_f = 50\%$ . Since the outer and inclusion dimensions are fixed/input, the real fiber volume fraction differs slightly from this target. In Table 5.1 the number of fibers ( $N_f$ ) and real fiber volume fraction ( $V_f$ ) of the five different MVE sizes used in the convergence study is given.

$w \times h$ [ $\mu\text{m}$ ]	$N_f$ [-]	$V_f$ [%]
$12.5 \times 12.5$	1	50.3
$37.5 \times 37.5$	8	44.7
$50 \times 50$	15	47.1
$62.5 \times 62.5$	24	48.3
$75 \times 75$	35	48.9

**Table 5.1:** Real fiber volume fraction for the considered MVE sizes (Fiber radius:  $r = 5 \mu\text{m}$ )

Any convergence study inherently has a limited validity; e.g. a mesh that is converged for one set of material properties is not necessarily converged for a different combination. Ideally, the convergence study is repeated every time the input is altered. In practice (computational) resources often limit the number of performed convergence studies. The following input parameters are expected to have an effect on the RVE size:

- Combination of material properties
- Volume fraction
- Mode-mixity (load-cases)

The decision was made to limit the convergence study to three different load-cases, keeping all other parameters constant. This decision was motivated by the project goal (see: Chapter 1). The constituent fracture behavior is specified using bilinear Traction-Separation Laws, as was discussed in Chapter 3. The fracture behavior of the constituents is assumed to be mode independent. The matrix strength was taken as 50 MPa and a weak interface was assumed with half the matrix strength (25 MPa). The fiber (transverse) strength was taken as 100 MPa, which is high enough to exclude fiber fracture. Increasing the fiber strength further therefore does not alter the results. The failure opening was assumed the same for all materials at  $2.0 \mu\text{m}$ . The input cohesive constitutive behavior is included in Figure 5.3.

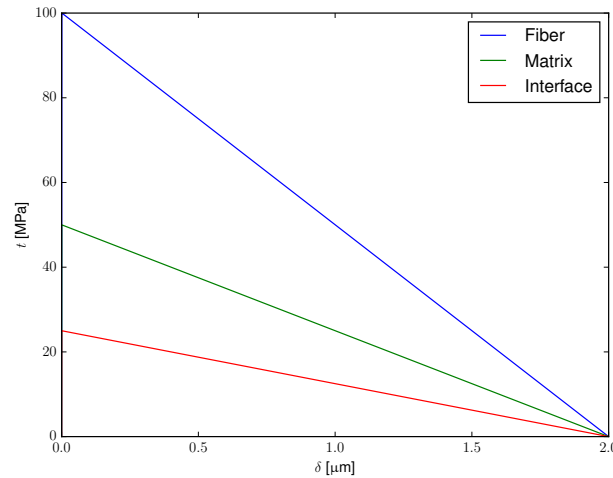


**Figure 5.3:** Cohesive material properties used in the convergence study

The applied deformations for the three convergence study load-cases are shown in Figure 5.4.

In the size convergence study, results of different sizes of MVEs are compared. In the proposed multiscale framework, the goal of the microscale analysis is to determine effective cohesive constitutive behavior in the form of an Effective Traction Separation Law (ETSL), that is to be used at the macroscopic scale. Convergence will therefore be checked by comparing ETSLs.

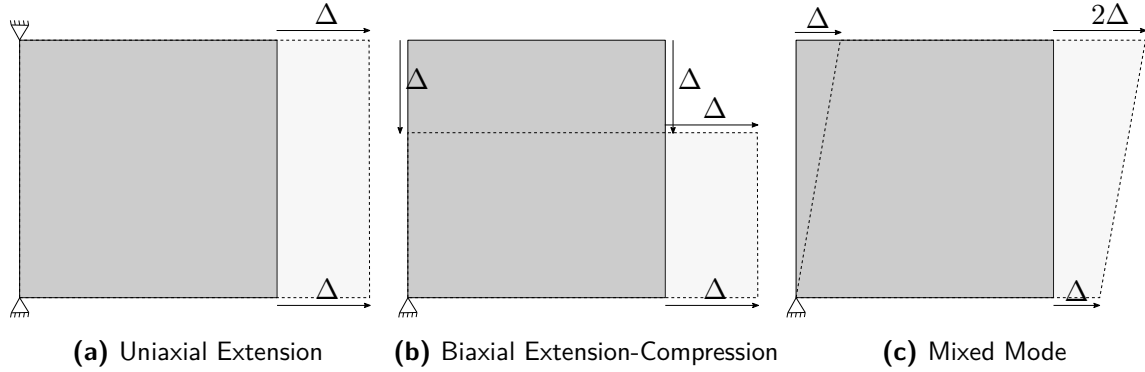


**Figure 5.4:** Deformations applied for the convergence study

The size convergence can only be studied when the results were obtained for converged meshes. Therefore a mesh convergence study is performed first for all MVE sizes and load cases. The results of the mesh convergence study are discussed in Section 5.1. The results of the size convergence study are given in Section 5.2.

## 5.1 Mesh Convergence

As mentioned before a mesh convergence study is performed for each of the considered MVE sizes and under three different loadings. The results of the mesh convergence study for the uniaxial extension load case (Figure 5.4a) are presented in Section 5.1.1, followed by the Biaxial Extension-Compression load case (Figure 5.4b) in Section 5.1.2. The section is concluded with the mesh convergence study for the mixed mode load case (Figure 5.4c).

Four mesh densities were considered for the unit cell, with the coarsest grid size of  $2\ \mu\text{m}$  halved three subsequent times to arrive at the finest  $0.25\ \mu\text{m}$  mesh. The grid size refers to the target node spacing used during the meshing of the MVE (see: Section 4.1.3). The mesh refinement was done by complete re-meshing, rather than splitting/bisecting original elements, to minimize mesh-dependent behavior. The unit cell meshes are shown in Figure 5.5.

The  $37.5 \times 37.5\ \mu\text{m}$  MVE is meshed using three grid sizes, equal to the node spacing used for the unit cell. Computational cost excluded the  $0.25\ \mu\text{m}$  grid size. Since in principal three data points are sufficient to check (rate of) convergence, this should not pose any problems. The  $50 \times 50\ \mu\text{m}$  MVE was meshed using the same target node spacings used for the  $37.5 \times 37.5\ \mu\text{m}$  MVE. The three mesh sizes applied to a single  $50 \times 50\ \mu\text{m}$  realization are shown in Figure 5.6.

For the  $62.5 \times 62.5\ \mu\text{m}$  MVE the computational cost excluded the finest ( $0.5\ \mu\text{m}$ ) node spacing used on the  $50 \times 50\ \mu\text{m}$  MVE. To obtain a third mesh density for the study the decision was

made to use  $3\ \mu\text{m}$ , rather than doubling the  $2\ \mu\text{m}$  grid size. The  $75 \times 75\ \mu\text{m}$  MVE is meshed using the same node spacing as the  $62.5 \times 62.5\ \mu\text{m}$  MVE;  $3\ \mu\text{m}$ ,  $2\ \mu\text{m}$  and  $1\ \mu\text{m}$ . The  $3\ \mu\text{m}$  mesh can still reasonably approximate the circular ( $5\ \mu\text{m}$  radius) shape of the inclusions, as can be seen in Figure 5.7a. The  $2\ \mu\text{m}$  and  $1\ \mu\text{m}$  node spacings are shown in Figure 5.7b and Figure 5.7c respectively.

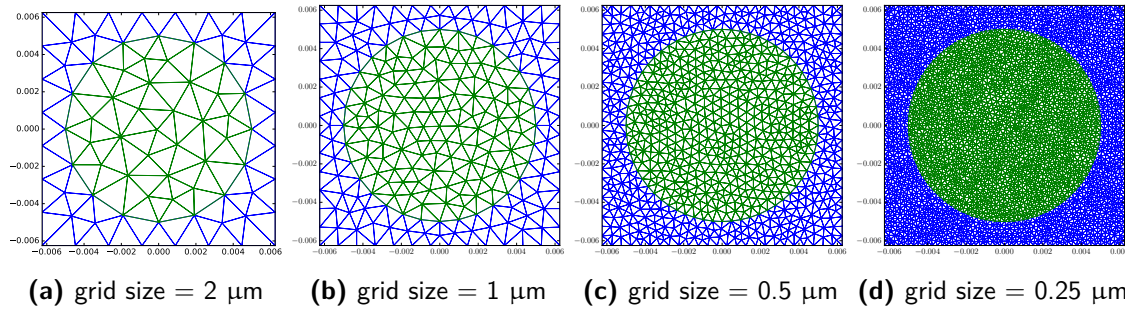


Figure 5.5:  $12.5 \times 12.5\ \mu\text{m}$  (Unit cell)

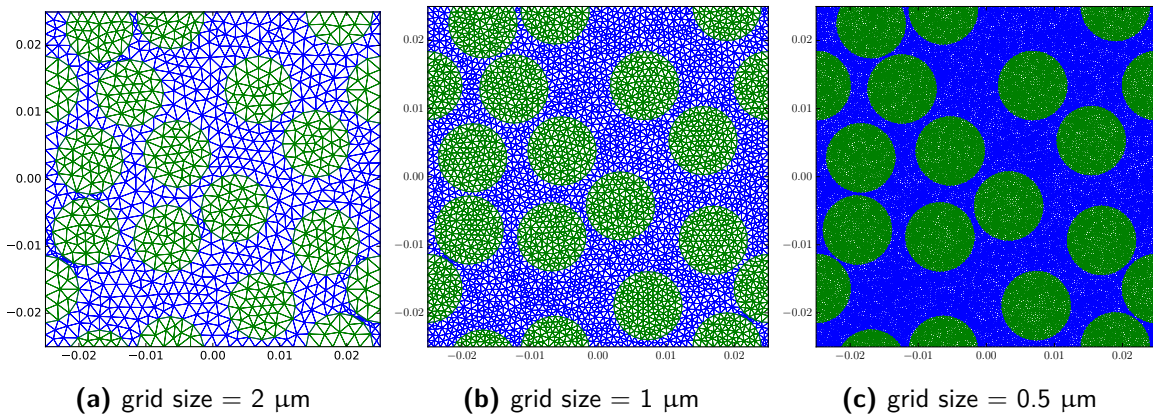


Figure 5.6:  $50 \times 50\ \mu\text{m}$

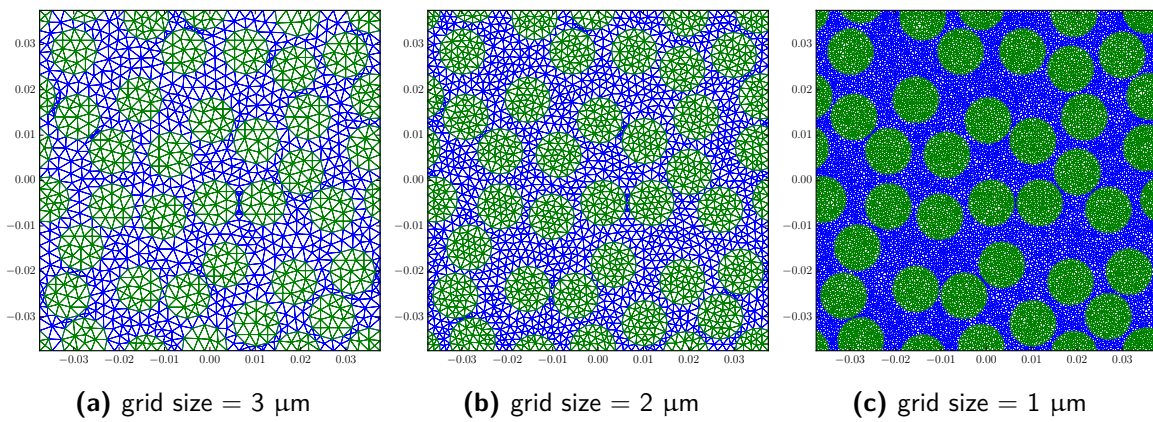
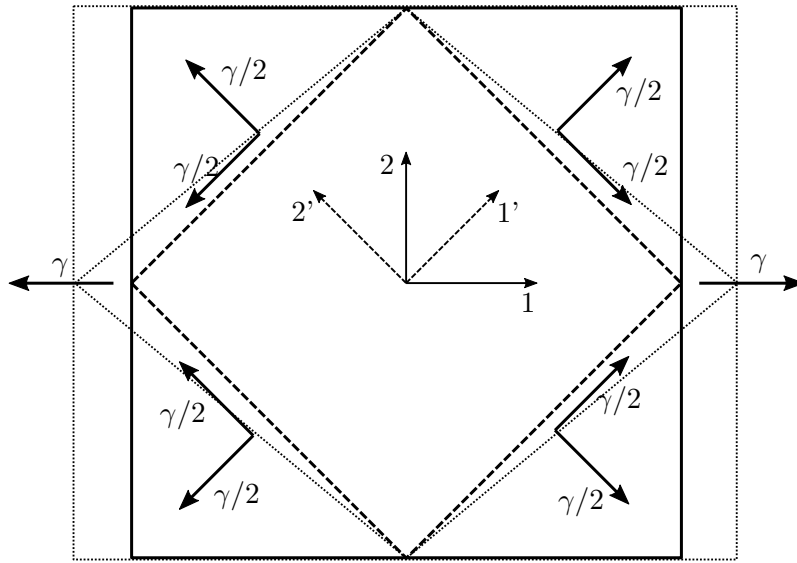


Figure 5.7:  $75 \times 75\ \mu\text{m}$

### 5.1.1 Uniaxial Extension

The uniaxial extension load case was shown schematically in Figure 5.4a. The principal strain is in the global 1-direction, i.e. equal to the only non-zero strain tensor term  $\epsilon_{11}$ . The Poisson contraction of the transversely isotropic material is restricted resulting in biaxial tension in the MVE, with the maximum tensile stress in the principal strain direction.



**Figure 5.8:** Uniaxial Extension

Under the applied deformation a vertical crack is expected. In Figure 5.9 the deformation at the final state of the simulation is shown for the unit cell. The maximum in-plane principal stress is included in the plots.

It can be seen that localization occurs left of center for the 2  $\mu\text{m}$  (Figure 5.9b) and 0.5  $\mu\text{m}$  (Figure 5.9c) meshes and right of center for the 1  $\mu\text{m}$  (Figure 5.9a) and 0.25  $\mu\text{m}$  (Figure 5.9d) meshes. The symmetric geometry and the absence of flaws result in a system that in should have no preference regarding the side at which localization occurs under this loading, leaving the mesh as the only factor influencing the location of the crack. The results in Figure 5.9, therefore, show the effect of the mesh on the crack geometry. Comparing the two finest meshes it can be concluded that, although mirrored with respect to the  $y$ -axis, the shape of the crack converges.

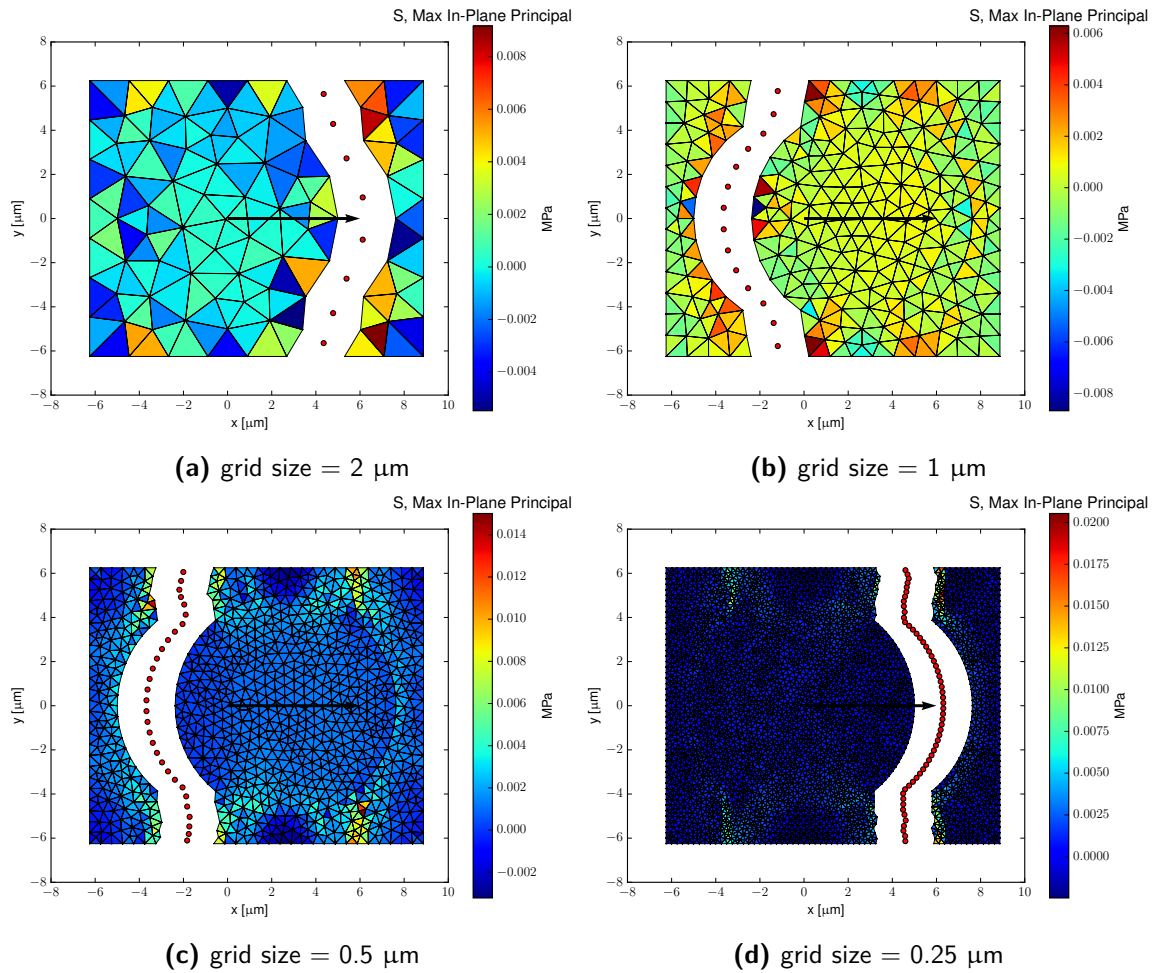


**Figure 5.9:** Mesh Convergence: Deformation (Uniaxial Extension, Unit Cell:  $12.5 \times 12.5 \mu\text{m}$ )

The ETSL in mode I and II are included in Figure 5.10. The uniaxial extension applied to the unit cell results in pure mode I opening, for which the ETSL is given in Figure 5.10a. The mode II ETSL shown in Figure 5.10b has no real value, with the tangential opening below 2 picometer. Focusing on the mode I ETSL it can be concluded that the cohesive constitutive behavior converges for a mesh size of  $0.5 \mu\text{m}$ . With a converged effective ultimate strength of 39 MPa and a failure opening of  $2.0 \mu\text{m}$ , the ETSL is in-between the matrix and interface behavior.

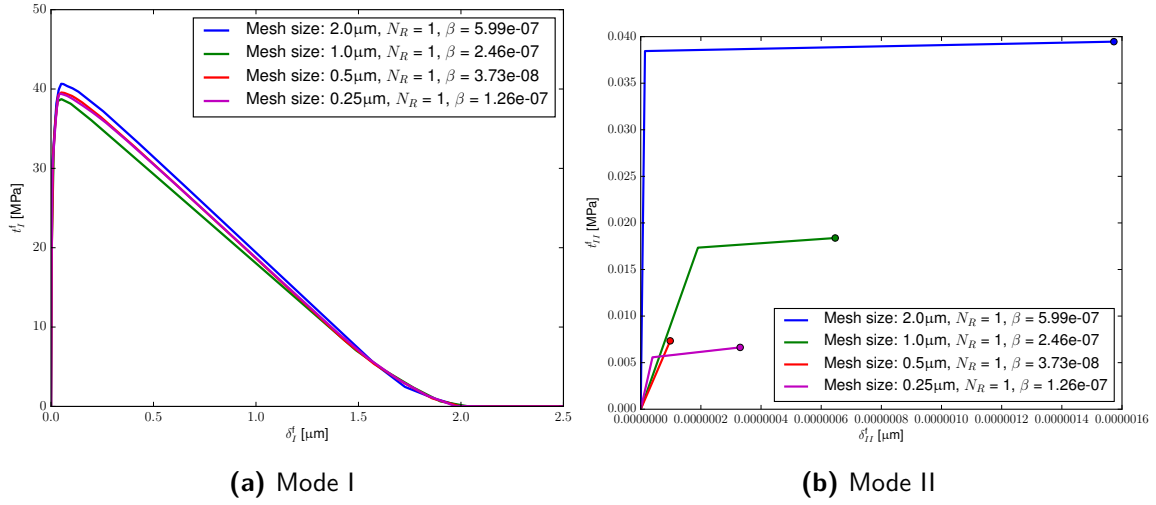


**Figure 5.10:** Mesh Convergence: ETSL (Uniaxial Extension, Unit Cell:  $12.5 \times 12.5 \mu\text{m}$ )

Figure 5.11 illustrates the mesh convergence of crack properties. Note that the  $x$ -axis values are absolute mesh sizes and therefore increase from fine to coarse. Both the crack length (Figure 5.11a), as well as the material content (Figure 5.11b) converge for a mesh size of  $0.5 \mu\text{m}$ , equal to the value observed for the ETSL.

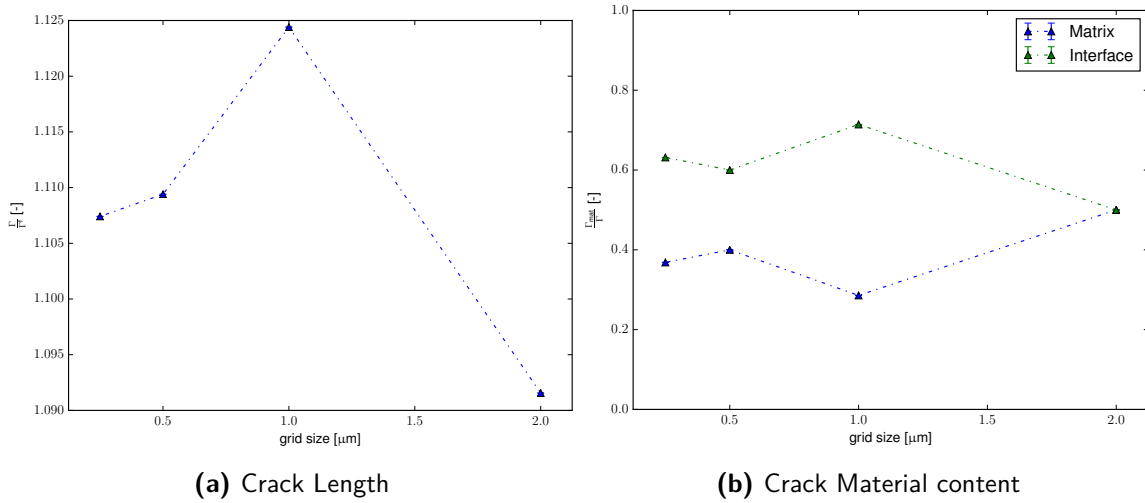


**Figure 5.11:** Mesh Convergence: Crack Configuration (Uniaxial Extension, Unit Cell:  $12.5 \times 12.5 \mu\text{m}$ )

Three mesh sizes were investigated for the  $37.5 \times 37.5$  MVE as discussed at the beginning of this section. For each of those mesh sizes, five different realizations were analyzed to obtain a measure for the spread. Figure 5.13a presents the average mode I ETSL for each mesh size. The average ETSL is obtained by combining the results of all five realizations of the same mesh density. For the finest mesh, the  $1\sigma$ -bounds (standard deviation) are included by shading. The thin portion of the ETSL indicates where the viscous automatic stabilization energy (see: Section 4.2) of at least one realization exceeded 5% of the total strain energy,

which adversely effects the accuracy of the simulation.

The viscous automatic stabilization helps the simulation to converge. Viscosity adds rate dependent traction to limit the opening rate and increase the stable time step, as was mentioned in Section 4.2. The last part of the ETSL includes the added rate-dependent traction as shown in Figure 5.12. This section of the curve is thus less reliable and should not be given as much weight in determining convergence of the fracture behavior.

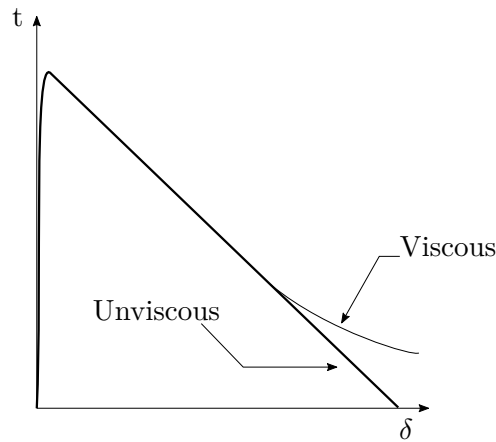
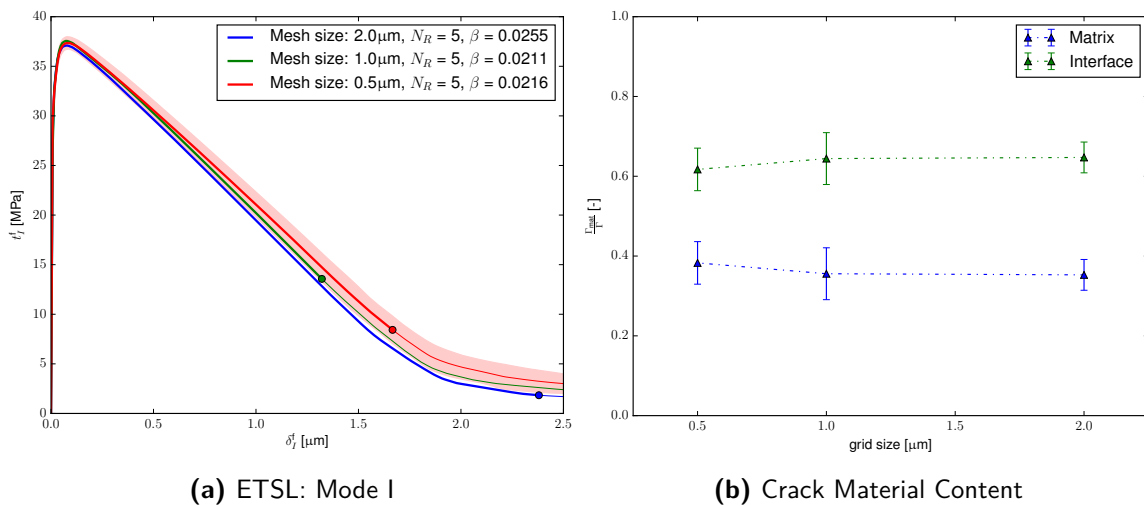


Figure 5.12: The effect of viscous stresses on the ETSL

Examining Figure 5.13a and Figure 5.13b it can be concluded that the a mesh size of 1  $\mu\text{m}$  is sufficiently small for the  $37.5 \times 37.5 \mu\text{m}$  MVE.



(a) ETSL: Mode I

(b) Crack Material Content

Figure 5.13: Mesh Convergence: Uniaxial Extension,  $37.5 \times 37.5 \mu\text{m}$

The mode I ETSL and the material composition of the crack for three different mesh densities applied to the  $50 \times 50 \mu\text{m}$  MVE is included in Figure 5.14. As can be seen in Figure 5.14a, the effective fracture behavior converges for a mesh density of 1  $\mu\text{m}$ , i.e. the same as for the

smaller  $37.5 \times 37.5 \mu\text{m}$  MVE. The material composition of the crack also converges for a mesh density of  $1 \mu\text{m}$ .

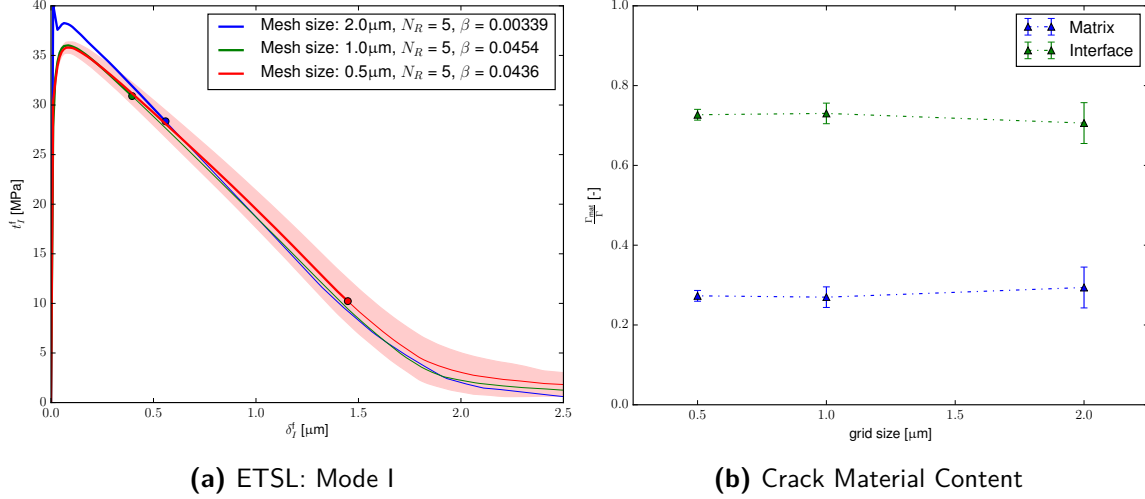


**Figure 5.14:** Mesh Convergence: Uniaxial Extension,  $50 \times 50 \mu\text{m}$

The uniaxial extension mesh convergence study of the  $62.5 \times 62.5 \mu\text{m}$  MVE is included in Figure 5.15. The finest mesh size that was considered for this MVE size is  $1 \mu\text{m}$ . The mode I ETSL converges for a mesh size of  $2 \mu\text{m}$ . The material composition of the crack is equal for the coarser meshes, but significantly changes for the finest mesh size. Examination of the deformation results showed that one of the realizations of the  $1 \mu\text{m}$  simulations had extensive crack branching along the interface on both sides of the same fiber. The type of branching has an impact on the material composition, but not on the effective fracture behavior. The effective fracture behavior of the  $62.5 \times 62.5 \mu\text{m}$  MVE converges for a mesh size of  $2 \mu\text{m}$ .

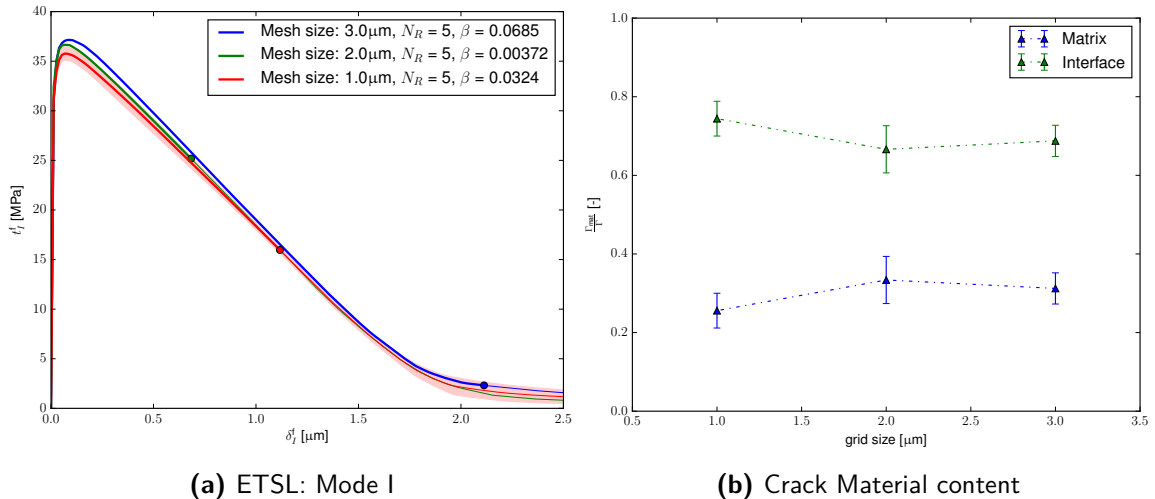


**Figure 5.15:** Mesh Convergence: Uniaxial Extension,  $62.5 \times 62.5 \mu\text{m}$

The mesh convergence study for the largest of the considered MVE sizes is shown in Fig-

ure 5.16. Both the mode I ETSL, as well as the material composition of the crack, converge for a mesh size of 2  $\mu\text{m}$ .

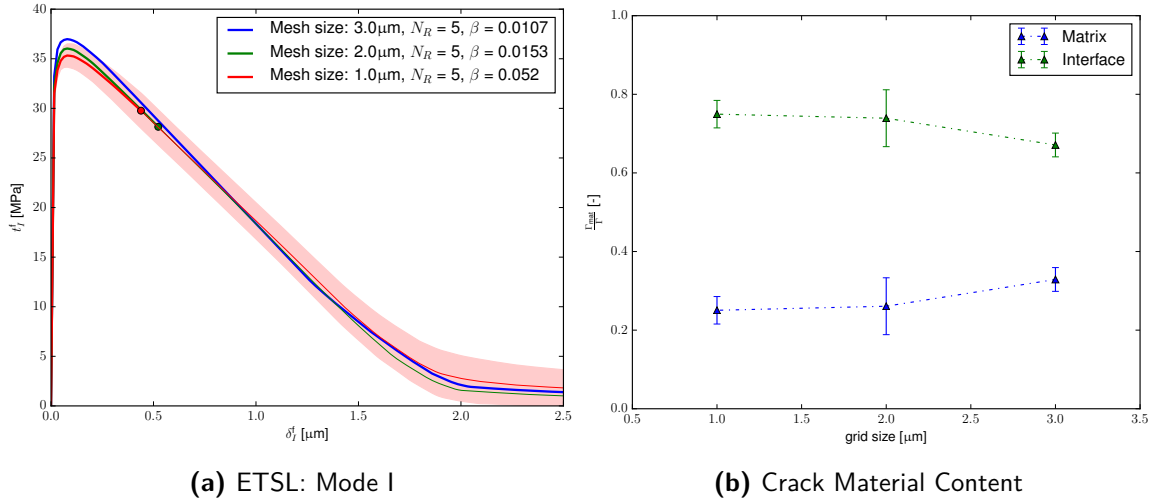


Figure 5.16: Mesh Convergence: Uniaxial Extension, 75  $\times$  75  $\mu\text{m}$

5.1.2 Biaxial Extension-Compression

The biaxial extension-compression was shown schematically in Figure 5.4b. The principal strain directions are aligned with the global coordinate system. The applied deformation is a pure shear deformation under 45° as shown in Figure 5.17. The principal stresses are directed along the principal strain direction, with tension in the 1-direction and compression in the 2-direction. The maximum shear stress occurs under  $\pm 45^\circ$ .

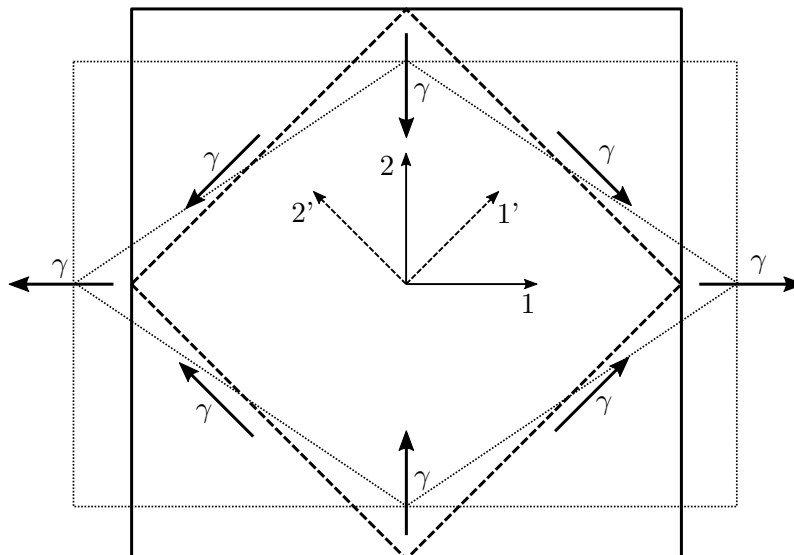
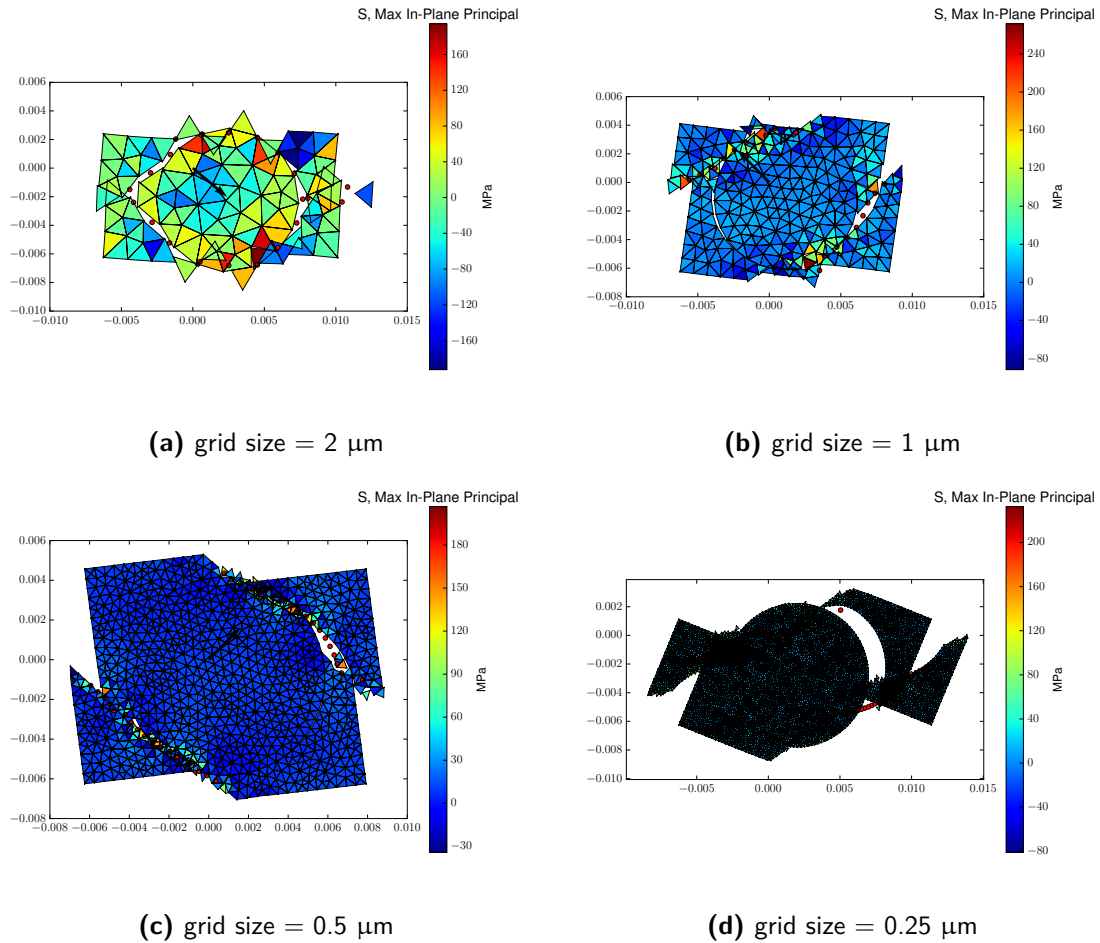


Figure 5.17: Biaxial Extension-Compression

The deformation at the last frame of the fracture simulation for the unit cell for all four

considered mesh sizes is shown in Figure 5.18. With the exception of the coarsest mesh (Figure 5.18a), the unit cell fails in the shear mode, with pure mode II opening. Sliding over a rough and curved crack surface results in high compressive stresses, up to 260 MPa as shown in Figure 5.18b. Since the shear stress in  $\pm 45^\circ$  is equal, mode II fracture occurs along both directions.



**Figure 5.18:** Mesh Convergence: Deformation (Biaxial Extension-Compression, Unit Cell:  $12.5 \times 12.5 \mu\text{m}$ )

The mode I and mode II ETSLs of the unit cell loaded with biaxial extension-compression are shown in Figure 5.19. The unit cell with the coarsest mesh, included in Figure 5.18a, fractures partially in mode I. The mode I ETSL of this simulation is the the only one with substantial positive traction as can be seen in Figure 5.19a. The mesh convergence for this load case is done based upon the mode II fracture behavior shown in Figure 5.19b. The mode II ETSL for the unit cell under biaxial extension-compression converges for a mesh size of 0.5  $\mu\text{m}$ , which is the same for the uniaxial extension load case.

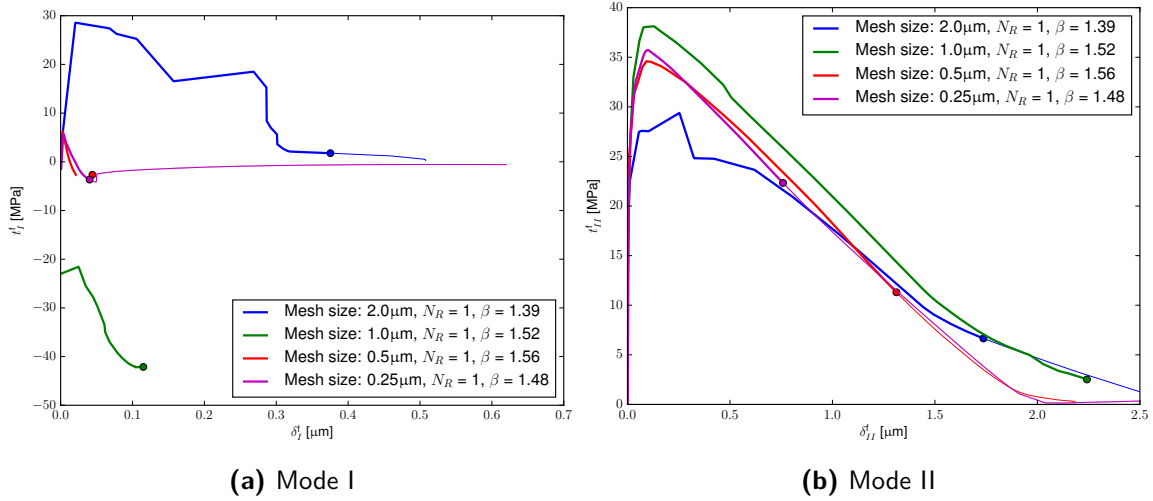


**Figure 5.19:** Mesh Convergence: ETSL (Biaxial Extension-Compression, Unit Cell:  $12.5 \times 12.5 \mu\text{m}$ )

The crack configuration of the unit cell is studied in Figure 5.20. The fraction of the microscopic to the effective macroscopic crack length is shown in Figure 5.20a. For the  $1 \mu\text{m}$  mesh density the fraction is below one, which is an impossibility. The simulation was aborted due to convergence issues before the load step was completed and not all cohesive elements along the crack path failed (see: Figure 5.18b). The micro-macro crack length fraction converges for a grid size of  $0.5 \mu\text{m}$ . The material composition of the crack is shown in Figure 5.20b. The material content of the crack has also converged for a mesh density of  $0.5 \mu\text{m}$ .

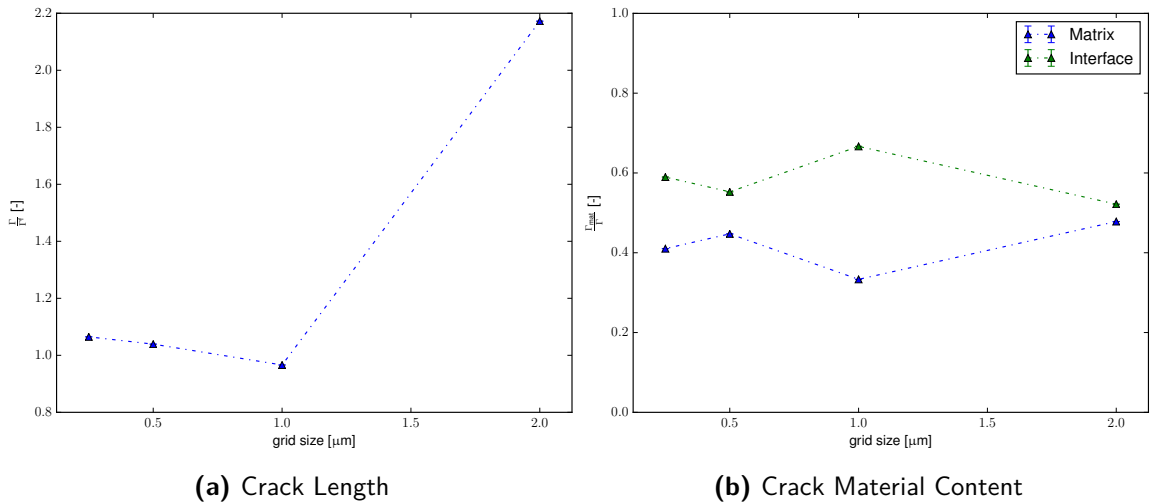


**Figure 5.20:** Mesh Convergence: Crack Configuration (Biaxial Extension-Compression, Unit cell:  $12.5 \times 12.5 \mu\text{m}$ )

The mode II ETSL and the the material composition of the  $37.5 \times 37.5 \mu\text{m}$  MVE loaded under biaxial extension-compression is shown in Figure 5.21. The simulation with the finest mesh ( $0.5 \mu\text{m}$ ) considered for this MVE size was unable to complete the load step. Mesh

convergence can, therefore, not be established. The crack contains, unlike the results of the unit cell, more matrix than interface.

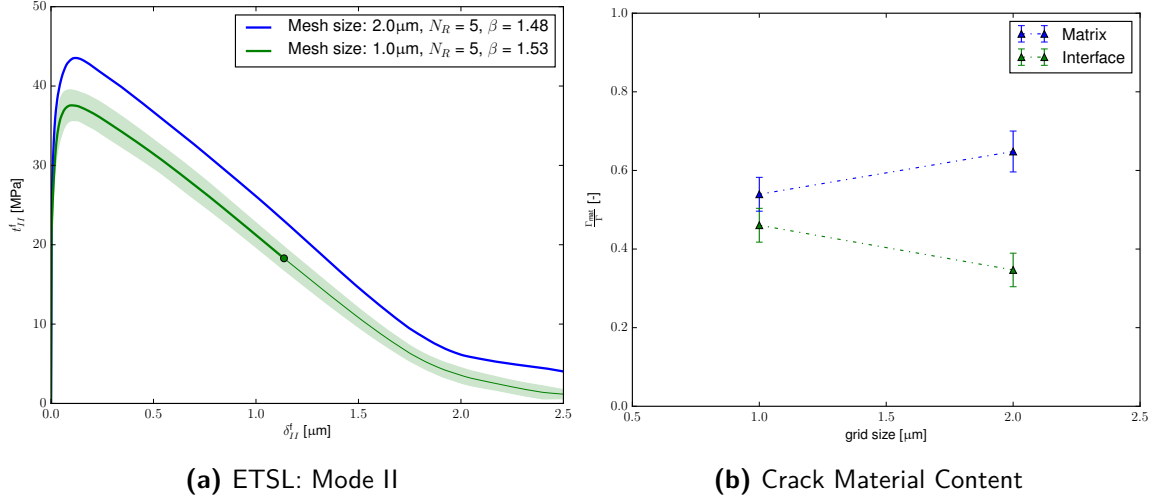


**Figure 5.21:** Mesh Convergence: Biaxial Extension-Compression,  $37.5 \times 37.5 \mu\text{m}$

The mesh convergence study of the  $50 \times 50$  MVE is also limited to just two mesh densities. The simulations using the finest mesh size of  $0.5 \mu\text{m}$  were not able to fully fail the MVE and were aborted when the stable time step was lower than the floating point accuracy. The mode II ETSL shown in Figure 5.22a shows the ultimate strength converged within the standard deviation.

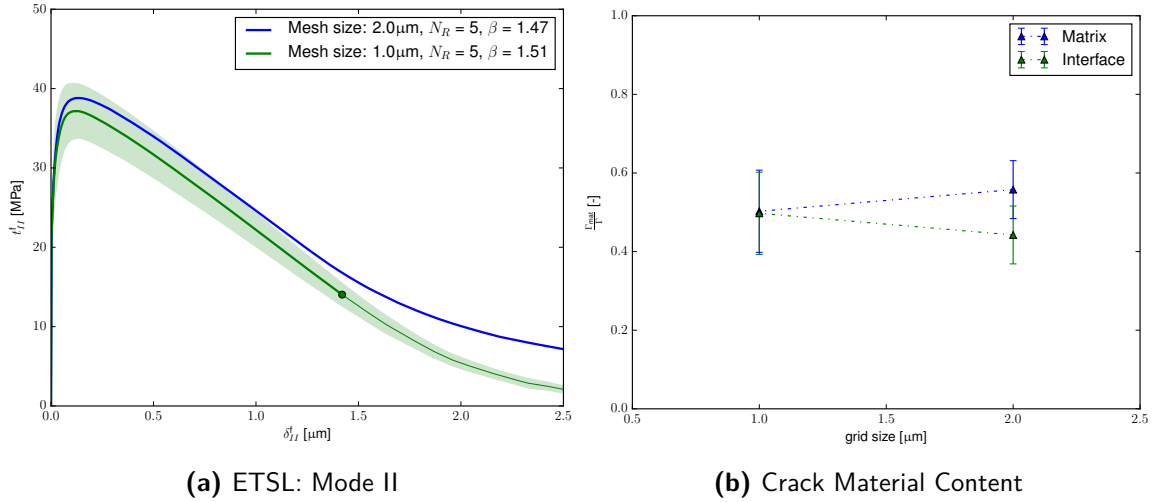


**Figure 5.22:** Mesh Convergence: Biaxial Extension-Compression,  $50 \times 50 \mu\text{m}$

For the  $62.5 \times 62.5 \mu\text{m}$  MVE, the finest mesh size considered was  $1 \mu\text{m}$ . The simulations with this mesh size were, however, not able to complete the load step. It is not possible to determine whether the mode II ETSL has converged for this MVE size by examination of Figure 5.23.

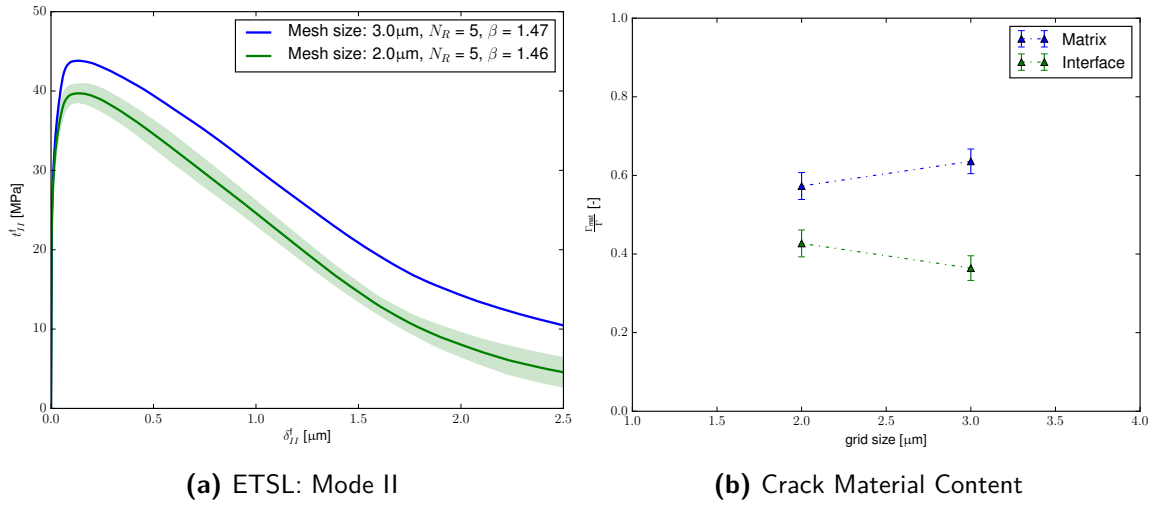


**Figure 5.23:** Mesh Convergence: Biaxial Extension-Compression,  $62.5 \times 62.5 \mu\text{m}$

The mesh convergence of the  $75 \times 75$  MVE is shown in Figure 5.24. Unfortunately the finest mesh size of  $1 \mu\text{m}$  did not complete the fracture simulation, as in the case of the  $62.5 \times 62.5$  MVE. The material content of the crack is stable at around 45% interface and 55% matrix. It is not possible to determine whether the mode II ETSL has converged for the  $2 \mu\text{m}$  mesh density.

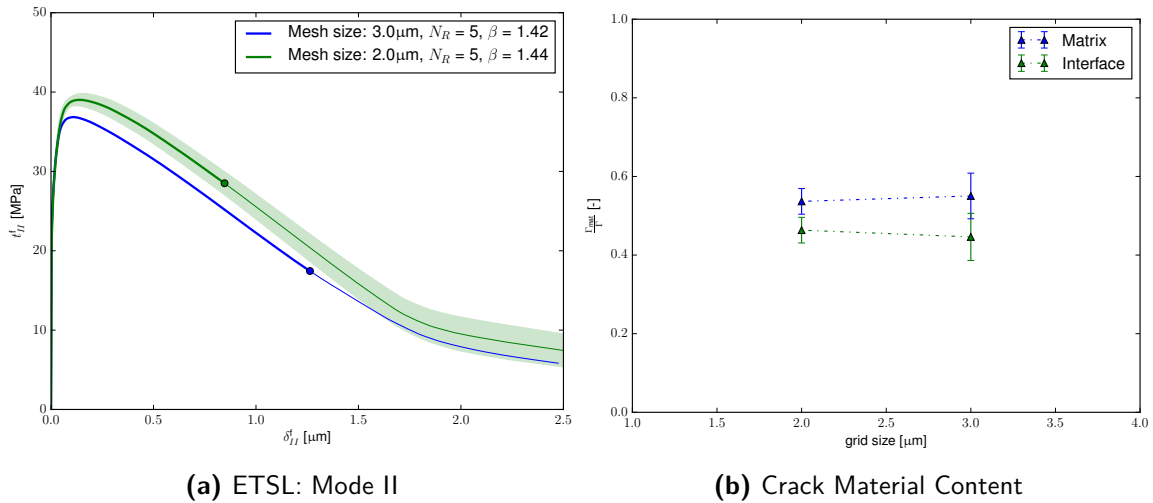


**Figure 5.24:** Mesh Convergence: Biaxial Extension-Compression,  $75 \times 75 \mu\text{m}$

For all the MVEs, with the exception of the unit cell, the mesh convergence study of the fracture behavior was limited to two mesh sizes. The biaxial extension-compression simulations turned out to be incredibly challenging. The mesh-dependency of the cohesive zone method with embedded cohesive elements makes it not very well suited to simulate pure mode II fracture, since it can never produce a smooth sliding surface. For the size convergence study the finest possible mesh size will be used.

### 5.1.3 Mixed Mode

The mixed load case is a combination of uniaxial extension and simple shear, as shown in Figure 5.4c. The load case was designed to produce mixed mode fracture, with substantial opening and traction in both crack opening modes. The deformation at the final state of the simulation for the unit cell is shown in Figure 5.25. Comparing Figure 5.25c and Figure 5.25d it can be concluded that the crack geometry converges for a mesh size of  $0.5 \mu\text{m}$ .

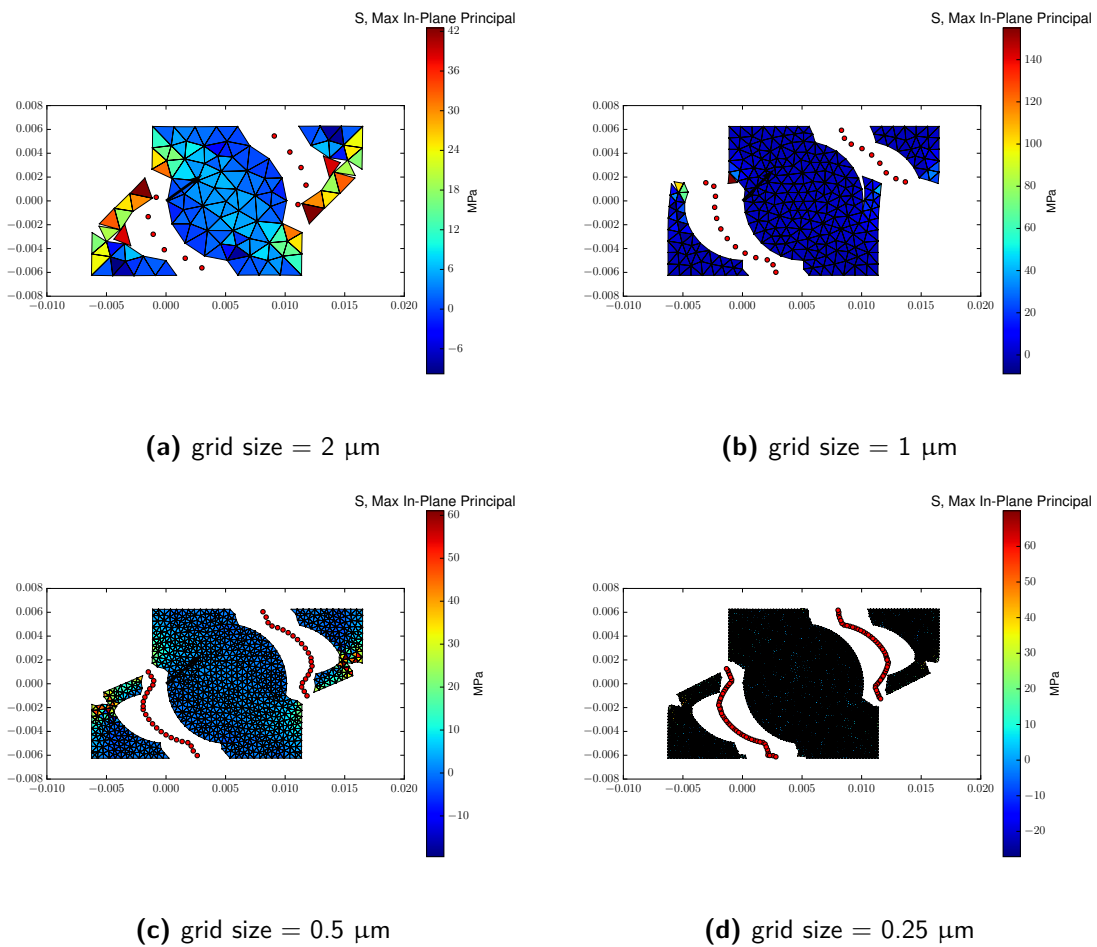


**Figure 5.25:** Mesh Convergence: Deformation (Mixed, Unit Cell:  $12.5 \times 12.5 \mu\text{m}$ )

The ETSLs in both modes are included in Figure 5.26. The mode I ETSL converges for a mesh density of  $0.5 \mu\text{m}$  as can be seen in Figure 5.26a. The mode II ETSLs of the two finest mesh sizes are not so close together. The initial fracture occurs in mode I, as evidenced by the height of the traction peak. The mode I ETSL was, therefore, given more importance in determining convergence.

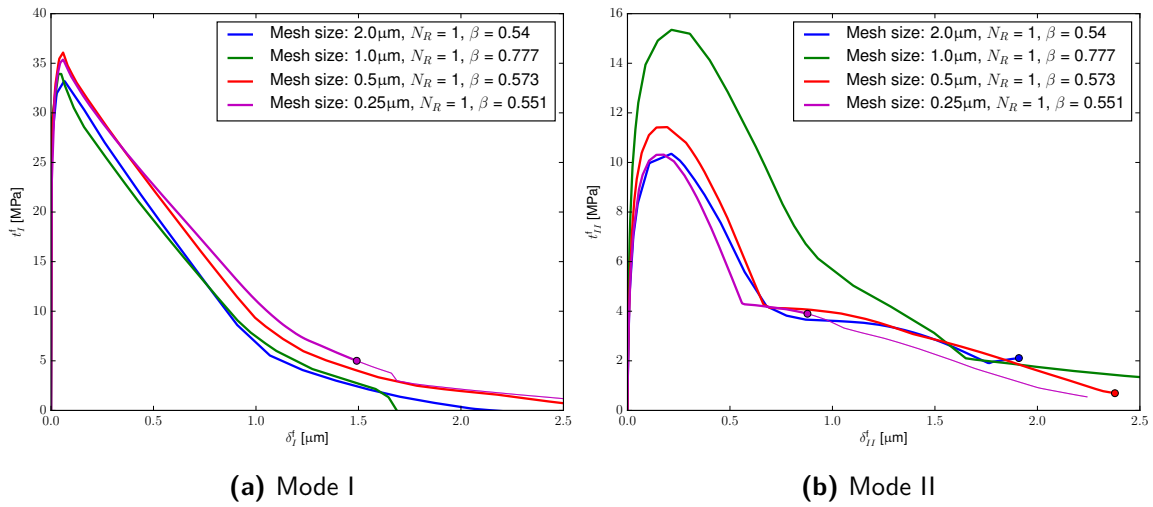


Figure 5.26: Mesh Convergence: ETSL (Mixed, Unit Cell:  $12.5 \times 12.5 \mu\text{m}$ )

Analysis of the crack configuration supports the mesh convergence at  $0.5 \mu\text{m}$ . The ratio of the microscopic to effective macroscopic crack length already converged for a mesh size of  $1 \mu\text{m}$ . The material composition of the crack converges for  $0.5 \mu\text{m}$  to approximately 75% interface and 25% matrix.

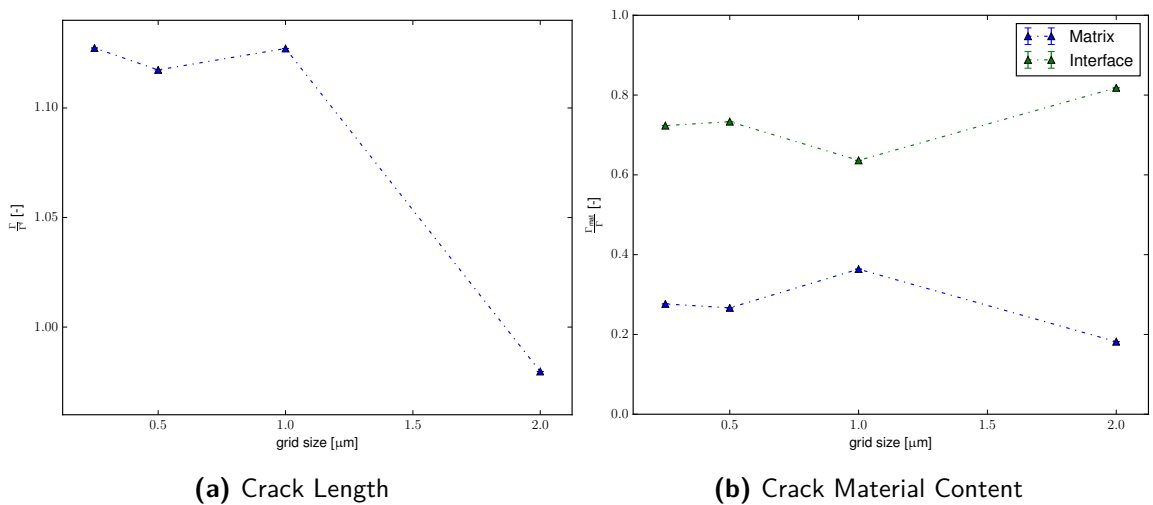
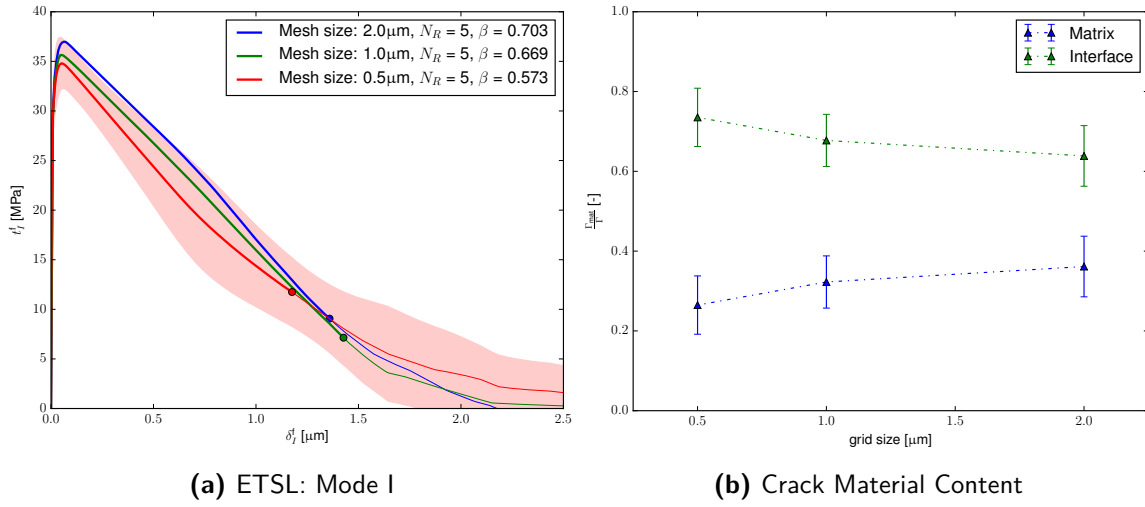


Figure 5.27: Mesh Convergence: Crack Configuration (Mixed, Unit cell:  $12.5 \times 12.5 \mu\text{m}$ )

The mesh convergence study of the  $37.5 \times 37.5 \mu\text{m}$  MVE is included in Figure 5.28. The mode I ETSL converges within the standard deviation for a mesh size of  $1 \mu\text{m}$ , which is the same size as was found for the uniaxial extension load case. The material content of the crack is similar for the two coarsest mesh sizes. The finest mesh size, however, was found to have significantly more cracking along the interface. Examination of the results showed that two realizations of the finest mesh density had isolated interface crack segments that were not part of the main crack. The fracture behavior of the  $37.5 \times 37.5 \mu\text{m}$  MVE converged for a mesh density of  $1 \mu\text{m}$ .



**Figure 5.28:** Mesh Convergence: Mixed,  $37.5 \times 37.5 \mu\text{m}$

For the  $50 \times 50 \mu\text{m}$  MVE the mode I fracture converges perfectly for the  $1 \mu\text{m}$  mesh density, as shown in Figure 5.29a. The mode I ETSL belonging to the coarsest mesh also converged within the standard deviation of the finest mesh simulations, which is relatively large. The material composition of the crack is stable at approximately 75% interface and 25% matrix.

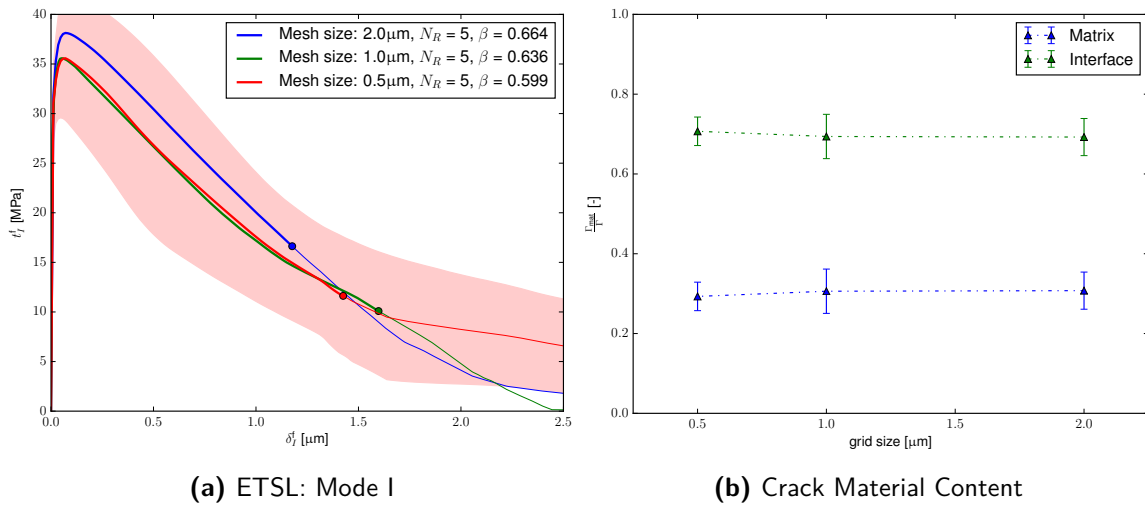


**Figure 5.29:** Mesh Convergence: Mixed,  $50 \times 50 \mu\text{m}$

The mesh convergence for the second largest MVE is shown in Figure 5.30a. The mode I ETSL, included in Figure 5.30a, already converged for the coarsest mesh size of  $3 \mu\text{m}$ . The material content of the crack is also relatively stable for the three different mesh sizes.

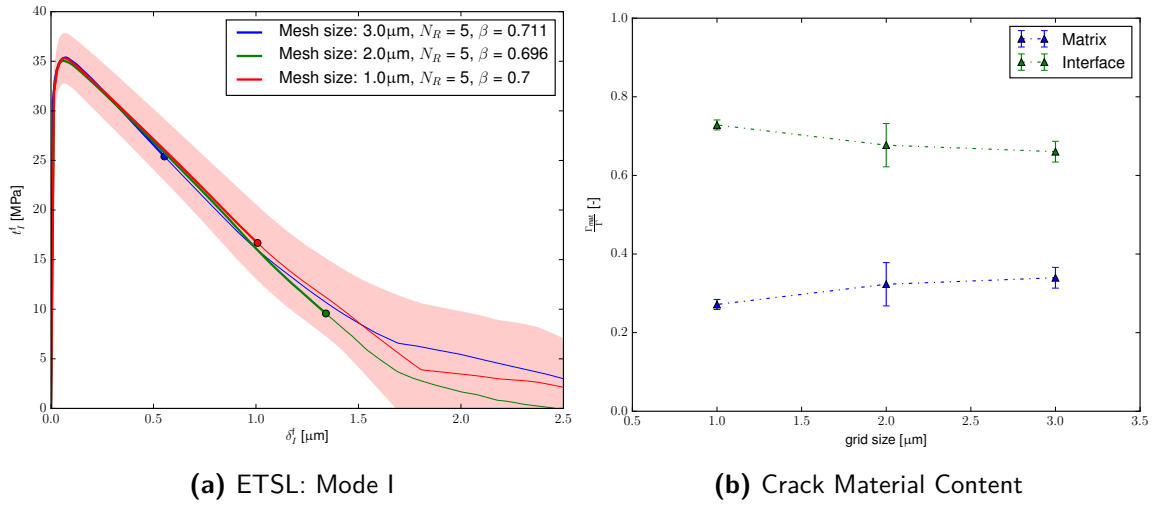


Figure 5.30: Mesh Convergence: Mixed,  $62.5 \times 62.5 \mu\text{m}$

For the largest MVE the mixed mode fracture converges for a mesh size of  $2 \mu\text{m}$ . The mode I ETSLs of the three considered mesh densities are shown in Figure 5.31a. The ETSLs of the two finest meshes are on top of each other up to the viscous portion of the simulation. The material composition of the crack differs significantly for the finest mesh. This is caused by crack branching and isolated crack segments in two of the five realizations.

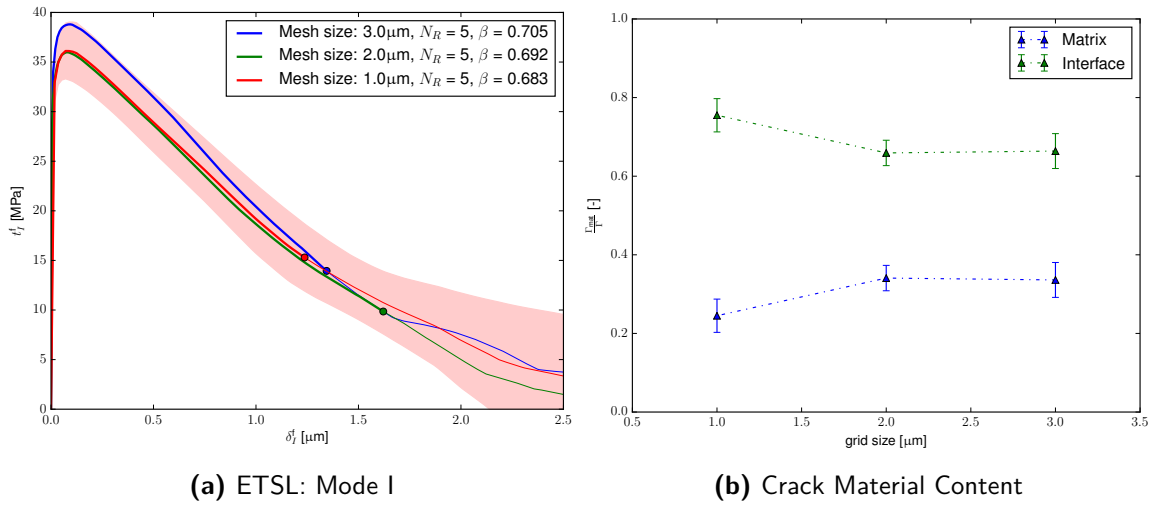


Figure 5.31: Mesh Convergence: Mixed,  $75 \times 75 \mu\text{m}$

## 5.2 Micro-structural Volume Element size: RVE

In the previous section the converged mesh was established for 5 different sizes of MVEs under 3 different external loads. The results of converged meshes will be compared to establish the RVE size. The RVE size is determined per load case and the largest of the three is adopted as the overall RVE. First the results of the uniaxial extension load case will be discussed in

Section 5.2.1, followed by the biaxial extension-compression load case in Section 5.2.2. Finally the RVE convergence study of the mixed load case is included in Section 5.2.3.

### 5.2.1 Uniaxial Extension

The uniaxial extension load case (see: Figure 5.4a) resulted in pure mode I cracking ( $\beta \approx 0$ ) in all simulations. The converged mesh size for this load case was established in Section 5.1.1 for all considered MVE sizes. The mode I ETSLs for the converged meshes are included in Figure 5.32.

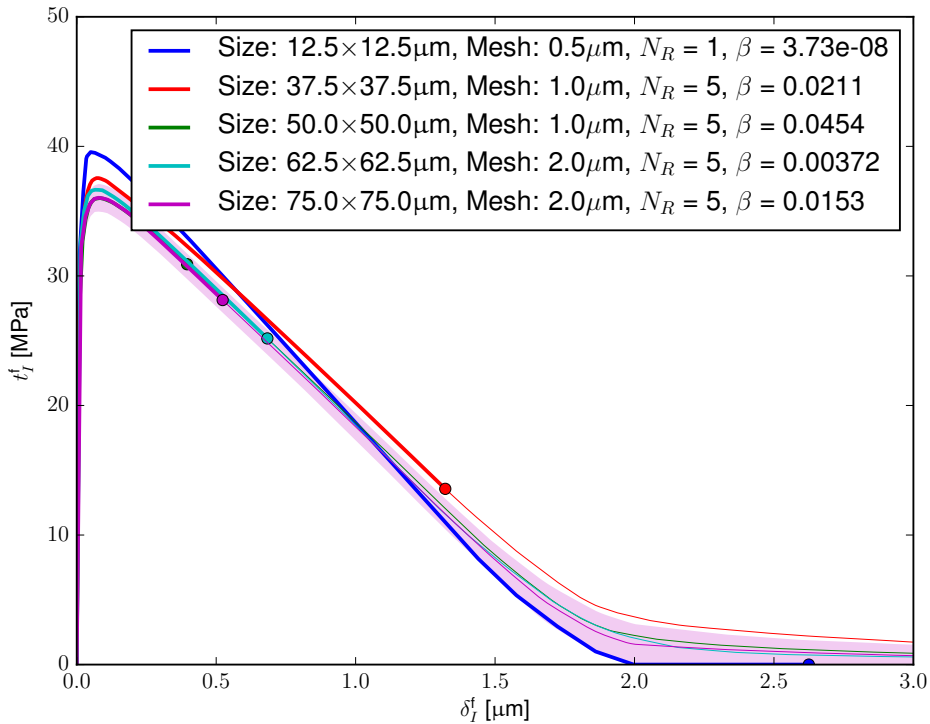


**Figure 5.32:** RVE convergence: ETSL Mode I, Uniaxial Extension

The mode I effective fracture behavior converges for an MVE size of  $50 \times 50 \mu\text{m}$ , which lies underneath the curves belonging to the  $62.5 \times 62.5$  and  $75 \times 75 \mu\text{m}$  ETSL for most of the fracture process. Interestingly, the ETSL of the  $12.5 \times 12.5 \mu\text{m}$  unit cell is not far off from the converged fracture behavior.

The convergence of the crack length and material composition is included in Figure 5.33. The fraction of the interface, which is the weaker than both the fiber and the matrix, increases for larger MVE sizes. The larger the MVE size, the more potential high-interface-content crack paths will exist. As a result the interface fraction increases from approximately 60% for the unit cell to 75% for the largest MVE.

A relation between the interface fraction and the ultimate strength can be identified, by comparing Figure 5.32 and Figure 5.33. The unit cell, which has the lowest interface fraction is the strongest, whereas the  $75 \times 75 \mu\text{m}$  has the highest interface fraction and the lowest

ultimate strength. For an interface that is stronger than or equal to the matrix, the RVE size is expected to be smaller. The volume fraction is also expected to have an influence on the RVE size for mode I fracture.

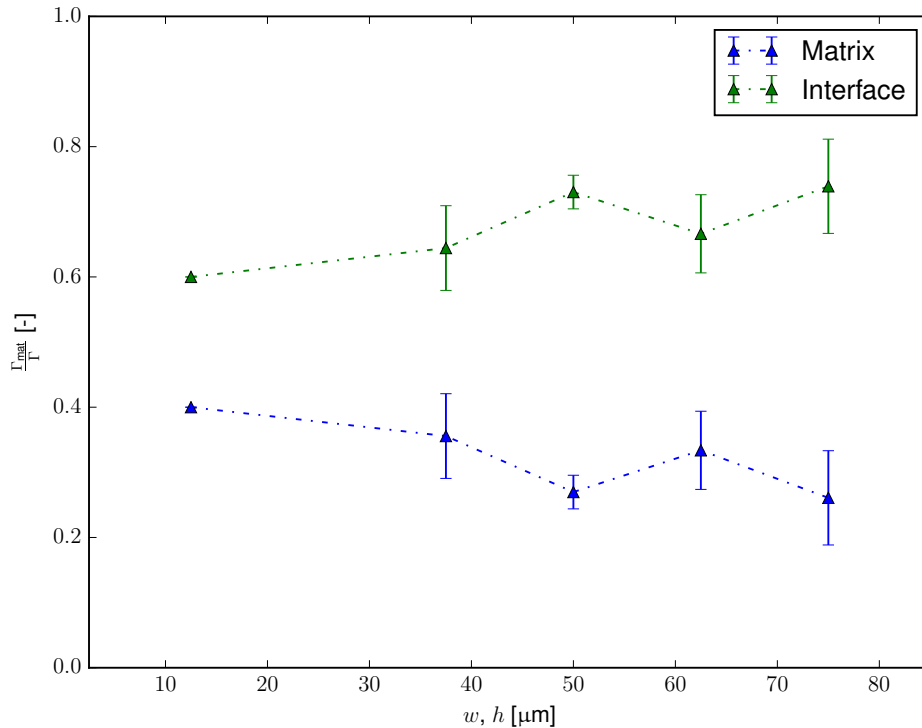


**Figure 5.33:** RVE Convergence: Crack Material Content, Uniaxial Extension

## 5.2.2 Biaxial Extension-Compression

The biaxial extension-compression load case (see: Figure 5.4b) resulted in pure mode II cracking ( $\beta \approx \pi/2$ ) for almost all simulations, the exception being the unit cell with the coarsest mesh density (see: Figure 5.18a). The mode II ETSLs for the considered MVE sizes are included in Figure 5.34. The material composition of the crack is included in Figure 5.35.

The convergence of the ETSL is not as clear as for the mode I crack. When the crack opens in mode II, the two crack surfaces slide over each-other. The sliding mechanism needs a crack surface that is as flat as possible. Since the crack has to follow element boundaries, it is impossible to obtain a completely smooth surface. The presence of the stronger fibers add an extra layer of difficulty for forming a flat crack surface.

The material composition of the crack oscillates around a 50-50% distribution. Judging by Figure 5.34 the crack material seems to have converged for the largest MVE size. The ETSL also seems to have settled with the  $62.5 \times 62.5 \mu\text{m}$  curve within the standard deviation of the  $75 \times 75 \mu\text{m}$  MVE. The RVE size for mode II cracking is  $75 \times 75 \mu\text{m}$ .

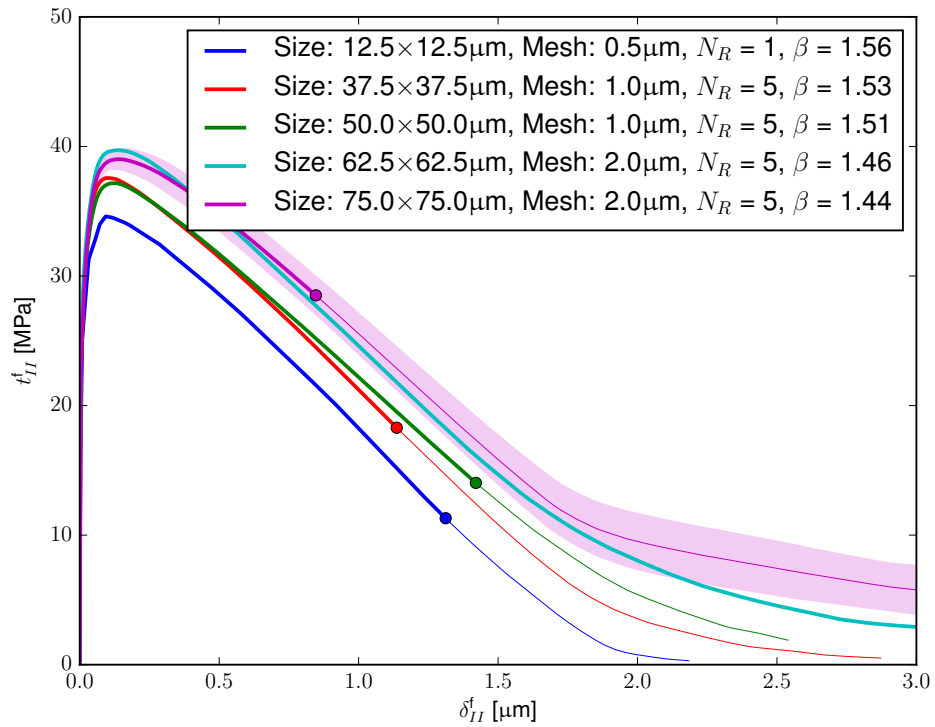


Figure 5.34: RVE Convergence: ETSL Mode II, Biaxial Extension-Compression

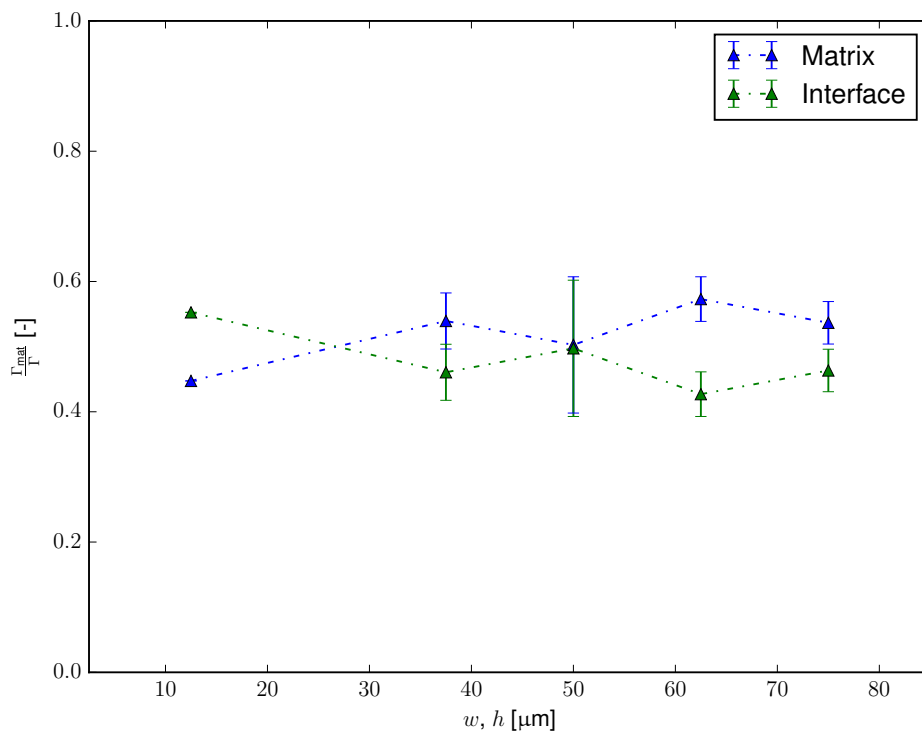


Figure 5.35: RVE Convergence: Crack Material Content, Biaxial Extension-Compression

### 5.2.3 Mixed Mode

The mixed load case (see: Figure 5.4c) resulted in combined mode I and mode II opening, with the mode mixity parameter in the 0.6-0.7 range. A convergence study of the mode I ETSL is included in Figure 5.36. The mode II ETSLs are plotted in Figure 5.37. For all considered MVE sizes the initial fracture occurs in mode I, and as a result the peaks of the mode I ETSLs are higher than that of their mode II companions.

Judging by Figure 5.36, the ultimate strength seems to converge rapidly to around 35 MPa. The softening portion of the ETSL, however, has a lot of spread and the difference between the realizations was observed to be high, resulting in large standard deviations.

For mode II the situation is different. The peak mode II traction settles at approximately 7 MPa for the larger MVE sizes. The mode II opening is mostly in the viscous portion of the analysis. The mode-mixity is not constant throughout the simulation, with initial opening in mode I and increasing mode II opening towards the end of the simulation. To obtain the mode I and mode II behavior the mode-mixity at the end of the simulation is used to separate the vectors into their normal and tangential component; Therefore, comparing the modes separately may not be the best method to determine the RVE size.

The absolute traction is plotted against the absolute opening in Figure 5.38. The effective fracture behavior, for this load case, converges for an RVE size of  $50 \times 50 \mu\text{m}$ . The material content of the crack is given in Figure 5.39. The material composition is quite stable and settles at 70% interface and 30% matrix.

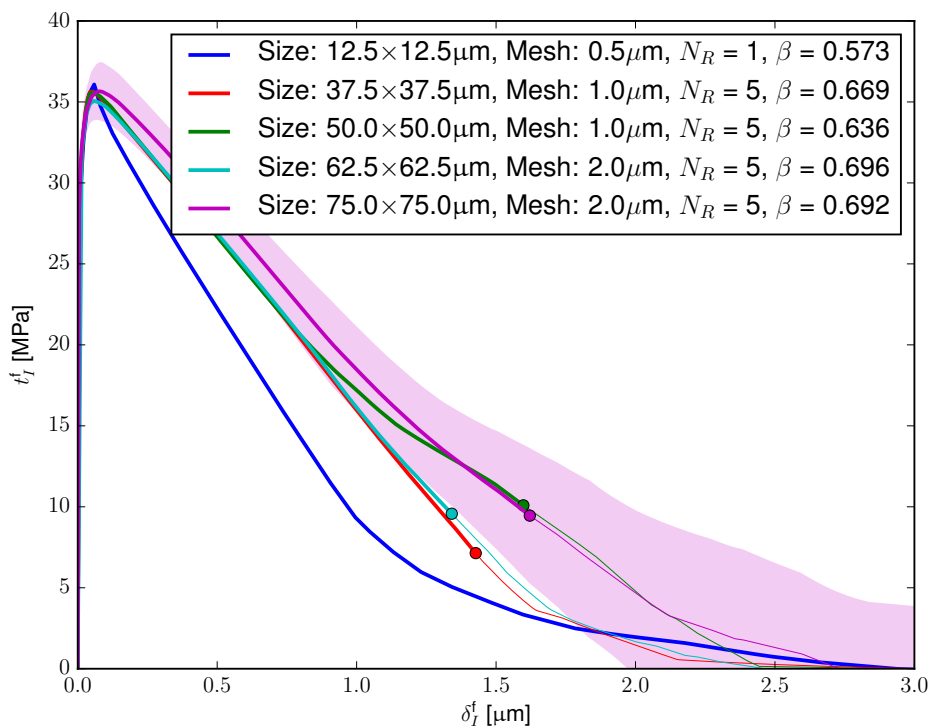


Figure 5.36: RVE Convergence: ETSL Mode I, Mixed

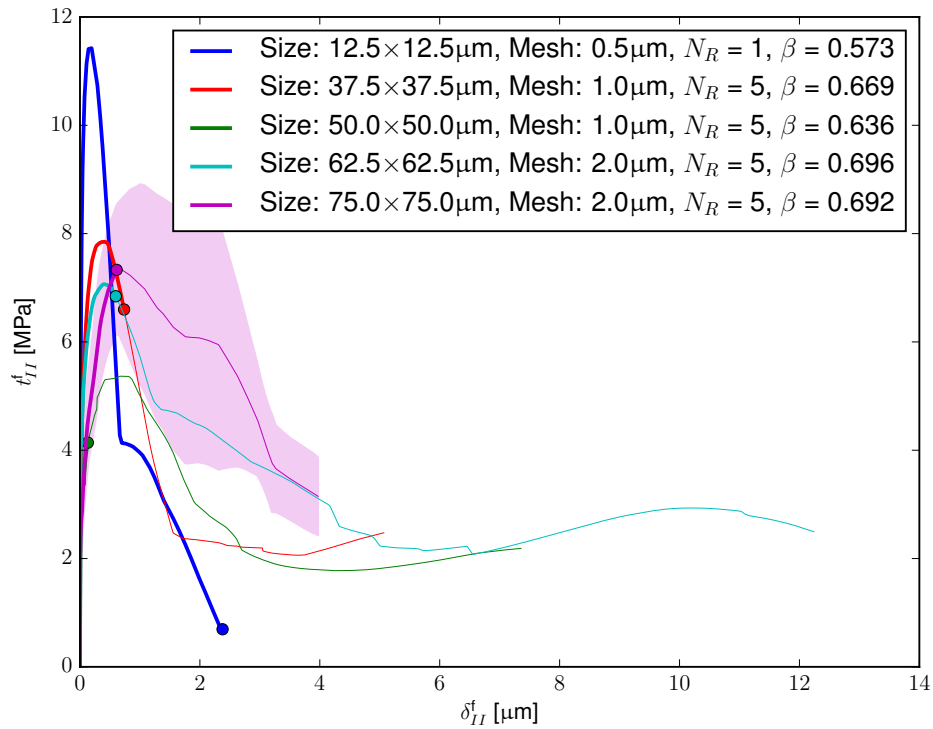


Figure 5.37: RVE Convergence: ETSL Mode II, Mixed

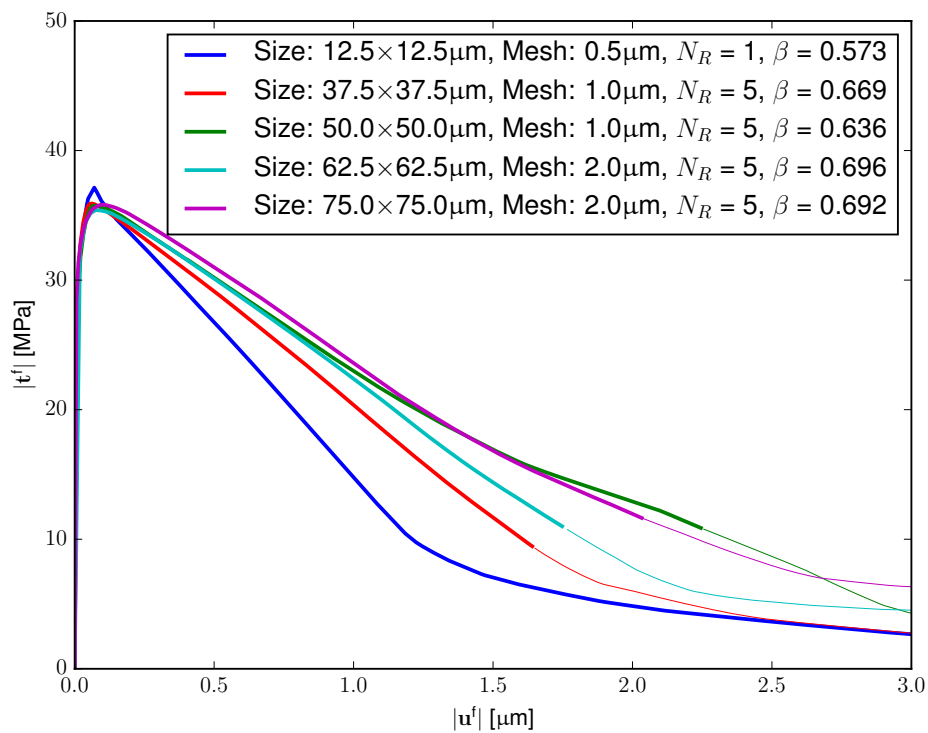
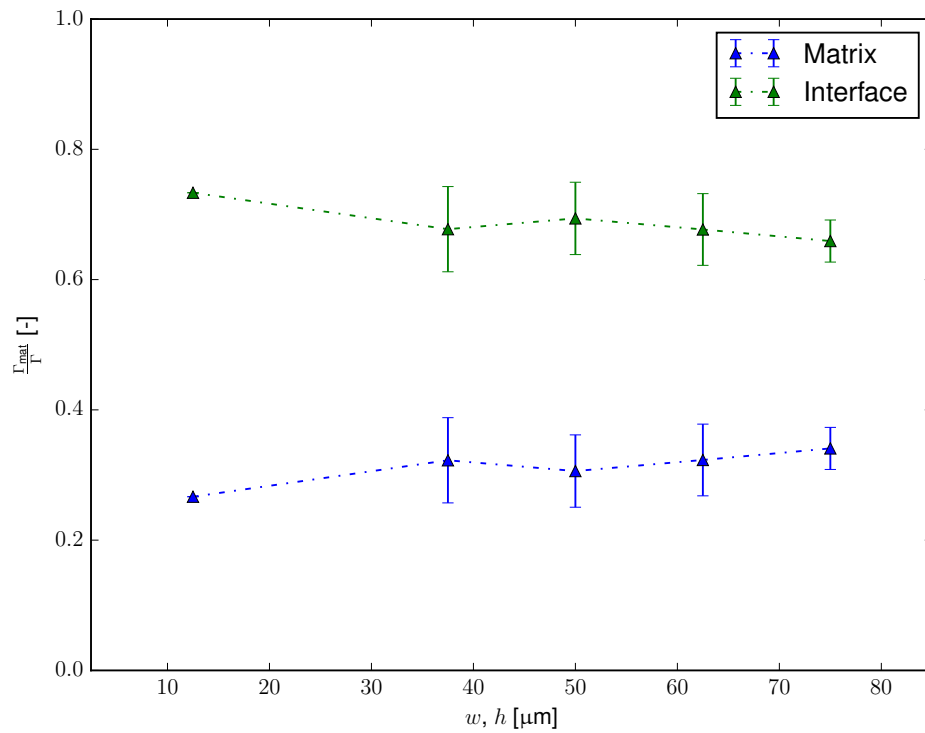


Figure 5.38: RVE Convergence: ETSL absolute, Mixed



**Figure 5.39:** RVE Convergence: Crack Material Content, Mixed

The RVE size for both the uniaxial extension as well as the mixed load case was found to be  $50 \times 50 \mu\text{m}$ . To obtain representative mode II fracture behavior, a larger MVE is required. The RVE size for mode II was determined to be  $75 \times 75 \mu\text{m}$ . Representative fracture behavior for the considered material properties and volume fraction can be found in all modes with an RVE of  $75 \times 75 \mu\text{m}$ .



# Simulations at Cryogenic Temperature

The Representative Volume Element (RVE) size was established in Chapter 5. The size convergence study was performed at room temperature. The RVE size was determined to be  $75 \times 75 \mu\text{m}$  for a weak interface and a fiber volume fraction of 50%. The RVE geometry is included in Table 6.1.

Description	Value
Width	$75 \mu\text{m}$
Height	$75 \mu\text{m}$
Fiber radius	$5 \mu\text{m}$
Fiber volume fraction	50%

**Table 6.1:** RVE geometry

With an established RVE, a working multiscale analysis tool for fracture in composites was complete in construction. At this point, the tool could be applied to study cryogenic fracture behavior, by including a thermal step prior to the mechanical load step, as discussed in Chapter 4. The size convergence study was not repeated for the cryogenic load case. Instead the room temperature RVE was assumed to remain representative for the fracture behavior at cryogenic conditions. This is a safe assumption as long as the fracture mechanism does not change significantly.

The thermal and mechanical properties of the fiber and matrix are given in Table 6.2. The envisioned application of Carbon Fiber Reinforced Plastic (CFRP) to an Engine Thrust Frame (ETF) by Airbus Defence and Space will use HexTow<sup>®</sup> IM7 fibers combined with CYCOM<sup>®</sup> 5230-1 epoxy. The material properties were based upon material data sheets of the pure constituents. The transverse elastic modulus of the carbon fiber and the temperature dependent Coefficient of Thermal Expansion (CTE) of the epoxy were obtained from reference [12].

Property	Fiber	Matrix		Units
		50 K	300 K	
Density	$1.8 \cdot 10^{-6}$	$1.31 \cdot 10^{-6}$		kg/mm <sup>3</sup>
Elastic Modulus	19000	6540	3520	MPa
Poisson's ratio	0.23	0.35		[-]
Coefficient of Thermal Expansion	$7 \cdot 10^{-6}$	$1.4 \cdot 10^{-5}$	$5.6 \cdot 10^{-5}$	K <sup>-1</sup>
Specific Heat	0.879	1.0		mJ/(kg K)
Thermal Conductivity	5.4	0.35		mW/(mm K)

**Table 6.2:** Bulk Material Properties [12, 16, 34]

The strength of the constituents was kept the same as in the convergence study and is included in Table 6.3. The properties assume a weak interface and strong fibers with respect to the matrix. The cohesive material properties were based on references [3, 73].

Property	Fiber		Matrix		Interface		Units
	50 K	300 K	50 K	300 K	50 K	300 K	
Ultimate Traction <sup>1</sup>	100	100	50	50	25	25	MPa
Fracture Energy	0.1	0.1	0.05	0.05	0.025	0.025	N/mm
Failure Opening	2.0	2.0	2.0	2.0	2.0	2.0	μm

**Table 6.3:** Cohesive Material Properties

The remainder of this chapter will discuss the results found for composites under cryogenic loading. The thermal analysis results are discussed in Section 6.1. The results of the cryogenic fracture simulations are included in Section 6.2. This section also includes a comparison with room temperature results to isolate the effect of the thermal load. The mode-dependency of the fracture behavior is studied in Section 6.3. Concluding remarks regarding the multiscale method applied to study cryogenic fracture of composites are presented in Section 6.5.

## 6.1 Thermal Analysis Results

The results of the thermal load step, which occurs prior to the mechanical load step, were used to study the thermal behavior of the composite. The effective CTE of the composite was determined and compared to an approximation obtained using the Rule of Mixtures (RoM). The results of this CTE study are included in Section 6.1.1. Field data of the last thermal load increment was used to investigate the thermal stress field in the composites. Section 6.1.2 contains an overview and a quantitative discussion of the thermal stress results.

### 6.1.1 Effective Coefficient of Thermal Expansion

The time incremental strain results of the thermal load step are used to compute an effective CTE of the composite. The volume-averaged strain is computed for every time step

<sup>1</sup>Mode independent

using Eq. (4.6). The volume-averaged strain tensor is a symmetric tensor with the following components:

$$\langle \epsilon \rangle_{\Omega} = \begin{bmatrix} \langle \epsilon_{11} \rangle_{\Omega} & \langle \epsilon_{12} \rangle_{\Omega} \\ \langle \epsilon_{12} \rangle_{\Omega} & \langle \epsilon_{22} \rangle_{\Omega} \end{bmatrix}$$

The thermal contraction as a result of cooling is represented by the diagonal terms of the volume-averaged strain tensor. The off-diagonal entries represent the shear strain resulting from the thermal loading. Figure 6.1 shows the evolution of the strain components as the temperature is reduced from  $T_0 = 298$  K to the cryogenic temperature  $T_1 = 77$  K.

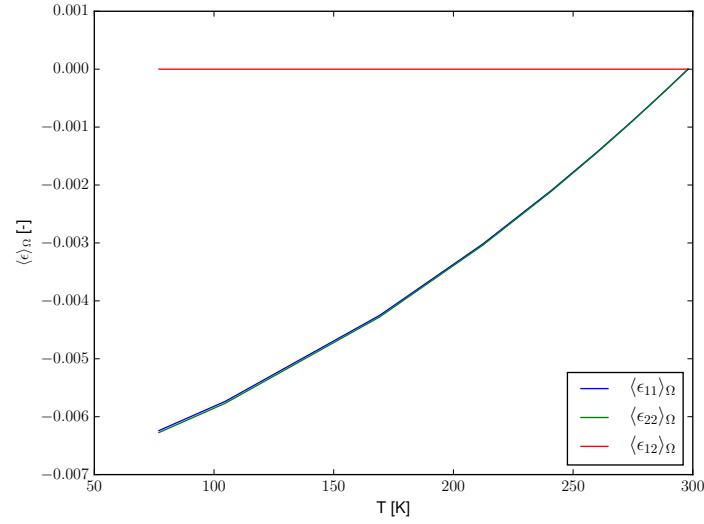


**Figure 6.1:** Thermal Strain Evolution

The analysis on the RVE shows the composite is transversely isotropic, with:

$$\begin{aligned} \langle \epsilon_{11} \rangle_{\Omega} &\approx \langle \epsilon_{22} \rangle_{\Omega} \\ \langle \epsilon_{12} \rangle_{\Omega} &= 0 \end{aligned}$$

Like the corresponding thermal strain tensor components, the CTEs in 1- and 2-directions are approximately equal. The effective CTE of the composite is computed as the average of  $\alpha_{11}$  and  $\alpha_{22}$  and is plotted in Figure 6.2. The constituent input is also included in Figure 6.2. The effective CTE is in between the fiber and matrix behavior, but clearly more influenced by the matrix.

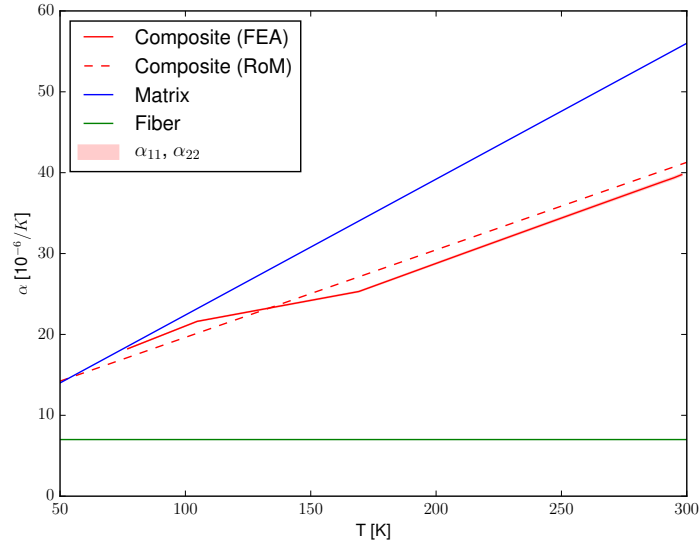


**Figure 6.2:** Effective CTE of the Composite

Figure 6.2 includes a RoM solution for the CTE obtained using Eq. (6.1)

$$\alpha_{22} = (1 + \nu_{23f})\alpha_{22f}V_f + (1 + \nu_m)\alpha_m V_m + \alpha_{11}\nu_{12} \quad (6.1)$$

and  $\alpha_{33} = \alpha_{22}$ . The axis system used in Eq. (6.1) corresponds to the fiber reference system prevalent in associated literature; 1-axis in fiber direction, 2-axis in transverse direction and the 3-axis is the out-of-plane (thickness) direction. In contrast, all analysis in this thesis has the 1,2-plane as the transverse plane, to accommodate the plane-strain definition in ABAQUS®.

In order to evaluate Eq. (6.1), the longitudinal CTE of the composite must be obtained first by using Eq. (6.2).

$$\alpha_{11} = \frac{1}{E_{11}} (\alpha_{11f}E_{11f}V_f - \alpha_m E_m V_m) \quad (6.2)$$

Longitudinal properties of composite lamina are dominated by the fiber properties, as they are usually orders of magnitude stiffer as well as stronger and more brittle. Assuming a perfect bond between the fibers and the matrix, a parallel (Voigt) model for the longitudinal modulus can be used to compute the longitudinal stiffness. The Young's modulus of the lamina in fiber direction can be found with the *rule of mixtures* as given by Eq. (6.3).

$$E_{11} = V_f E_{11f} + V_m E_m \quad (6.3)$$

The same assumptions lead to a similar relation for the major (longitudinal) Poisson's ratio of the lamina:

$$\nu_{12} = \nu_{13} = \nu_f V_f + \nu_m V_m \quad (6.4)$$

Where  $\nu_f = \nu_{12f} = \nu_{13f}$ .

Figure 6.2 shows the computationally computed effective CTE and the analytical solution are similar. The computational results are based on less assumptions and include more details - such as the distribution of the fibers and the fiber-matrix bond - than the analytical solution. The fact that the analytically obtained solution is close to the Finite Element Analysis (FEA) results does inspire confidence in the simulation and verifies the computational method.

### 6.1.2 Thermal Stress

While the effective CTE of the composite is an interesting result, the thermal residual stress at cryogenic temperature is of direct interest to Airbus DS and was formulated as a project goal in Chapter 1.

The last frame of the thermal load step is the equilibrium state at cryogenic temperature (77 K). The complete stress tensor for each bulk element in the RVE is exported to `python`. The stress tensor is symmetric and of the following form:

$$\boldsymbol{\sigma} = \begin{bmatrix} \sigma_{11} & \sigma_{12} \\ \sigma_{12} & \sigma_{22} \end{bmatrix}$$

The tensor components are used to compute the in-plane principal stresses ( $\sigma_1, \sigma_2$ ) using Eq. (6.5).

$$\sigma_{1,2} = \frac{\sigma_{11} + \sigma_{22}}{2} \pm \sqrt{\left(\frac{\sigma_{11} - \sigma_{22}}{2}\right)^2 + \sigma_{12}^2} \quad (6.5)$$

The maximum in-plane principal stress is given by the "+"-solution of Eq. (6.5). A positive maximum principal stress indicates the value of the maximum tensile stress at the material point, while a negative maximum principal stress corresponds to the minimum compressive stress at a material point under biaxial compression. The "-"-solution gives the minimum principal stress, corresponding to the maximum compression or the lowest tensile stress for a biaxial tensile stress state.

Compressive stresses do not directly drive fracture as they are a closing force. The maximum principal stress, when positive, is an opening force on a crack and therefore, for the purpose of the project, deemed the most useful representation of the stress state in the RVE. The in-plane maximum principal stress at 77 K for all five realizations are presented in Figure 6.3.

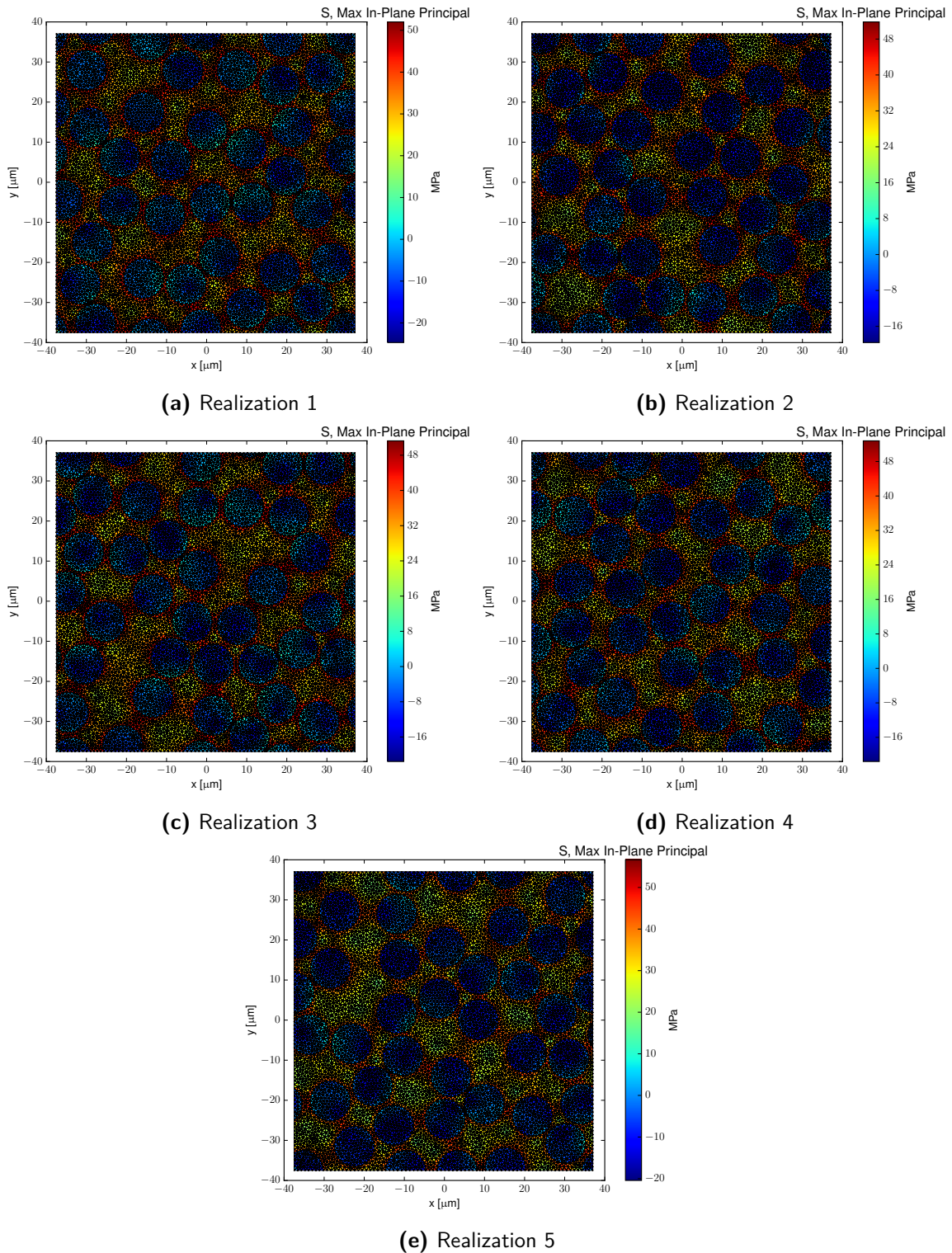


**Figure 6.3:** Thermal Stress at  $T = 77$  K

The maximum tension occurring anywhere in the five realizations is around 56 MPa (see: Figure 6.3e). This stress occurs at the edge of the RVE ( $x, y = 10, -37.5 \mu\text{m}$ ) and is influenced

by boundary effects. The maximum tensile stresses towards the center of the RVE are around 50 MPa and occur in the matrix along the fiber-matrix interface.

The thermal stresses arise as a result of the mismatch in CTE between the matrix and the fiber. The mechanism is shown schematically in Figure 6.4.

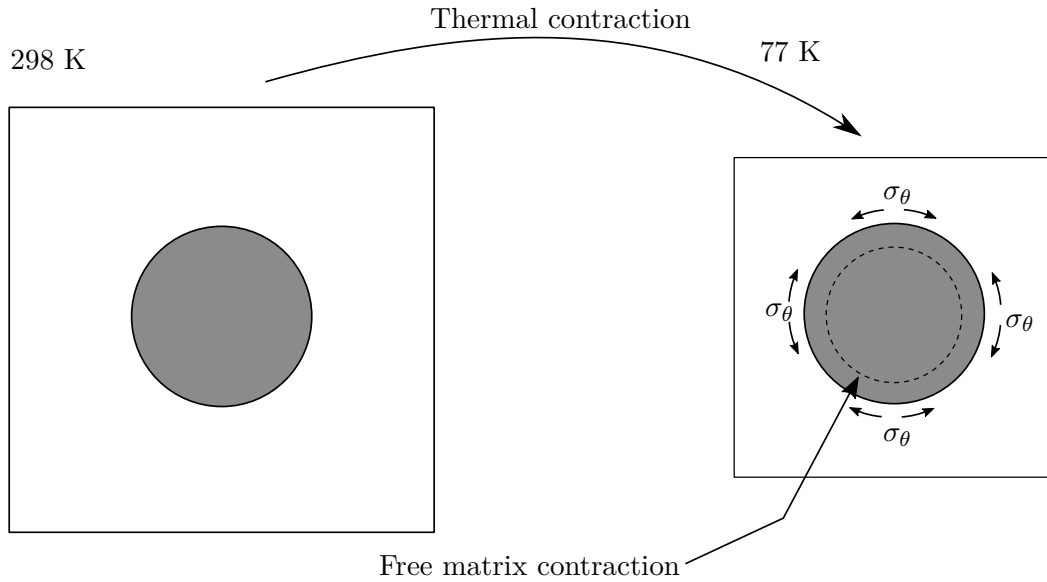


**Figure 6.4:** Thermal tensile stress in the matrix developing radially around fibers

Using the material properties listed in Table 6.2, the matrix stiffness and CTE at 77 K and the CTE at 298 K were computed as:

$$\begin{aligned} E_{M,77K} &= 6214 \text{ MPa} \\ \alpha_{M,77K} &= 1.85 \cdot 10^{-5} \text{ K}^{-1} \\ \alpha_{M,298K} &= 5.57 \cdot 10^{-5} \text{ K}^{-1} \end{aligned}$$

The average CTE in the  $T \in [0, 298]$  K range equals:

$$\alpha_{M,avg} = 3.71 \cdot 10^{-5} \text{ K}^{-1}$$

The free thermal strain in the matrix at 77 K equals:

$$\epsilon_{M,free} = 3.71 \cdot 10^{-5} \cdot (77 - 298) = -0.0082$$

Whereas the free thermal strain in the fiber is:

$$\epsilon_{M,free} = 7 \cdot 10^{-6} \cdot (77 - 298) = -0.0015$$

To simplify the analysis, it is assumed that the matrix must conform to the fiber deformation, since this is the stiffest constituent. Moreover, this assumption will result in the "worst-case" scenario, i.e. the highest thermal stresses. The tangential mechanical stress in the matrix as a result of complying to the fiber deformation equals:

$$\sigma_{\theta} = 41.6 \text{ MPa}$$

This analytically obtained number is 16.8% lower than the maximum in-plane principal stress obtained from the simulation; However, the calculation did not include the effect of two fibers close to each other and should only be used to compare the order of magnitude.

It can be concluded that the performed thermal FEA on the RVE is an effective method to compute the thermal residual stresses arising from the mismatch in CTE of the fiber and the matrix. The analysis was performed using material properties typical to intermediate modulus carbon fiber (HexTow<sup>®</sup> IM7) and epoxy (CYCOM<sup>®</sup> 5230-1). The maximum tensile stress occurring in the composite as a result of free contraction under the cryogenic loading is approximately 50 MPa.

## 6.2 Fracture

The thesis objective is to determine the effect of the cryogenic environment on the progressive failure of the composite. The constitutive relationship, or Effective Traction Separation Law (ETSL) describing the progressive failure of the composite, is the result of microscale fracture simulations on RVEs. The ETSL is the outcome of averaging the results obtained for five realizations of the same RVE size, but with different random fiber distributions.

The microscale analysis was performed on  $75 \times 75 \mu\text{m}$  RVEs for which convergence in three different fracture modes was established in Chapter 5. The five realizations used in the analysis are shown in Figure 6.5.

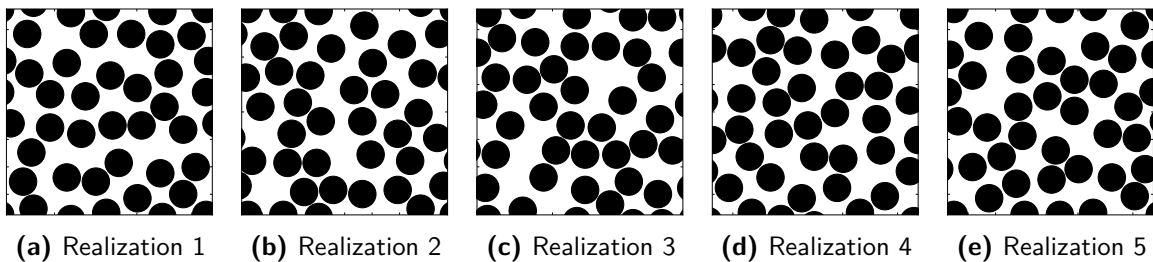


**Figure 6.5:** Five Realizations of the  $75 \times 75 \mu\text{m}$  RVE ( $V_f = 50\%$ )

### 6.2.1 Uniaxial extension

The ETSLs for the uniaxial extension simulations for both temperatures are plotted in Figure 6.6. The power plots used to verify the Hill-Mandel condition on the crack are included in the appendix (see: Figure A.1 and Figure A.2). The results show that the effect of the cryogenic temperature and the resulting thermal residual stresses on the effective fracture

behavior is negligible. The cryogenic ETSL has an effective ultimate traction slightly above that of the room temperature ETSL.

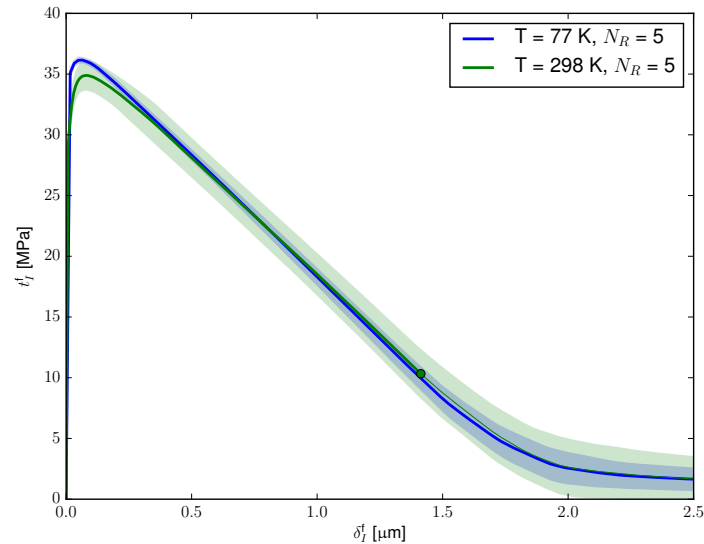


**Figure 6.6:** Uniaxial Extension (Mode I)

The limited effect of the temperature reduction can be explained by examining the content of the crack. Shown in Figure 6.7, the crack follows the fiber-matrix interface for approximately 75% of its total length, for both the room temperature as well as the cryogenic simulation. The restricted thermal contraction of the matrix loads the interface under radial compression. The first portion of the load step is used to alleviate the pre-compression on the interface. As a result, the effective ultimate traction is higher for the cryogenic case.

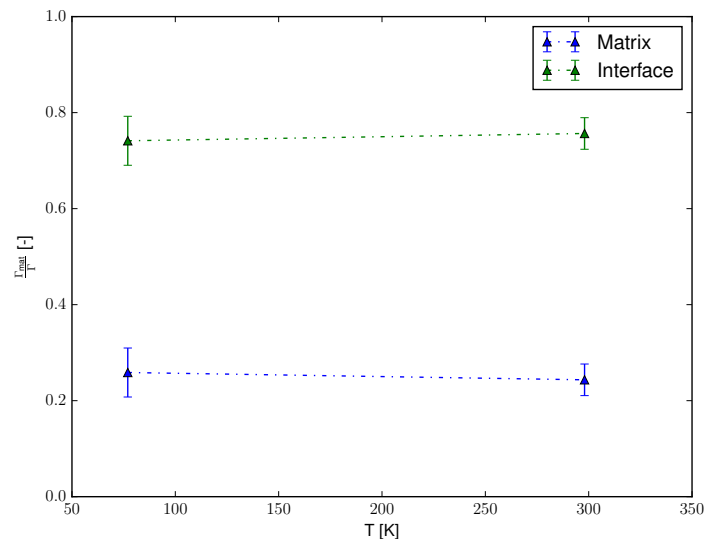


**Figure 6.7:** Crack Material Content: Uniaxial Extension

Following crack initiation the thermal stresses in the neighborhood of the crack are partially

removed, since there is less surrounding material preventing free thermal contraction. As a result, the cryogenic ETSL and its Room Temperature (RT) counterpart are almost equal throughout most of the fracture process.

## 6.2.2 Biaxial extension-compression

The biaxial extension-compression loading equals pure-shear under  $45^\circ$ , resulting in a mode II crack in the maximum shear direction. The mode II ETSLs obtained from the RT and cryogenic simulations are shown in Figure 6.8. The curves used to verify the Hill-Mandel condition on the crack are included in Figure A.3 and Figure A.4. Unlike the uniaxial extension load case, the cryogenic ETSL is entirely under the room temperature ETSL. It should be noted that the standard deviation of the cryogenic ETSL is very large, corresponding to a large spread of results for the different realizations. Moreover, the viscous portion of the ETSL (dashed) is entered early-on for both simulations.

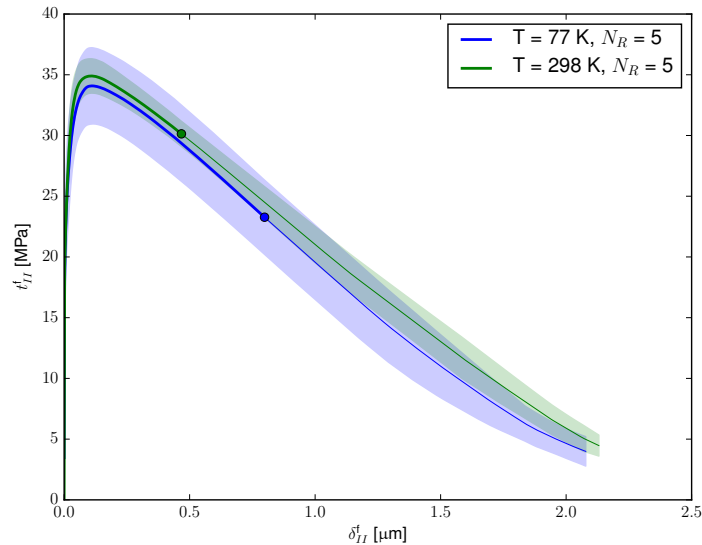


**Figure 6.8:** Biaxial Extension-Compression (Mode II)

The material content of the crack is shown in Figure 6.9. The temperature has no measurable effect on the make-up of the crack, with 45% matrix and 55% interface for both temperatures. With the crack opening in mode II, the pre-compression of the interface has no beneficial effect on the effective ultimate strength. The high thermal residual stress in the matrix combined with the larger matrix fraction of the crack, has a negative effect on both the effective ultimate strength as well as the fracture energy at cryogenic temperature.

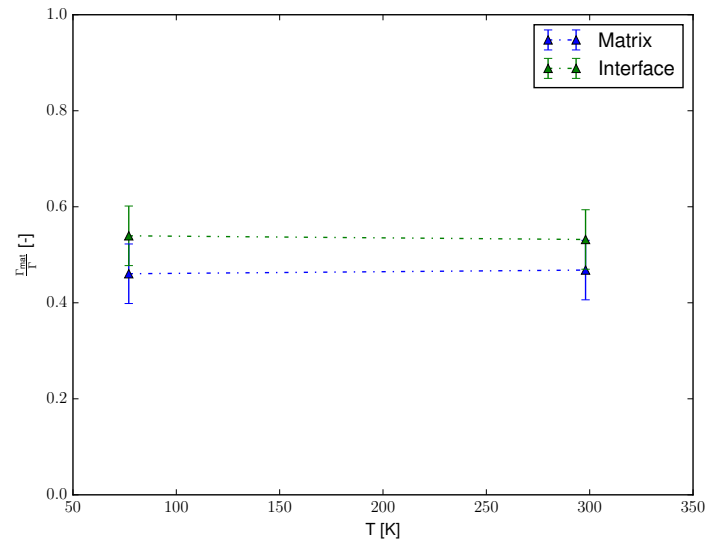


**Figure 6.9:** Crack Material Content: Biaxial Extension-Compression

### 6.2.3 Mixed Mode

The mixed mode load case is a combination of shear and extension, resulting in both normal and tangential crack opening. The ETSL for mode I is included in Figure 6.10. The Hill-Mandel power plots of the mixed mode simulations are included in Figure A.5 and Figure A.6. Figure 6.10 shows that the effective ultimate strength averaged over the realizations is approximately equal between the two temperatures. For both temperatures the spread in the results of the different realizations is high, resulting in a large standard deviation.

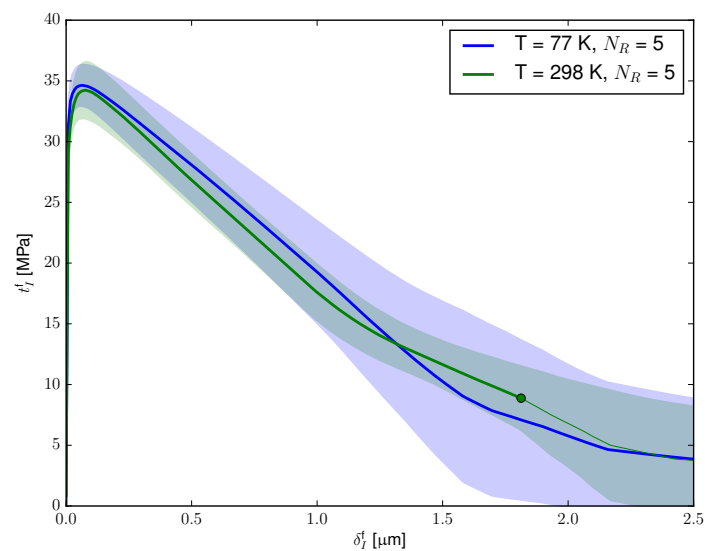


**Figure 6.10:** Mixed (Mode I)

The mode II ETSL is included in Figure 6.11. The mode II opening occurs after initial

fracture in mode I. The maximum tangential traction is, as a result of this chronology, lower. The tangential opening occurs almost exclusively in the viscous portion of the simulation, limiting the confidence in the result. Moreover, the standard deviation is large as seen from the shaded areas.

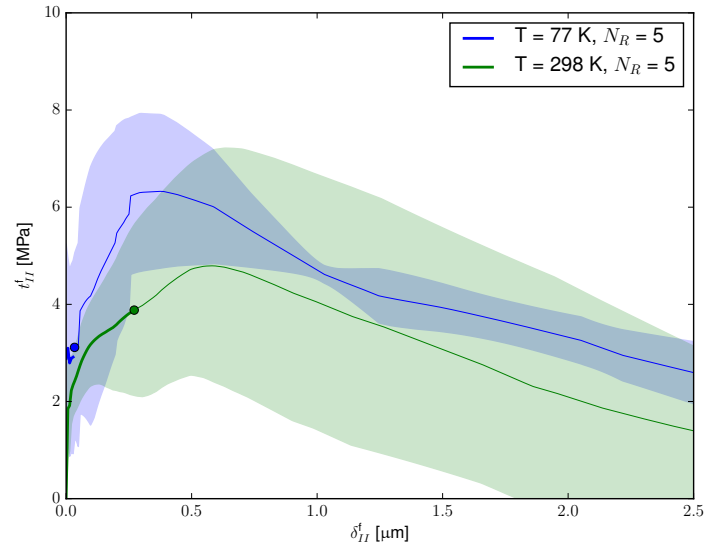


**Figure 6.11:** Mixed (Mode II)

The composition of the crack is presented in Figure 6.12. The temperature has no effect on the material fractions, with the matrix at 25% and the interface at 75% of the total crack length for both room and cryogenic temperature.

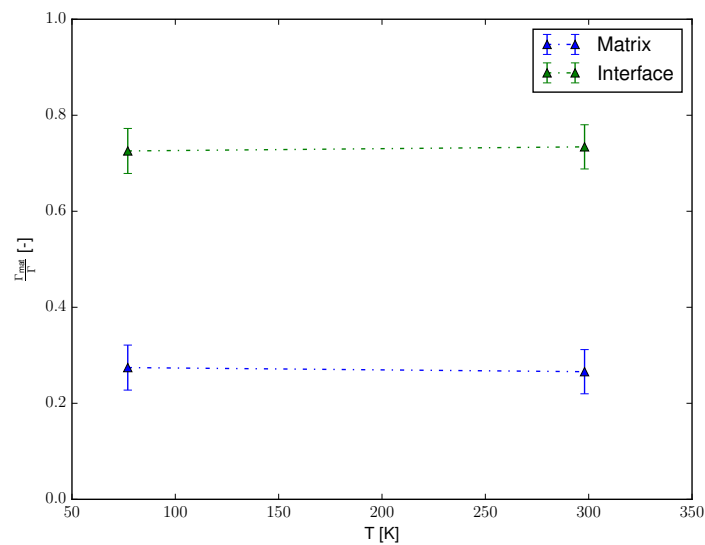


**Figure 6.12:** Crack Material Content: Mixed

### 6.3 Mode mixity

The absolute value of the ultimate traction at 298 K and 77 K is plotted against the mode mixity in Figure 6.13. For both temperatures the line is almost horizontal corresponding to mode-independent fracture initiation behavior. The relative difference between the RT and cryogenic strength is within 5%.

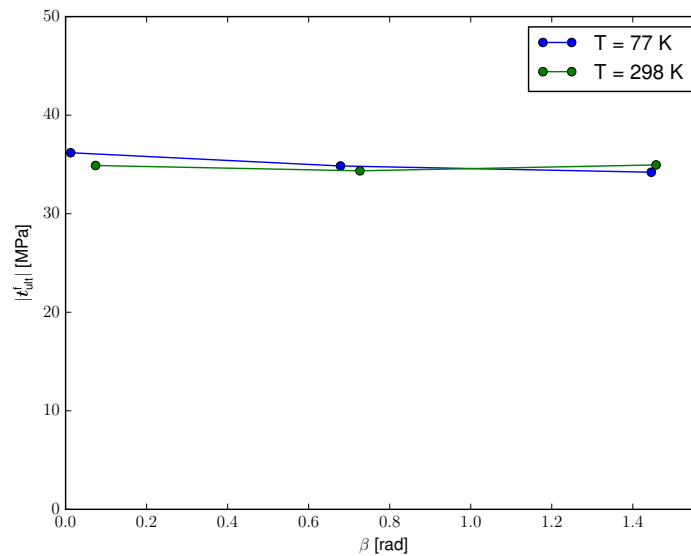


**Figure 6.13:** Ultimate traction as a function of mode mixity

The fracture energy as a function of mode-mixity is given in Figure 6.14. The fracture energy was determined as the area underneath the absolute traction-separation relation, up to the common failure opening of  $\delta_f = 2 \mu\text{m}$  (see: Table 6.3).

$$G_f^f = \int_0^{t_F} \mathbf{t}^f \cdot \llbracket \mathbf{u} \rrbracket^f dt$$

The effective fracture energy in the mixed mode and mode II is higher than that of mode I fracture. The mixed mode and mode II simulations were, however, harder to converge with more viscous energy dissipation as a result. The mode II absolute traction includes a substantial compressive normal traction component as a result of sliding over an uneven surface. The fracture energy outcome is less reliable as a result.

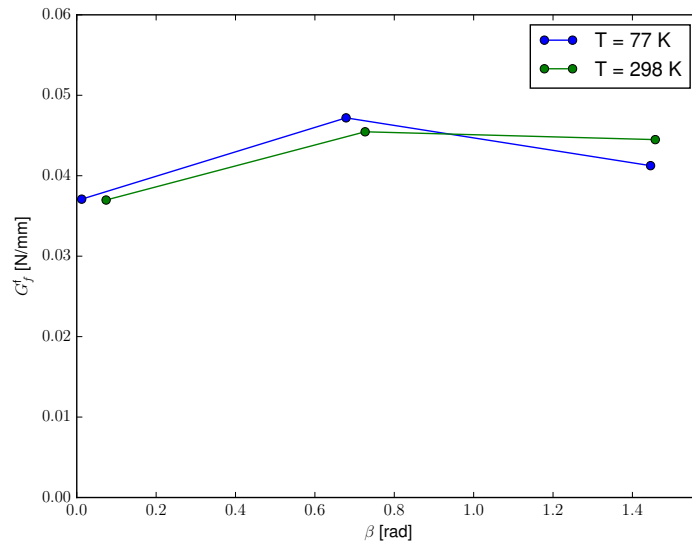


**Figure 6.14:** Fracture Energy as a Function of Mode Mixity

The results shown in Figure 6.13 Figure 6.14, with combined transverse isotropy of the composite structure and mode-independent constituent properties, point to a mode-independent ETSL. Upon closer examination, however, it becomes apparent that the mode I and mode II fracture mechanisms differ on some critical points. Firstly, the material content is significantly different with 75-25% interface-matrix for the pure mode I crack (see: Figure 6.7) and a more equal distribution of 55-45% for the mode II crack (see: Figure 6.9).

The crack morphology of a typical uniaxial extension and biaxial extension-compression case is included in Figure 6.15. While the mode I crack winds through the composite, following the interface as much as possible, the mode II crack is more straight. The kinematics of a mode II crack require a flat sliding surface, giving the crack less room to follow weak links in the structure. As a result, the ratio between the microscopic crack length and the effective macroscopic crack length is closer to 1 compared to the mode I crack.

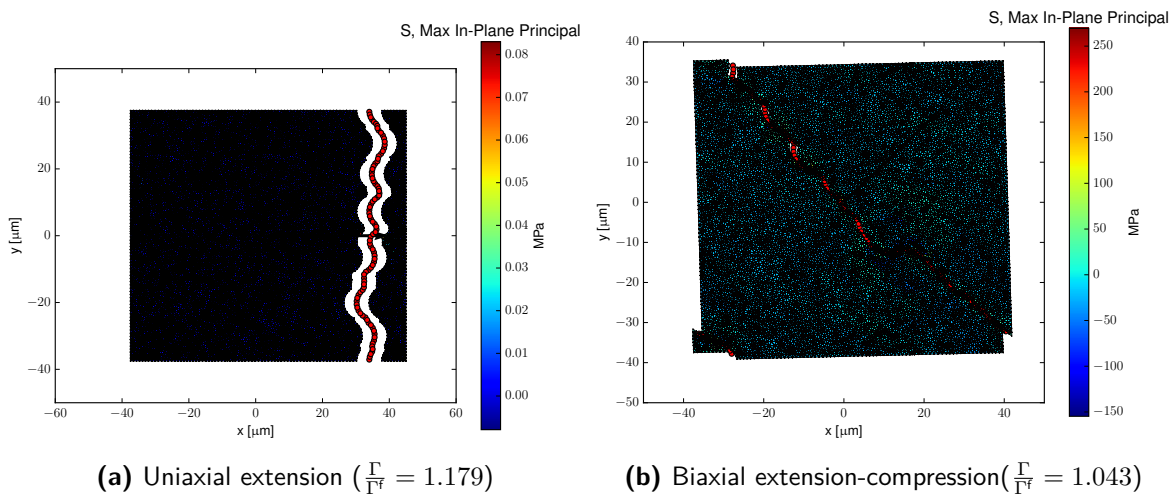


**Figure 6.15:** Typical Mode I and II Crack Morphologies

Using a RoM solution for the effective strength corrected with the crack length ratio, the mode I and mode II ultimate strengths indeed come out to be similar:

$$\begin{aligned} \text{Mode I:} & \quad (0.75 \cdot 25 + 0.25 \cdot 50) \cdot 1.18 \approx 36.9 \text{ MPa} \\ \text{Mode II:} & \quad (0.55 \cdot 25 + 0.45 \cdot 50) \cdot 1.04 \approx 37.7 \text{ MPa} \end{aligned}$$

The similarity is caused by the combination of material properties and crack morphology and not by actual mode-independence. The RoM solution is reasonably accurate when compared to the analysis results and can be used to come within 10% of the simulation result for both mode I and mode II, as shown in Table 6.4. It should be noted that the fractions used to compute the RoM solution were obtained using the simulation and would not be available otherwise.

	Ultimate strength [MPa]		Difference [%]
	298 K	RoM	
Mode I	34.89	36.9	5.8
Mode II	34.95	37.7	7.9

**Table 6.4:** Comparison between RoM and Simulation Results

## 6.4 Initiation criterion

The macroscale implementation using the cohesive segment approach (see: Section 3.1), requires, besides the effective fracture behavior, a criterion for the crack extension direction. In van Hoorn [73], it was found that a maximum principal strain criterion can be used to determine the crack extension direction on the macroscopic scale. The maximum principal strain direction can be computed using the applied deformation gradient. The principal strain direction was computed for the three considered load cases and included in Table 6.5. The angles are with respect to the horizontal axis (1-direction).

	Deformation Gradient	Strain	Principal Strain	Direction
UE	$\begin{bmatrix} \gamma & 0 \\ 0 & 0 \end{bmatrix}$	$\begin{bmatrix} \gamma & 0 \\ 0 & 0 \end{bmatrix}$	$\begin{bmatrix} \gamma & 0 \\ 0 & 0 \end{bmatrix}$	0°
BEC	$\begin{bmatrix} \gamma & 0 \\ 0 & -\gamma \end{bmatrix}$	$\begin{bmatrix} \gamma & 0 \\ 0 & -\gamma \end{bmatrix}$	$\begin{bmatrix} \gamma & 0 \\ 0 & -\gamma \end{bmatrix}$	0°
MM	$\begin{bmatrix} \gamma & \gamma \\ 0 & 0 \end{bmatrix}$	$\begin{bmatrix} \gamma & \gamma/2 \\ \gamma/2 & 0 \end{bmatrix}$	$\begin{bmatrix} (1 + \sqrt{2})\gamma/2 & 0 \\ 0 & (1 - \sqrt{2})\gamma/2 \end{bmatrix}$	22.5°

**Table 6.5:** Principal strain direction for all three load cases

The crack orientations obtained in the simulation are included in Table 6.6. For the uniaxial extension load case the obtained results coincide the principal strain direction. This cannot be said for the other two load cases. The biaxial extension-compression results consistently showed mode II cracks under  $\pm 45^\circ$ , i.e. in the maximum shear strain direction (see: Figure 5.17). The mixed mode load case did not crack in the direction of the principal strain

either. Rather than pure mode I opening on a slanted  $22.5^\circ$  crack, a vertical crack is formed which opens laterally.

	Simulation					Max Principal Strain
	R1	R2	R3	R4	R5	
UE	$0.000320^\circ$	$-0.0489^\circ$	$-0.0318^\circ$	$-5.29^\circ$	$-4.99^\circ$	$0^\circ$
BEC	$-43.7^\circ$	$-42.2^\circ$	$43.7^\circ$	$-44.9^\circ$	$43.9^\circ$	$0^\circ$
MM	$0.688^\circ$	$0.435^\circ$	$0.490^\circ$	$0.708^\circ$	$1.40^\circ$	$22.5^\circ$

**Table 6.6:** Crack orientation observed in the simulation (RT) compared to the principal strain direction

A maximum principal strain criterion is therefore not suitable to determine the crack extension direction. A maximum stress criterion might be better suited to compute the crack extension direction. The stress is, however, unlike the strain, not known a priori. The applied stress tensor can be obtained with the applied strain and a macroscopic constitutive law, obtained through volume averaging of the RVE. This is, however, outside of the scope of this thesis project.

## 6.5 Conclusion

Thermal analysis on the RVE was used to compute the CTE of the composite through strain homogenization. The effective CTE in 1- and 2-direction are equal and there was no average shear deformation as a result of the thermal load. The results were consistent with transversely isotropic material behavior. A RoM solution was used to verify the method.

The thermal stresses at cryogenic temperature were computed for five realizations of the RVE. The maximum tensile stress in the composite at 77 K was found to be approximately 50 MPa for intermediate modulus carbon fiber (HexTow<sup>®</sup> IM7) and epoxy (CYCOM<sup>®</sup> 5230-1).

Multiscale ETSLs for fracture of the composite at cryogenic temperature were compared to their RT counterparts. The ultimate strength in mode I fracture was found to be higher at cryogenic temperature, although the difference was not significant. The ultimate shear strength (mode II) was impacted negatively by cooling. The mixed mode fracture was left unaffected. It can be concluded that the composite strength at ply level is not impacted significantly by reducing the temperature to 77 K.

For the material properties considered, a mode-independent macroscopic fracture model is reasonable. It was found that the material composition and the crack morphology were dependent on the fracture mode. Therefore, it should not be expected that a mode-independent model works well for every combination of material properties. In general the fracture process is influenced by the opening mode.

# Conclusions and Recommendations

## 7.1 Conclusions

Airbus Defence and Space is seeking to replace aluminum by Carbon Fiber Reinforced Plastic (CFRP) for an Engine Thrust Frame (ETF) that connects a cryogenic second stage tank to the rocket engine. The absence of a reliable predictive failure method for composites under cryogenic conditions has inhibited development of such a structure in the past. This project was developed and carried out in an effort to provide new insights into the field of composite fracture mechanics under cryogenic conditions. The conclusions drawn from this study are relevant to companies such as Airbus, where weight savings produced from replacing traditional materials with composites, grant a lucrative and thus, competitive design advantage for space structures.

The technical objective of the project is repeated below:

*The research objective of the MSc. Thesis is to develop a damage onset and growth model for transverse fracture inside Unidirectional (UD) CFRP plies under combined thermal and mechanical loading and under cryogenic conditions, by using advanced numerical methods on the microscopic scale coupled with the macroscale by computational homogenization, a technique known as multiscale modeling.*

Due to limited academic precedence for multiscale modeling of fracture, the project required initial effort to be focused on the model development phase. The multiscale fracture framework must be verified by demonstrating scale coupling; Scale coupling is achieved through satisfying the Hill-Mandel condition and by identifying a Representative Volume Element (RVE). Only after the multiscale fracture model was implemented and verified, could it be used to study cryogenic fracture behavior.

Fracture of composites is characterized by a multitude of failure mechanisms at various spatial scales. The multiscale method captures the combined effect of several failure mechanisms, at the composite ply-level, into a homogenized macroscale fracture model. A new technique for homogenizing fracture properties was proposed by Turteltaub et al. [69]. The proposed

technique was applied in this thesis to study transverse fracture behavior, as discussed in Chapter 3.

The multiscale framework was implemented in `python`, with the mesh-generation performed by `gms` and the analysis in `ABAQUS`<sup>®</sup>, as detailed in Chapter 4. The computational framework is able to produce the Microstructural Volume Element (MVE) geometry, which captures the random fiber distribution seen in composite plies. The meshed geometry, combined with material properties and thermal/mechanical loading, was written to an input file for `ABAQUS`<sup>®</sup>. After `ABAQUS`<sup>®</sup> performed the fracture simulation, results were extracted and used to compute the homogenized fracture response, which was then scrutinized for its representation of micro-scale behavior.

To find a RVE, a mesh and size convergence study was carried out for three different load cases and corresponding fracture modes. The size convergence study followed the approach of Gitman et al. [29], using only mechanical loading and increasing the volume element size until the effective fracture behavior converged (i.e. micro-scale behavior was accurately represented). With this method, it was determined that reasonable effective constitutive fracture behavior for a mode I crack could already be obtained with a unit cell. Convergence of the mode I fracture behavior was achieved with a  $50 \times 50 \mu\text{m}$  MVE, whereas for mode II a minimum RVE size of  $75 \times 75 \mu\text{m}$  was deemed appropriate. The multiscale fracture model, proposed by Turteltaub et al. [69], was implemented successfully and a RVE was established. The model is successful in conserving the rate of work between the micro- and macroscopic scales, which is paramount to the validity of the multiscale method.

With the fracture model implemented and the RVE size determined, the cryogenic conditions were added to arrive at a cryogenic fracture model. The literature study [78] done in preparation of the thesis project concluded that the mismatch of Coefficient of Thermal Expansion (CTE) between the constituents drives the microcracking in composites under cryogenic conditions. The ETF application excludes the effect of fuel intrusion from consideration and instead, the cryogenic conditions were implemented by applying a constant temperature field (77 K) to the RVE in a thermal load step, which occurs prior to the application of mechanical load. Constituent material properties of intermediate modulus carbon fiber (HexTow<sup>®</sup> IM7) and epoxy (CYCOM<sup>®</sup> 5230-1) were used in all analyses. Besides fracture, the microscale simulations were used to find the effective CTE of the composite and to solve the transverse thermal stress field at the cryogenic operating temperature of 77 K.

The results produced by the thermal load step were used to find the effective CTE and the thermal stresses present in the composite, which derive from the mismatch in CTE of the constituents. The resulting effective CTE of the composite was observed to be close to the solution obtained with Rule of Mixtures (RoM). The microscale simulation was based on less assumptions than the RoM and is believed to be a more realistic method to obtain effective transverse thermal properties using constituent behavior. The thermal stress field in the composite microstructure at cryogenic temperature was solved for five realizations of the  $75 \times 75 \mu\text{m}$  RVE. High tension was found in tangential direction around the fibers in the matrix. The maximum thermal tensile stress was approximately 50 MPa.

The multiscale fracture framework was used to compare each mode at both room and cryogenic temperatures. A comparison and discussion of the results are included in Chapter 6. Although the cryogenic temperature resulted in high thermal stresses, the effect on the fracture (strength, energy) was small compared to the standard deviation. The thermal contraction,

as a result of cooling, was found to increase mode I fracture strength while overall mode II fracture properties became weaker due to cryogenic loading.

The mode-dependency of the fracture behavior for room and cryogenic temperatures is included in Chapter 6. The ultimate strength was found to be mode-independent for the set of material properties considered. The fracture energy in mode II was observed to be higher than that of mode I. Higher fracture energy in mode II may be attributed to increased viscosity along with the high normal compressive stresses which result from sliding. A mode-independent macroscopic model is reasonably accurate at both temperatures; however, it was discovered that the opening mode clearly impacts the microscopic length and the material composition of the crack. Therefore, it is concluded that a mode-independent macroscopic fracture model cannot be used for all material combinations.

## 7.2 Recommendations

The overall thesis objective has been achieved, however, the author would like to make the following recommendations which might benefit extensions of this research which seek to improve upon the method developed herein:

- The effective traction was defined using a best-fit to the Hill-Mandel condition by assigning a single fitting parameter constant over the simulation time. As a result, the Hill-Mandel condition is never exactly satisfied over the length of the simulation. Future research should look into a more flexible method for combining the volume- and crack-averaged traction vector, that is able to perfectly match the Hill-Mandel condition on the crack.
- The method used to integrate the traction over the crack face uses a rank-one definition of the stress tensor. There is no possibility to determine the full state of stress using only information of the cohesive elements. Future research could include an integration over the bulk elements adjacent to the crack to obtain the full state of stress at the crack face.
- The viscous energy added by the automatic stabilization algorithm of ABAQUS<sup>®</sup> exceeded the predefined threshold of 5% of the total strain energy in most simulations. Deactivation of the automatic stabilization algorithm had detrimental effects on the stability of the simulations, i.e. divergence. A better understanding of the inner-workings of the automatic stabilization algorithm or a manually defined replacement can give the user better control over the viscosity and potentially help isolate the viscous traction from the results. Reduced viscosity will, however, lead to smaller stable time steps and a higher computational cost.
- There were no imperfections, such as voids or imperfect fiber-matrix bonds, included in the geometry of the MVE. The cryogenic loading of the RVE was shown to result in high thermal stresses, but no microcracking was observed. The overall compressive strain does not allow for any significant crack opening to occur. By including material imperfections, which are present in any real composite, it is believed that an accurate model for microcracking due to thermal loading can be obtained. The material imperfections will act as microcrack initiation sites and provide the room for microcrack

opening. Future research into (cryogenic) fracture of composites through multiscale modeling should include realistic material imperfections at the microscale.

The research done in this thesis also lead to some new ideas for future research in the broader area of fracture mechanics of composites:

- Experimental data on fiber-matrix bond strength, required for the interface properties, is difficult to obtain. One outcome of the research was that a RoM solution, using matrix and interface fractions of the total crack length, can be used to compute the transverse strength to within 10% of the multiscale results. This knowledge can contribute to the design of new experiments created to determine fiber-matrix bond strengths.
- The microscale model showed mode II fracture when biaxial extension-compression was applied to the MVE. Instead of mode I fracture in the principal strain direction, the microscale model consistently preferred mode II along the maximum shear direction. An interesting extension of this research could include an eXtended Finite Element Method (XFEM) simulation on the microscale to verify this finding.
- The effective fracture behavior was found to be mode-independent for the considered material properties. A parameter study can be performed to explore the extend of material combinations, to which a mode-independent model is reasonable. A mode-independent multiscale model would reduce the number of microscale simulations to the number of realizations.

---

# Bibliography

- [1] *Abaqus Analysis User Guide*, Abaqus 6.14 edition.
- [2] M. V. Cid Alfaro. *Multiscale Analyses of Fibre Metal Laminates*. Phd. Thesis, Delft University of Technology (TU Delft), Delft, 2008.
- [3] M. V. Cid Alfaro, A. S. J. Suiker, and R. de Borst. Transverse failure behavior of fiber-epoxy systems. *J. Compos. Mater.*, 44(12):1493–1516, 2010.
- [4] M. V. Cid Alfaro, A. S. J. Suiker, and R. de Borst. Multiscale Modelling of the Failure Behavior of Fibre-Reinforced Laminates. In R. de Borst and E. Ramm, editors, *Multiscale Methods in Computational Mechanics*, Lecture Notes in Applied Computational Mechanics 55, pages 233–259, 2011.
- [5] T. L. Anderson. *FRACTURE MECHANICS*. Taylor & Francis Group LLC., Boca Raton, FL, 3<sup>rd</sup> edition, 2005.
- [6] G.I. Barenblatt. The mathematical theory of equilibrium cracks in brittle fracture. volume 7 of *Advances in Applied Mechanics*, pages 55 – 129. Elsevier, 1962.
- [7] G. E. Beltz and J. R. Rice. Dislocation Nucleation Versus Cleavage Decohesion. In T. C. Lowe, A. D. Rollett, P. S. Follansbee, and G. E. Daehn, editors, *Modeling the Deformation of Crystalline Solids*, pages 457–480. The Minerals, Metals & Materials Society, Harvard University, Cambridge, MA, 1991.
- [8] T. Belytschko, W. K. Liu, B. Moran, and K. Elkhodary. *Nonlinear Finite Elements for Continua and Structures*. John Wiley & Sons Ltd., Hoboken, NJ, 2<sup>nd</sup> edition, 2003. ISBN:978-1-119-63270-3.
- [9] D. S. Brauer, C. Rüssel, S. Vogt, and M. Schnabelrauch. Degradable phosphate glass fiber reinforced polymer matrices: Mechanical properties and cell response. *J. Mater. Sci. Mater. Med.*, 19(1):121–127, 2008.
- [10] G. T. Camacho and M. Ortiz. Computational Modeling of Impact Damage in Brittle Materials. *Int. J. Solids Struct.*, 33(20-22):2899–2938, 1996.

- [11] T. Chao-Dinh, G. Zi, P.-H. Lee, T. Rabczuk, and J.-H. Song. Phantom-node method for shell models with arbitrary cracks. *Comput. Struct.*, 92-93:242–256, 2012.
- [12] S. Choi and B. V. Sankar. Micromechanical Analysis of Composite Laminates at Cryogenic Temperatures. *J. Compos. Mater.*, 40(12):1077–1091, 2006.
- [13] E. W. C. Coenen, V. G. Kouznetsova, and M. G. D. Geers. Novel Boundary Conditions for strain localization analysis in microstructural volume elements. *Int. J. Numer. Meth. Engng*, 90(1):1–21, 2012.
- [14] E. W. C. Coenen, V. G. Kouznetsova, and M. G. D. Geers. Multi-scale continuous-discontinuous framework for computational-homogenization-localization. *J. Mech. Phys. Solids*, 60(8):1486–1507, 2012.
- [15] A. Cornec, I. Schneider, and K.-H. Schwalbe. On the practical application of the cohesive model. *Eng. Fract. Mech.*, 70:1963–1987, 2003.
- [16] *CYCOM<sup>®</sup> 5320-1 Epoxy Resin System*. Cytec Industries Inc., 2014. Rev. October 2015.
- [17] I. M. Daniel and O. Ishai. *Engineering Mechanics of Composite Materials*. Oxford University Press, New York, NY, 2<sup>nd</sup> edition, 2006.
- [18] R. de Borst. Numerical aspects of cohesive-zone models. *Eng. Fract. Mech.*, 70:1743–1757, 2003.
- [19] W. J. Drugan and J. R. Willis. A micromechanics-based nonlocal constitutive equation and estimates of representative volume element size for elastic composites. *J. Mech. Phys. Solids*, 44(4):497–524, 1996.
- [20] Z.-Z. Du. eXtended Finite Element Method (XFEM) in Abaqus. Presentation retrieved from [www.3ds.com](http://www.3ds.com).
- [21] D. S. Dugdale. Yielding of steel sheets containing slits. *J. Mech. Phys. Solids*, 8(3):100–104, August 1960.
- [22] C. Eckart and G. Young. The approximation of one matrix by another of lower rank. *Psychometrika*, 1:211–218, 1936.
- [23] H. D. Espinosa and P. D. Zavattieri. A Grain Level Model for the Study of Failure Initiation and Evolution in Polycrystalline Brittle Materials. Part I: Theory and Numerical Implementation. *Mech. Mater.*, 35(3-6):333–364, 2003.
- [24] P. Evesque. Fluctuations, correlations and representative elementary volume (REV) in granular materials. *Poudres Grains*, 11:6–17, 2000.
- [25] I. Foster. *Designing and Building Parallel Programs*. Addison-Wesley, Boston, MA, 1995.
- [26] Y. Freed and L. Banks-Sills. A New Cohesive Zone Model for Mixed Mode Interface Fracture in Bimaterials. *Eng. Fract. Mech.*, 75(15):4583–4593, 2008.
- [27] P. H. Geubelle and J. S. Baylor. Impact-Induced Delamination of Composites: A 2D Simulation. *Compos. Part B: Eng.*, 29(5):589–602, 1998.

- [28] C. Geuzaine and J.-F. Remacle. *Gmsh Reference Manual*, April 2017. gmsh 3.0.
- [29] I. M. Gitman, H. Askes, and L. J. Sluys. Representative volume: Existence and size determination. *Eng. Fract. Mech.*, 74(16):2518–2534, 2007.
- [30] A. A. Griffith. Phenomena of Rupture and Flow in Solids. *Philos. Trans. Royal Society of London*, 221-A:163–198, October 1921.
- [31] A. Hansbo and P. Hansbo. A finite element method for the simulation of strong and weak discontinuities in solid mechanics. *Comput. Methods. Appl. Mech. Engrg.*, 193(33-35): 3523–3540, 2004.
- [32] Z. Hashin. Analysis of Composite Materials - A Survey. *J. Appl. Mech.*, 50(3):481–505, 1983.
- [33] Z. Hashin and A. Rotem. A Fatigue Failure Criterion for Fiber Reinforced Materials. *J. Compos. Mater.*, 7(4):448–464, 1973.
- [34] *HexTow<sup>®</sup> IM7*. Hexcel Corporation, 2016.
- [35] R. Hill. A Theory of Yielding and Plastic Flow of Anisotropic Metals. In *Proceedings of the Royal Society*, volume 193 of *A: Mathematical, Physical and Engineering Sciences*, pages 281–297, London, 1948. Royal Society.
- [36] R. Hill. Elastic Properties of Reinforced Solids: Some Theoretical Principles. *J. Mech. Phys. Solids*, 11(5):357–372, 1963.
- [37] A. Hillerborg, M. Modeer, and P. E. Peterson. Analysis of crack formation and crack growth in concrete by means of fracture mechanics and finite elements. *Cement Concrete Res.*, 6:773–782, 1976.
- [38] C.E. Inglis. Stresses in a plate due to the presence of cracks and sharp corners. *Trans. Institution of Naval Architects*, 55:219–230, March 1913.
- [39] G. R. Irwin. Analysis of Stresses and Strains near the End of a Crack Transversing a Plate. *J. Appl. Mech.*, 24:361–364, 1957.
- [40] G. R. Irwin. Plastic Zone Near a Crack and Fracture Toughness. In *Sagamore Research Conference Proceedings*, volume 4, 1961.
- [41] D. V. Kubair and P. H. Geubelle. Comparative analysis of extrinsic and intrinsic cohesive models of dynamic fracture. *Int. J. Solids Struct.*, 40(15):3853–3868, July 2003.
- [42] M. G. Kulkarni, P. H. Geubelle, and K. Matouš. Multi-scale modeling of heterogeneous adhesives: Effect of particle decohesion. *Mech. Mater.*, 41(5):573–583, May 2009.
- [43] M. G. Kulkarni, K. Matouš, and P. H. Geubelle. Coupled multi-scale cohesive modeling of failure in heterogeneous adhesives. *Int. J. Numer. Meth. Engng*, 84(8):916–946, November 2010.
- [44] K. Matouš, M. G. Kulkarni, and P. H. Geubelle. Multiscale cohesive failure modeling of heterogeneous adhesives. *J. Mech. Phys. Solids*, 56(4):1511–1533, 2008.

- [45] C. Miehe. Strain-driven homogenization of inelastic microstructures and composites based on an incremental variational formulation. *Int. J. Numer. Meth. Engng*, 55(11): 1285–1322, 2002.
- [46] S. K. Mital, J. Z. Gyekenyesi, S. M. Arnold, R. M. Sullivan, J. M. Manderscheid, and P. L. N. Murthy. Review of Current State of the Art and Key Design Issues With Potential Solutions for Liquid Hydrogen Cryogenic Storage Tank Structures for Aircraft Applications. Technical Report NASA/TM-2006-214346, NASA Glenn Research center, Cleveland, OH, 2006.
- [47] N. I. Muskhelishvili. *Singular integral equations*. P. Noordhoff, Groningen, 2<sup>nd</sup> edition, 1953.
- [48] A. Needleman. A Continuum Model for Void Nucleation by Inclusion Debonding. *ASME J. Appl. Mech.*, 54(3):525–531, 1987.
- [49] A. Needleman. An Analysis of Tensile Decohesion Along an Interface. *J. Mech. Phys. Solids*, 38(3):289–324, 1990.
- [50] V. P. Nguyen. An open source program to generate zero-thickness cohesive interface elements. *Adv. Eng. Softw.*, 74:27–39, 2014.
- [51] V. P. Nguyen. Discontinuous galerkin/extrinsic cohesive zone modeling: Implementation caveats and applications in computational fracture mechanics. *Eng. Fract. Mech.*, 128: 37–68, 2014.
- [52] V. P. Nguyen, O. Lloberas-Valls, M. Stroeven, and L. J. Sluys. Homogenization-based multiscale crack modelling: From micro-diffusive damage to macro-cracks. *Comput. Methods Appl. Mech. Engrg.*, 200(9-12):1220–1236, 2011.
- [53] M. Ortiz and A. Pandolfi. Finite-Deformation Irreversible Cohesive Elements for three-dimensional Crack-Propagation Analysis. *Int. J. Numer. Meth. Engng.*, 44(9):1267–1282, 1999.
- [54] M. Ostoja-Starzewski. Microstructural randomness versus representative volume element in thermomechanics. *J. Appl. Mech.*, 69(1):25–35, 2002.
- [55] K. Park and G. H. Paulino. Cohesive Zone Models: A Critical Review of Traction-Separation Relationships Across Fracture Surfaces. *Appl. Mech. Rev.*, 64, November 2011.
- [56] K. Park, G. H. Paulino, and J. R. Roesler. A Unified Potential-Based Cohesive Model of Mixed-Mode Fracture. *J. Mech. Phys. Solids*, 57(6):891–908, 2009.
- [57] P. E. Petersson. Crack Growth and Development of Fracture Zones in Plain Concrete and Similar Materials. Technical Report LUTVDG/TVBM-1006, Lund Institute of Technology, Sweden, 1981.
- [58] A. Puck and H. Schürmann. Failure Theories of FRP Laminates by Means of Physically Based Phenomenological Models. *Compos. Sci. Technol.*, 58:1045–1067, 1998.

- [59] A. Reuss. Berechnung der Fließgrenze von Mischkristallen auf Grund der Plastizitätsbedingung für Einkristalle. *Zeitschrift für Angewandte Mathematik und Mechanik*, 9:49–58, 1929.
- [60] J. R. Rice. A Path Independent Integral and the Approximate Analysis of Strain Concentration by Notches and Cracks. *J. Appl. Mech.*, 35:379–386, 1968.
- [61] J. J. Rimoli and J. J. Rojas. Meshing strategies for the alleviation of mesh-induced effects in cohesive element models. *Int. J. Fract.*, 193(1):29–42, 2015.
- [62] J. H. Rose, J. Ferrante, and J. R. Smith. Universal Binding Energy Curves for Metals and Bimetallic Interfaces. *Phys. Rev. Lett.*, 47(9):675–678, 1981.
- [63] I. Scheider and W. Brocks. Simulation of Cub-Cone Fracture Using the Cohesive Model. *Eng. Fract. Mech.*, 70(14):1943–1961, 2003.
- [64] I. N. Sneddon. The Distribution of Stress in the Neighbourhood of a Crack in an Elastic Solid. In *Proceedings of the Royal Society*, volume 187 of *A: Mathematical, Physical and Engineering Sciences*, pages 229–260, London, 1946. Royal Society.
- [65] V. Srinivasa, V. Shivakumar, V. Nayaka, S. Jagadeeshaiah, M. Seethram, R. Shenoy, and A. Nafidi. Fracture morphology of carbon fiber reinforced plastic composite laminates. *Mat. Res.*, 13(3):417–424, 2010.
- [66] P. V. Trusov and I. E. Keller. *The Theory of Constitutive Relations. Part I*. Perm State Technical University, Perm, 1997. [in Russian].
- [67] S. W. Tsai. Strength Theories of Filament Structures. In R. T. Schwartz and H. T. Schwartz, editors, *Fundamental Aspects of Fiber Reinforced Plastics*, pages 3–11. Wiley Interscience, New York, NY, 1968.
- [68] S. W. Tsai and E. M. Wu. A General Theory of Strength for Anisotropic Materials. *J. Compos. Mater.*, 5(1):58–80, 1971.
- [69] S. Turteltaub, N. van Hoorn, W. Westbroek, and C. Hirsch. Multiscale mixed-mode failure criterion and traction-separation relation for composite materials. *Int. J. Solids Struct.*, 2017. Preprint submitted.
- [70] V. Tvergaard. Effect of Fibre Debonding in a Whisker-reinforced Metal. *Mat. Sci. Eng. A-Struct.*, 125:203–213, 1990.
- [71] V. Tvergaard and J. W. Hutchinson. The Influence of Plasticity on Mixed Mode Interface Toughness. *J. Mech. Phys. Solids*, 41(6):1119–1135, 1993.
- [72] F. van der Bas, F. Geuskens, J. Fatemi, and H. Scholten. Detailed design and analysis of the intermediate modulus CFRP ETF. Technical Report CUSS-DS-TN-012, Dutch Space, October 2013. Security Class: Restricted.
- [73] N. van Hoorn. Multiscale fracture simulations for composite materials. MSc. Thesis, TU Delft, Delft, January 2016.
- [74] J. G. M. van Mier. *Fracture processes of concrete*. CRC Press, Cleveland, OH, 1997.

- 
- [75] C. V. Verhoosel, J. J. C. Remmers, M. A. Gutiérrez, and R. de Borst. Computational homogenization for adhesive and cohesive failure in quasi-brittle solids. *Int. J. Numer. Meth. Engng.*, 83(8-9):1155–1179, 2010.
- [76] W. Voigt. Über die Beziehung zwischen den beiden Elasticitätsconstanten isotroper Körper. *Annalen der Physik*, 274:573–587, 1889.
- [77] A. A. Wells. Unstable Crack Propagation in Metals: Cleavage and Fast Fracture. In *Proceedings of the Crack Propagation Symposium*, volume 1, pages 210–230, Cranfield, 1961.
- [78] W. Westbroek. Multiscale Modeling of Fracture in Composites under Cryogenic Conditions. Literature report, TU Delft, Delft, April 2017.
- [79] H. M. Westergaard. Bearing Pressures and Cracks. *J. Appl. Mech.*, 2:289–305, 1939.
- [80] M. L. Williams. On the Stress Distribution at the Base of a Stationary Crack. *J. Appl. Mech.*, 24:109–114, 1957.
- [81] F. H. Wittmann, K. Rokugo, E. Bruehwiler, H. Mihashi, and P. Simonin. Fracture Energy and Strain Softening of Concrete as Determined by Means of Compact Tension Specimens. *Mater. Struct.*, 21(2):21–32, 1988.
- [82] D. Xie and A. M. Waas. Discrete cohesive zone model for mixed-mode fracture using finite element analysis. *Eng. Fract. Mech.*, 73(13):1783–1796, 2006.
- [83] X. P. Xu and A. Needleman. Void Nucleation by Inclusion Debonding in a Crystal Matrix. *Model. Simul. Mater. Sci. Eng.*, 1(2):111–132, 1993.
- [84] X. P. Xu and A. Needleman. Numerical simulations of fast crack growth in brittle solids. *J. Mech. Phys. Solids*, 42(9):1397–1434, 1994.
- [85] I. Yoshiaki and K. Aki. Seismic time function of propagating longitudinal-shear cracks. *Journal of Geophysical Research*, 77(11):2034–2044, 1972.
- [86] Z. Zhang, G. C. Paulino, and W. Celes. Extrinsic Cohesive modelling of dynamic fracture and microbranching instability in brittle solids. *Int. J. Numer. Meth. Engng.*, 72(8):893–923, 2007.

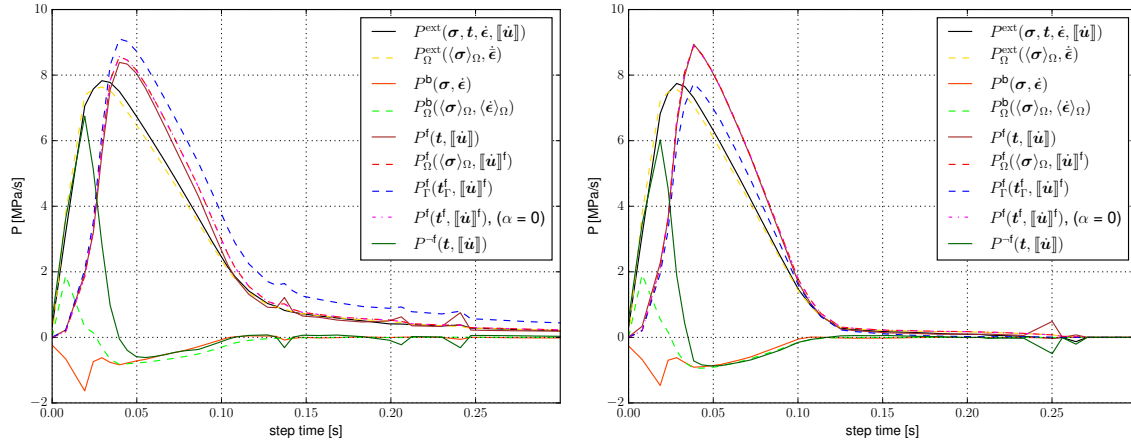
---

# Appendix A

---

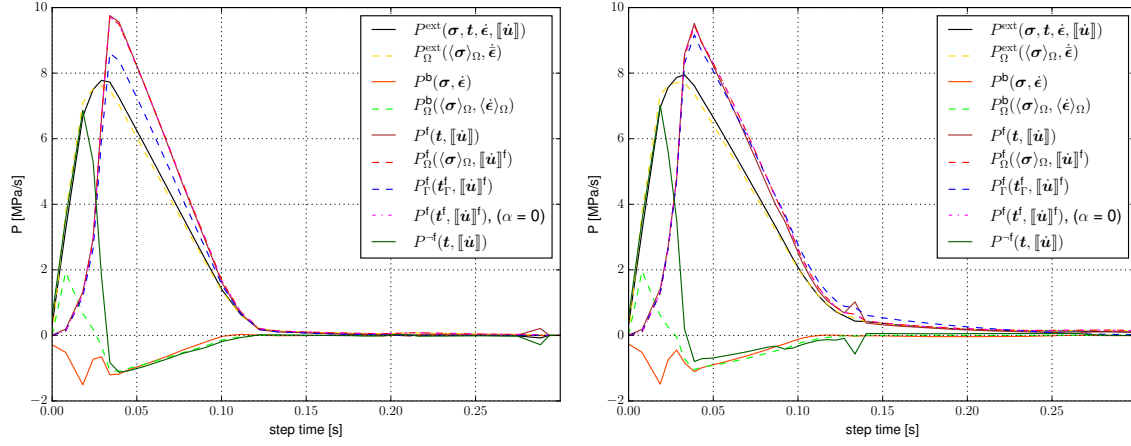
## Power Plots

This appendix includes the power plots used to satisfy the Hill-Mandel condition a posteriori. The procedure was discussed in Section 4.3.2. Figure A.1 shows the rate of work when forming a mode I crack at cryogenic temperature. The power required to create a mode I crack at room temperature is included in Figure A.2. In Figure A.3 and Figure A.4 the power as a function of step time is given for a mode II crack formed at cryogenic and room temperature respectively. Lastly the power plots for a mixed mode crack at cryogenic temperature is shown in Figure A.5 and at room temperature in Figure A.6.



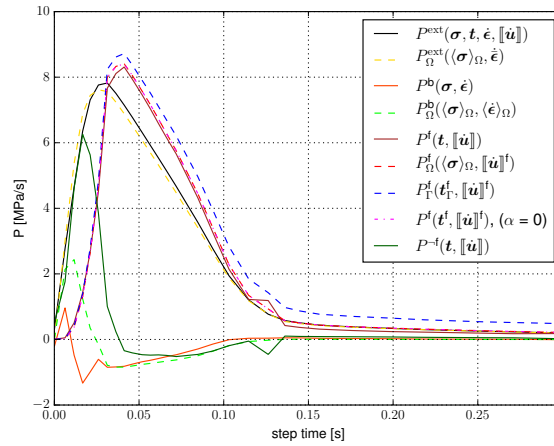
(a) Realization 1

(b) Realization 2



(c) Realization 3

(d) Realization 4



(e) Realization 5

Figure A.1: Power Plot: Uniaxial Extension,  $75 \times 75 \mu\text{m}$  MVE,  $T = 77 \text{ K}$

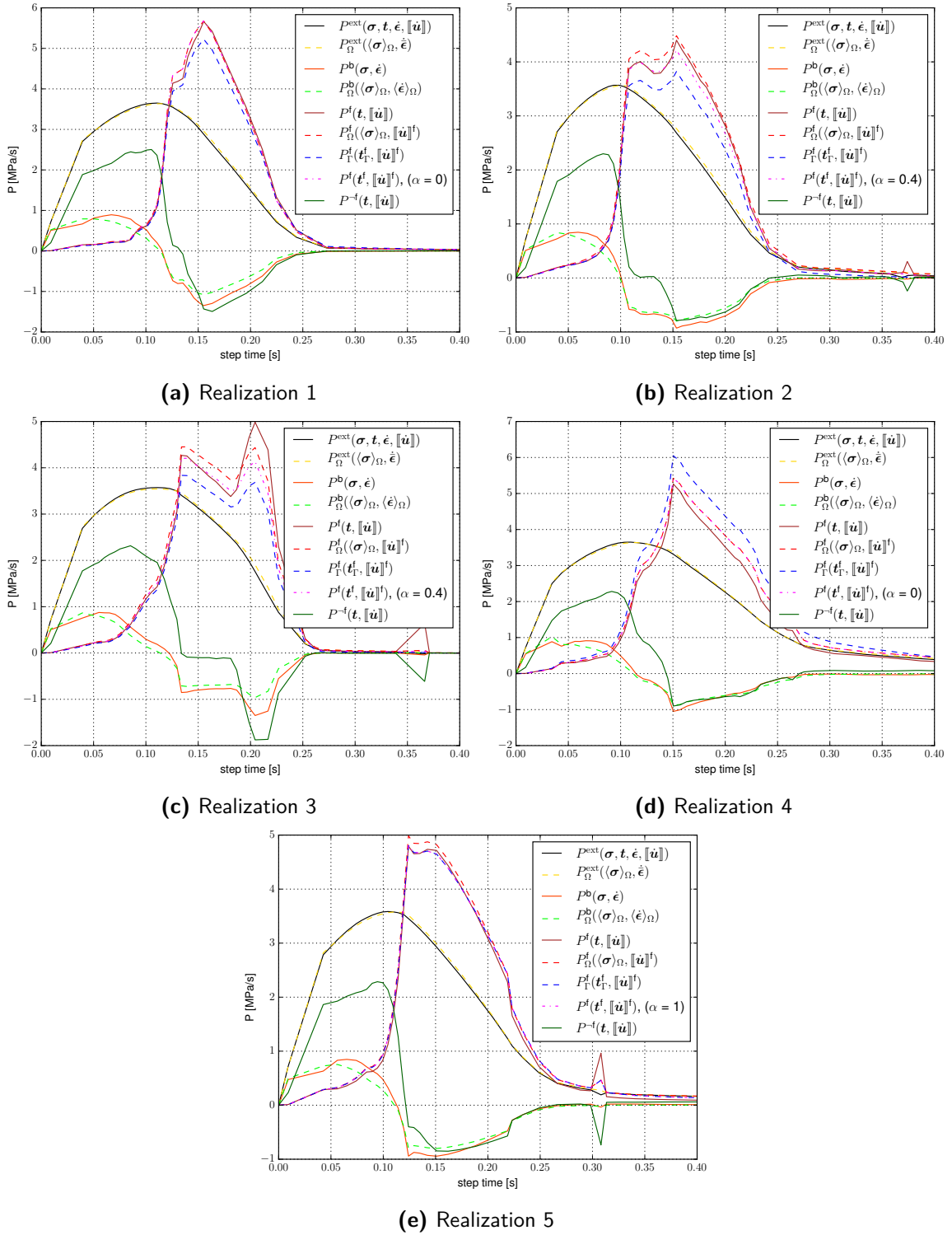
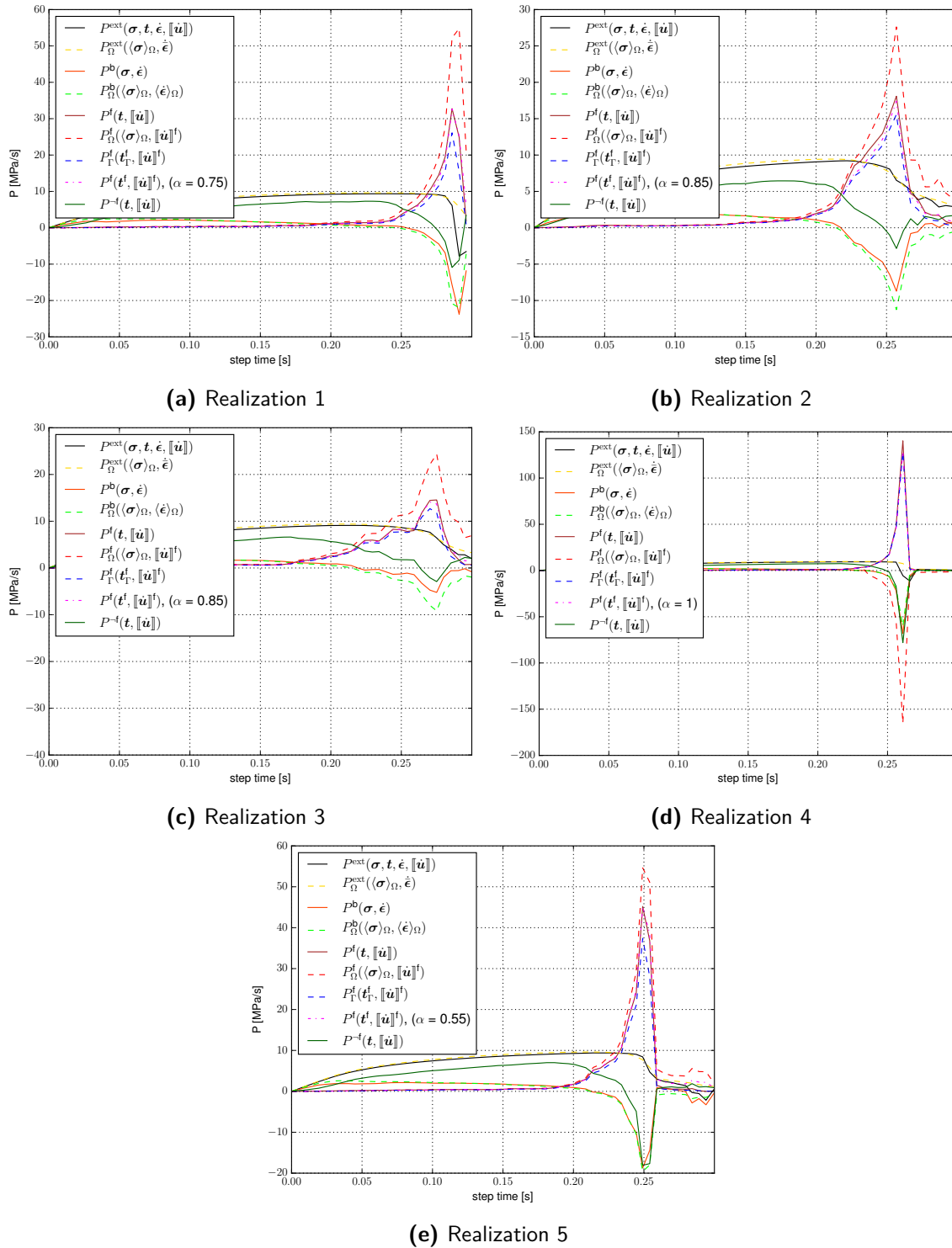
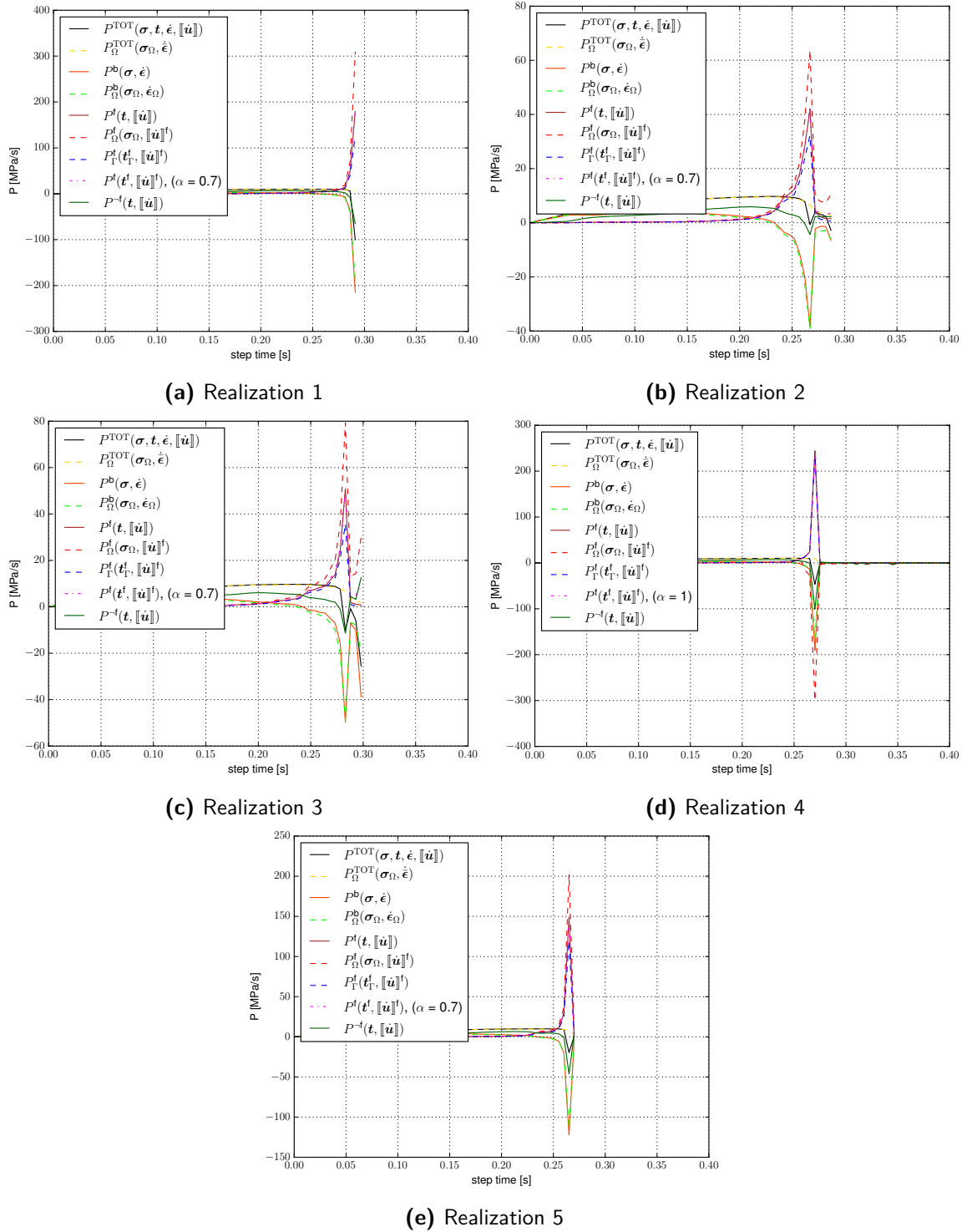


Figure A.2: Power Plot: Uniaxial Extension,  $75 \times 75 \mu\text{m}$  MVE,  $T = 298 \text{ K}$



**Figure A.3:** Power Plot: Biaxial Extension-Compression,  $75 \times 75 \mu\text{m}$  MVE,  $T = 77 \text{ K}$



**Figure A.4:** Power Plot: Biaxial Extension-Compression,  $75 \times 75 \mu\text{m}$  MVE,  $T = 298 \text{ K}$

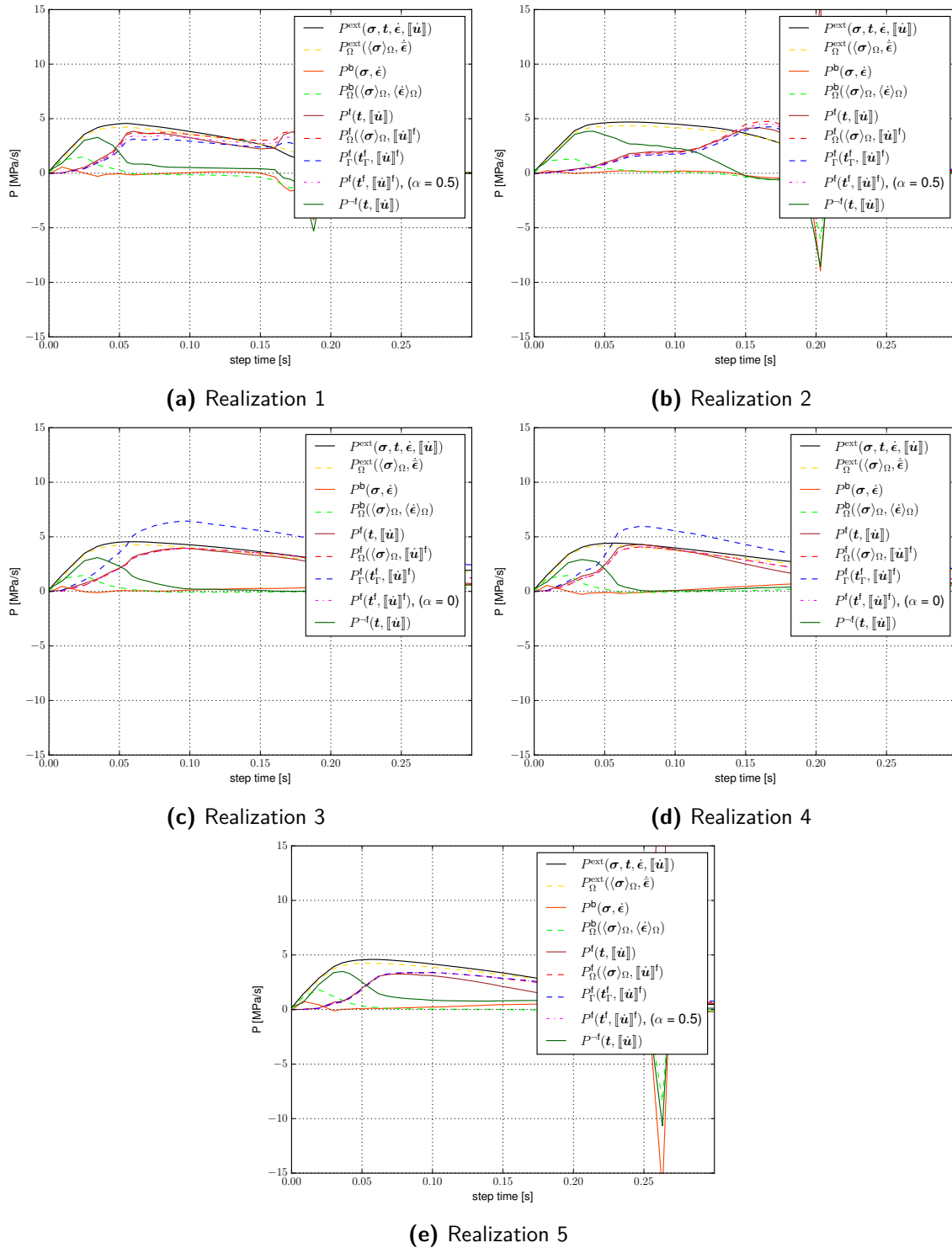


Figure A.5: Power Plot: Mixed Mode,  $75 \times 75 \mu\text{m}$  MVE,  $T = 77 \text{ K}$

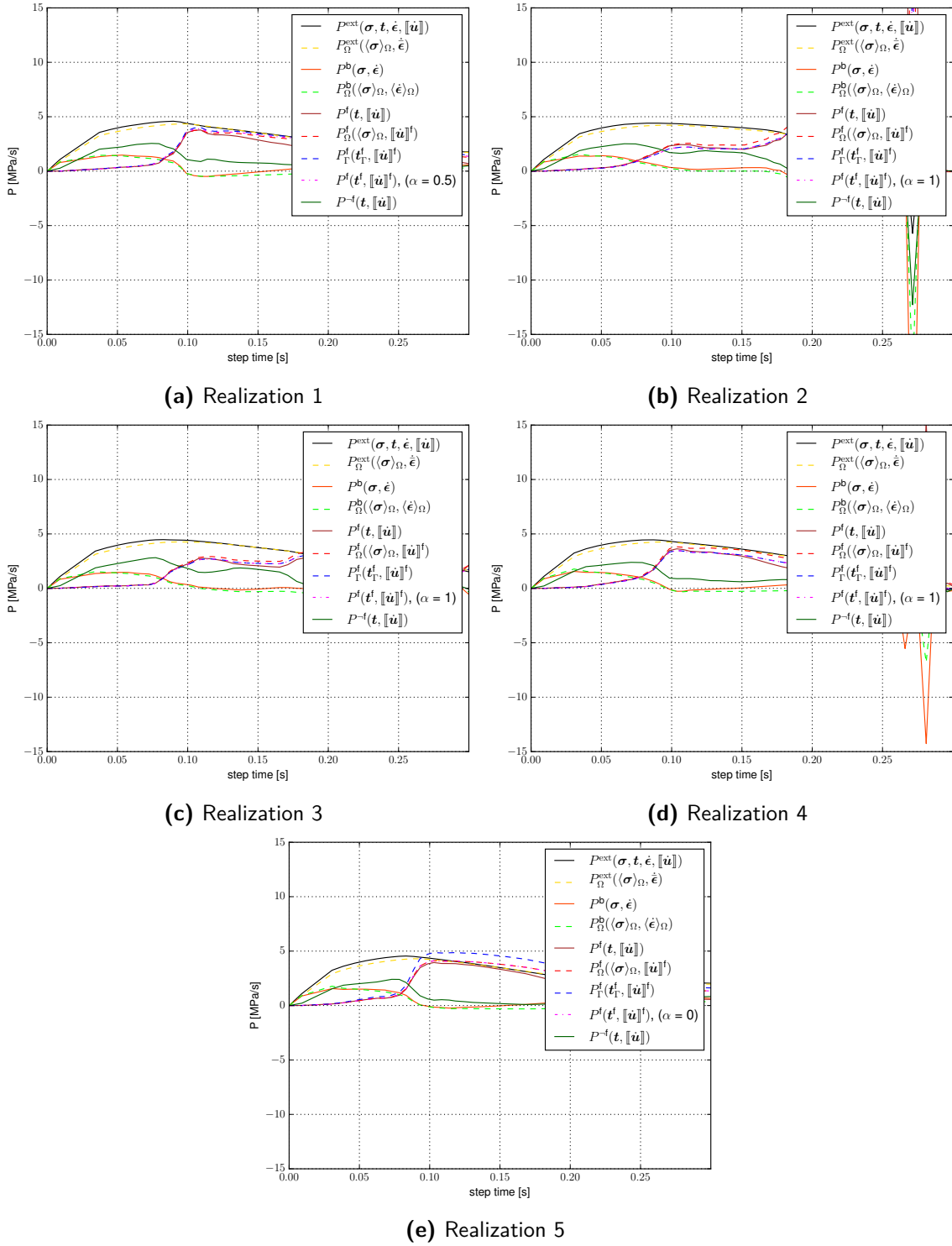


Figure A.6: Power Plot: Mixed Mode,  $75 \times 75 \mu\text{m}$  MVE,  $T = 298 \text{ K}$